Five Sample Joint Neutrino/Antineutrino Oscillation Analysis in T2K

Wing Yan Ma

Imperial College London

Submitted in part fulfilment of the requirements for the degree of
Doctor of Philosophy in Physics, September 2017

Abstract

This thesis describes a simultaneous fit to all five of the far detector oscillation samples analysed to date (FHC/RHC 1Rμ, FHC/RHC 1Re and FHC ν_e CC1π^+) using T2K data taken from 2009-2017 with 1.47×10^{21} POT in neutrino mode and 0.76×10^{21} POT in antineutrino mode. The aim of this analysis is to search for CP violation by setting limits on δ_{CP} and measure the oscillation parameters $\sin^2\theta_{13}$, $\sin^2\theta_{23}$ and $|\Delta m^2_{32}|$.

The T2K (Tokai to Kamioka) experiment is a long-baseline accelerator neutrino oscillation experiment that is designed to make precision measurements of neutrino oscillation by observing ν_μ disappearance and ν_e appearance. A ν_μ beam is produced using a 30 GeV proton beam at the J-PARC and is detected by the near detector complex, ND280, and by the far detector, Super-Kamiokande, which is 295 km away from J-PARC. The far detector and one of the near detectors are located in an off-axis direction to the neutrino beam centre, resulting a narrow neutrino energy peak of 0.6 GeV and where the ν_μ survival probability is expected to be minimal (or maximal ν_e appearance probability).

The neutrino fluxes and their uncertainties at the near and far detector are predicted by the Monte Carlo simulation tuned with data from external hadron production experiments. The uncertainties of the neutrino flux parameters and certain neutrino interactions parameters at the far detector are reduced by the measurement at the off-axis near detector. Since the last analysis there has been improvement to event reconstructions at SK which results in 20% increase in ν_e statistics and increased purity in the 1Rμ samples. Using data taken from 2009-2017, we observed 240 μ-like, 74 e-like, 15 ν_e CC1π^+-like events in neutrino mode, and 68 μ-like, 7 e-like events in antineutrino mode.

The best-fit oscillation parameter values for the T2K only fit are $\sin^2\theta_{13} = 0.0296^{+0.0066}_{-0.0052}$, $\sin^2\theta_{23} = 0.511^{+0.036}_{-0.032}$, $|\Delta m^2| = 2.458^{+0.058}_{-0.059} \times 10^{-3}\mathrm{eV}^2$ and $\delta_{CP} = -1.72^{+1.04}_{-0.92}$. The best-fit oscillation parameter values including a reactor constraint on $\sin^2\theta_{13}$ are $\sin^2\theta_{13} = 0.0224 \pm 0.0012$, $\sin^2\theta_{23} = 0.530^{+0.028}_{-0.034}$, $|\Delta m^2| = 2.462^{+0.059}_{-0.057} \times 10^{-3}\mathrm{eV}^2$ and $\delta_{CP} = -1.64 \pm 0.62$. These results are quoted from credible intervals presented in the result section. Confidence intervals for δ_{CP} are produced using the Feldman-Cousins method, and confidence intervals of the other oscillation parameters are produced using the constant $\Delta\chi^2$ method. The best-fit oscillation parameter values are found to be consistent with previous official results while giving tighter constraints.

There is a first indication of CP conservation in neutrino sector excluded at 2σ level. The results are also presented showing the correlations that exist between the oscillation parameters.

Acknowledgements

First of all, I would like to express my sincere gratitude to my supervisor, Dr. Morgan Wascko, for his support and advice throughout my PhD. Thank you for giving me opportunities to work on many aspects of the experiment.

I want to offer my thanks to everyone in the Imperial T2K group: Dr. Yoshi Uchida, Dr. Per Jonsson, Dr. Luke Pickering, Clarence Wret, Artur Sztuc and Toby Nonnenmacher. Special thanks to Dr. Phill Litchfield for his insightful advice and warm encouragements which has helped me a lot. Also, thanks to Dr. Patrick Dunne for his guidance and advice which has been very helpful. I am extremely grateful to have had the opportunity to work with such incredibly talented group of people, they have made the working environment very enjoyable.

I would like to thank everyone in the P-theta group, in particular Dr. Christophe Bronner and Dr. James Imber, for their help and advice on oscillation analysis. Quite unfortunately my work on the 2-ring π^0 sample did not make it into this thesis, but I deeply appreciate their work on the analysis software, their support and valuable advice throughout. I would also like to thank Miura-san and Mine-san for their kind help and support during my stay in Kamioka.

Many thanks again to Morgan and Phill, Dr. Antonin Vacheret and Dr. Steve Boyd who read and provided comments on drafts of this thesis. Their feedback immensely improved the manuscript. Any remaining mistakes are my own fault.

Finally, I would like to thank all my family and friends for their continuous support. In particular, I want to thank my sister, Vicky, for being amazingly supportive and I truly appreciate her believe and trust in me. Also, thanks to all my friends at Imperial, many of whom I met in the Badminton Club. Special thanks to Lucy, Victor, Oscar, Lu and Karl, whose friendship I value highly and who made the experience of my time at Imperial such a good one. I greatly miss the times when we enjoy ourselves at h-bar after many hours of badminton.

Above all, I thank *Him*, for giving me the courage and wisdom to pursue this research. Without His blessings I would not have been able to achieve what I have achieved. He, and only He, deserves all the praise and glory.

May God bless you all.

Declaration

The work and results presented in this thesis is my own. Chapters 1 and 2 describe the background on the theory motivating the analysis. Chapter 3 describes the T2K experiment whose data taken from 2009-2017 was analysed. This is the summary of the theoretical work of others, and all relevant papers and documents have been appropriately referenced.

Chapter 4 discusses the neutrino interaction models used in event generator which are work of others. I was solely involved with studying the proton final state interaction model, which is discussed in detail.

Chapter 5 describe the five far detector samples used for this analysis which were provided by the T2K-SK group. The development of the analysis framework used to perform the analysis is detailed on Chapter 6, to which I made significant contributions. My main contributions includes adapting new far detector samples which used a new reconstruction algorithm, implementing and validating new systematic parameterisation, and validating the framework for oscillation fits and producing fit results.

Contents

List of Tables

List of Figures

Chapter 1

Introduction

Particle physics is the study of elementary structure of matter and fundamental laws of interactions. Ever since the beginning of particle physics, physicists have been trying to come up with new theories/models and underlying symmetries that can describe all the fundamental particles and their interaction. The Standard Model (SM) of particle physics has been remarkably successful in describing the phenomenon of particles, making accurate predictions and grouping the known particles into families/generations. With the confirmation of the existence of Higgs bosons at CERN in 2012, the set of SM particles has been completed. However, there are still many issues that need new theories beyond the Standard Model to explain. For instance, gravity is not included in the SM but instead it is been treated separately usually using the general theory of relativity. Also, the existence of dark matter and dark energy and their nature cannot be explained by the SM, and how neutrinos acquire mass when only been observed in left-handed states (which will be detailed in later chapter). Hence, the Standard Model must be extended in order to describe existing observations and predict new/unobserved phenomena.

In recent years, there have been major improvements in our knowledge of neutrinos: the discovery that neutrinos have masses, and different neutrinos can transform into each other; this phenomenon is known as neutrino oscillation (or neutrino mixing). Neutrino oscillations is so far the only observed physical phenomenon that can not be explained by the SM. Since neutrinos not only play an important role in the small scale of particle physics but also massive scale of the evolution of the universe, this makes the study of neutrinos crucial to the future development of particle physics.

1.1 Thesis Overview

This thesis describes a simultaneous fit to five far detector data samples (FHC/RHC 1Rμ, FHC/RHC 1Re and FHC 1R ν_e CC1π^+) using data from 2009-2017 with 1.47×10^{21} protons on target (POT) in neutrino mode and 0.76×10^{21} POT in antineutrino mode.

Chapter 2 describes the general properties of neutrinos and various neutrino experiments. Chapter 3 describes the the Tokai-to-Kamioka Experiment (T2K) experimental setup. Chapter 4 describes neutrino event simulations and neutrino-nucleus interaction models. Chapter 5 describes each dataset that is are used as input to the oscillation analysis. Chapter 6 describes the analysis method and the results. In particular, the constraint on δ_{CP} using T2K dataset alone. Chapter 7 gives the conclusions and outlook.

Chapter 2

Neutrino Physics

The field of neutrino physics has advanced rapidly over the last two decades. It was exciting to see that achievements in this field has gained significant recognitions when the 2015 Nobel Prize was awarded to Takaaki Kajita and Arthur B. McDonald in recognition of their contributions towards the discovery of neutrino oscillations, and five neutrino oscillation experiments sharing the 2016 Breakthrough Prize in Fundamental Physics. This discovery changes our understanding of matter fundamentally, and provided a key role in understanding the universe. While there still remains many questions about neutrinos, their properties are slowly being revealed by various neutrino experiments during recent years.

The postulate of the existence of a neutrino goes back to 1930 when Wolfgang Pauli attempted to explain the continuous energy spectrum of β particles emitted in nuclear decays. The process discovered by James Chadwick in 1914 [21] was thought to be a two-body decay which should give a discrete energy spectrum. But Pauli proposed that the spectrum could be explained if an unobserved neutral spin $\frac{1}{2}$ particle with extremely small mass were among the decay products [22]. It was in 1934 that Italian physicist Enrico Fermi took up Pauli's idea and created a theory based on this three-body decay, modelling the process as a neutron converting into a proton, an electron and named Pauli's postulate particle as the "neutrino". It is the neutrino that carries away part of the energy released during the decay resulting a continuous energy spectrum of electrons. The existence of (anti-)neutrino was eventually confirmed in

1956 by Cowan and Reines [23] through observing detectable outputs originating from inverse β decays. In 1962 Lederman, Schwartz and Steinberger [24] found that more than one type of neutrino exists by detecting interactions of the muon neutrino for the first time. It was not until 2000 that the DONUT experiment at Fermilab [25] detected τ neutrinos and completed the full third generation of lepton.

2.1 Standard Model Neutrino and its properties

The Standard Model (SM) of particle physics consist of six quarks and six leptons which are all spin $\frac{1}{2}$ Dirac fermions and has a corresponding antiparticle which has opposite charge. There are three fundamental interactions in the SM which are the strong, weak and the electromagnetic interactions, and they are mediated by spin 1 gauge bosons. The strong interaction is mediated by massless gluons and they only interact with quarks and other gluons. The electromagnetic interaction is mediated by massless photons and they interact with all electrically charged particles (except neutrinos which are neutral). Weak interactions occur to all fermions and are mediated by the massive weak bosons: $W^{\pm}$ which have ± 1 electric charge and Z^0 which is neutral. Figure 2.1 (from [26]) summarises the SM.

The neutrino is an elementary particle with zero charge, which were produced abundantly from the Big Bang. Neutrinos only participate in Weak interactions, and so the cross section of neutrino interactions is around $10^{-40} cm^2$. These features make neutrinos extremely difficult to detect in experiments.

The SM is a major achievement in particle physics in the last century, it has become the basic theory describing characteristics of particles and interactions between them. So far, almost all the experimental results support this theoretical model. In the SM, neutrinos are neutral spin $\frac{1}{2}$ fermions. There are three types (or so-called “flavour”) of neutrinos: electron neutrinos, μ neutrinos and τ neutrinos, corresponding to the three charged leptons. Lepton number is

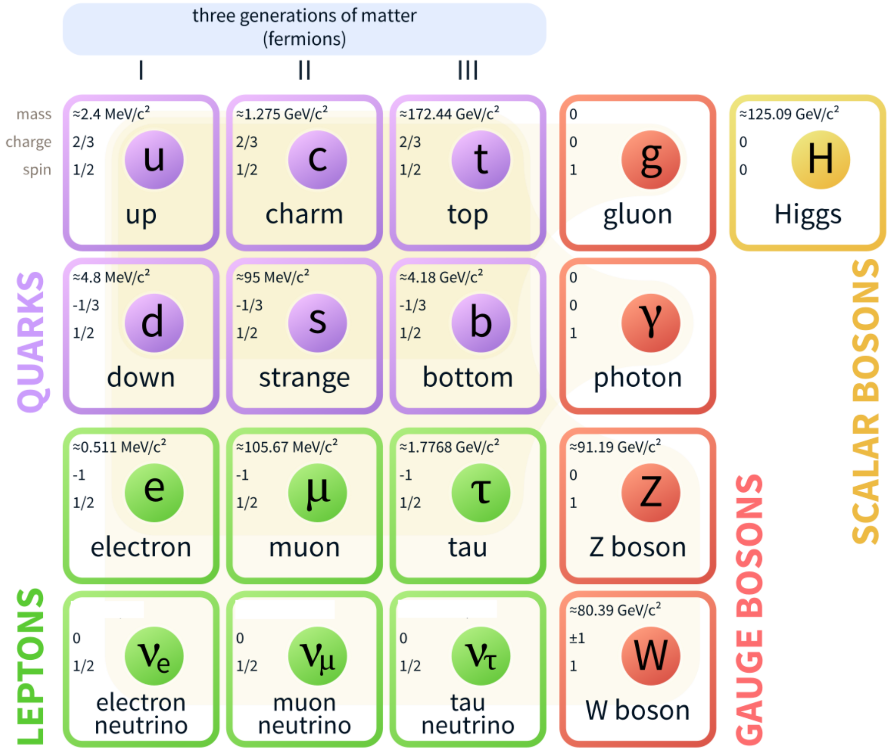

Figure 2.1: Overview of the Standard Model. The fermions in each row are identical except for the masses.

conserved separately for each of the three lepton families:

$$\begin{pmatrix} \nu_e \\ e^- \end{pmatrix}, \begin{pmatrix} \nu_\mu \\ \mu^- \end{pmatrix}, \begin{pmatrix} \nu_\tau \\ \tau^- \end{pmatrix} \tag{2.1}$$

In 1957 there was a revolutionary discovery that parity is violated in Weak interactions [27], which was soon followed by the observation that only left-handed neutrinos are involved in Weak interactions [28] (no right-handed neutrinos whatsoever). In the same year, Lee and Yang [29], Landau [30], and Salam [31] independently proposed a two-component model of the neutrino, each of which stated that there are only left-handed neutrinos with mass strictly at zero. The two-component neutrino Dirac theory and Weinberg-Salam weak interaction model described in [32, 33], shows the presence of only left-handed neutrinos and right-handed antineutrinos. Since right-handed neutrinos in this theory do not exist, neutrinos cannot acquire a mass via a Dirac mass term, i.e. neutrino mass is zero. Moreover, this theory predicts the existence of mixing between three generations of quarks, also known as oscillation, with the mixing matrix being unitary. But lepton number conservation ensures that the mixing does not occur between three generations of neutrinos. Since neutrinos were assumed to be massless in the SM, therefore any neutrino experiments that have found evidence of mass or oscillation will require some form of extension of the SM.

2.2 Neutrino mixing

2.2.1 Proposal of neutrino mixing

According to the Higgs mechanism in the SM, quarks and charged leptons acquire mass as they collide with the Higgs field and change their handedness. Therefore, if the mechanism is to be promoted to introduce right-handed neutrino using the same method, neutrinos can have mass. However this does not explain the fact that neutrino mass is much smaller than other fermions. In 1958, Italian physicist Bruno Pontecorvo [34] pointed out that if the neutrino mass is non-zero, different flavours of neutrinos can interchange between each other.

2.2.2 Discovery of Neutrino mixing

The Standard Solar Model (SSM) predicts rates and spectra of photons and neutrinos coming from nuclear reactions in the sun. When solar neutrinos strike the Earth they can react with atomic nuclei to produce electrons. In the 1960s, R. Davis et. al. at Homestake [35] successfully detected solar neutrinos, but the data obtained is only $\sim 1/3$ of the SSM predictions. This is commonly known as “the solar neutrino problem”. In 2001 the SNO experiment in Canada confirmed the missing solar neutrinos oscillate into other neutrino flavours [36]. This experiment is of decisive significance, it measured both the ν_e flux through Charged-current (CC) interactions for ν_e only ($\nu_e + d \to p + p + e^-$) and the total neutrino flux through flavour-independent Neutral-current (NC) interactions ($\nu_x + d \to p + n + \nu_x$) as well as elastic scattering ($\nu_x + e^- \to \nu_x + e^-$) which happens through both charged and neutral current channels. Not only did SNO observe the ν_e flux deficit, but it was also able to measure the ratio of ν_e flux to the total neutrino flux to be 0.301 ± 0.033, thus providing a perfect solution to the long-standing solar neutrino problem.

Another important phenomenon is the atmospheric neutrino anomaly. The Kamiokande experiment observed a large deficit in the flavour ratio $(\nu_\mu + \overline{\nu}_\mu)/(\nu_e + \overline{\nu}_e)$ [37] which is a further indirect evidence of neutrino mixing, In 1998, Super-Kamiokande reported a statistically significant deficit in the upward-going ν_μ events compared to the expectations assuming no oscillations was observed [38]. Both discoveries led to the Nobel Prize being awarded to Takaaki Kajita (Super-Kamiokande) and Arthur B. McDonald (SNO) in 2015.

2.2.3 Dirac and Majorana neutrinos

In the standard Weinberg-Salam $SU(2) \times U(1)$ electroweak theory, the neutrino mass is zero as a result of two assumptions: right-handed neutrinos and left-handed antineutrinos do not exist, and lepton number conservation. If either one of these two assumptions is not satisfied, neutrinos can acquire mass. According to the SM, the charged leptons and left-handed neutrinos form a doublet. Since the charged leptons have mass, they can have both left and right hand states, so a Dirac mass m_D comes naturally as:

$$\mathcal{L}_D = -m_D\overline{\psi}\psi = -m_D(\overline{\psi_R}\psi_L + \overline{\psi_L}\psi_R), \tag{2.2}$$

We call the neutrinos described by equation 2.2 as Dirac neutrinos. Here the lepton number is clearly conserved with the same amount of left- and right-handed states. But the situation is different for neutrinos because neutrinos have no charge. Since the weak interaction only couples to left-handed neutrinos, neutrino do not need to have a right-handed component that is necessary for generating the mass term. In an extended SM, right-handed neutrinos also exist and they interact only via coupling to left-handed neutrinos.

Furthermore, since right-handed neutrinos are neutral, according to Lorentz invariance, we may introduce a Majorna mass term m_M:

$$\mathcal{L}_M = \frac{1}{2} m_M \left(\overline{\psi_R^C} \psi_R + \overline{\psi_R} \psi_R^C \right) \tag{2.3}$$

where ψ_R^C is the charge conjugated right-handed neutrino field. Neutrinos and antineutrinos can interchange between one another through $\mathcal{L}_M$, hence violating lepton number. We call the neutrinos described by equation 2.3 as Majorana neutrinos.

2.2.4 Neutrino oscillation theory

Since the neutrino takes part in weak interactions only, a W boson decay which produces a lepton l_α ($\alpha = e,\ \mu,\ \tau$) will also produce a neutrino of the same flavour, ν_α. However, in the equation of motion describing neutrino propagation, the Hamiltonian depends on neutrino energy, and the mass of such neutrino. Neutrino flavour eigenstates $|\nu_\alpha\rangle$ and mass eigenstates $|\nu_i\rangle$ are different, they can be related by a unitary transformation matrix U:

$$|\nu_\alpha\rangle = \sum_i \mathrm{U}^*_{\alpha i} |\nu_i\rangle \tag{2.4}$$

where $i = 1,\ 2,\ 3, \ldots$ are the neutrino mass eigenstates. U is the 3×3 unitary leptonic mixing matrix referred to as the Pontecorvo-Maki-Nakagawa-Sakata (PMNS) matrix [39], which is analogous to the Cabbibo-Kobayashi-Maskawa (CKM) matrix [40] in the quark sector.

Neutrino oscillations in vacuum

When a neutrino propagate in vacuum, evolution of a mass eigenstate $|\nu_i\rangle$ after traveling time t is:

$$|\nu_i(t)\rangle = \exp(-i(E_i t - |\mathbf{p}_i| L)) |\nu_i(0)\rangle \tag{2.5}$$

where t is the time taken for the neutrino to travel distance L and $\mathbf{p}_i$ is the momentum three-vector. From equation 2.4, we can write:

$$|\nu_\alpha\rangle = \sum_i \mathrm{U}_{\alpha i}\, \exp(-i(E_i t - |\mathbf{p}_i|L))\, |\nu_i(0)\rangle \tag{2.6}$$

Since neutrino masses are very small ($m_i^2 \ll E_i^2$) we can use the relativistic limit:

$$|\mathbf{p}_i| = \sqrt{E_i^2 - m_i^2} \simeq E_i - \frac{m_i^2}{2E_i}, \tag{2.7}$$

Therefore we can write:

$$E_i t - |\mathbf{p}_i|L \simeq E_i(t - L) + \frac{m_i^2}{2E_i}L, \tag{2.8}$$

If we assume that all mass-eigenstates ν_i composing the initial flavour state ν_α have the same energy E, then we can rewrite equation 2.8 as:

$$E_i t - |\mathbf{p}_i|L \simeq E(t - L) + \frac{m_i^2}{2E}L, \tag{2.9}$$

With this approximation, equation 2.6 can be written as:

$$\begin{aligned} |\nu_\alpha\rangle &= \sum_i \mathrm{U}_{\alpha i}\, \exp\Big(-i\frac{m_i^2 L}{2E}\Big)\, |\nu_i(0)\rangle \\ &= \sum_i \mathrm{U}_{\alpha i}\mathrm{U}^*_{\beta i}\, \exp\Big(-i\frac{m_i^2 L}{2E}\Big)\, |\nu_\beta\rangle \end{aligned} \tag{2.10}$$

Notice that the phase $E(t - L)$ has been omitted for the rest of the calculation because it is common to all mass eigenstates and therefore it is irrelevant for neutrino oscillation. The same energy assumption may be unjustified given that neutrinos with different masses should have different energies and momenta. Nevertheless this assumption simplifies the derivation greatly and the same final result can still be achieved. A more rigorous treatment and discussion of why this simplification gives the same result can be found in [41].

The transition probability of $\nu_\alpha \to \nu_\beta$ can then be written as:

$$\begin{aligned} P(\nu_\alpha \to \nu_\beta) &= |\langle \nu_\beta | \, \nu_\alpha \rangle|^2 \\ &= \Big| \sum_i \mathrm{U}_{\alpha i} \mathrm{U}^*_{\beta i} \, \exp\Big(-i \frac{m_i^2 L}{2E} \Big) \Big|^2 \\ &= \sum_{i,j} \mathrm{U}^*_{\alpha i} \mathrm{U}_{\beta i} \mathrm{U}_{\alpha j} \mathrm{U}^*_{\beta j} \exp\Big(-i \frac{(m_i^2 - m_j^2) L}{2E} \Big) \end{aligned} \tag{2.11}$$

For derivation purpose, we write $M^{ij}_{\alpha\beta} = \mathrm{U}^*_{\alpha i} \mathrm{U}_{\beta i} \mathrm{U}_{\alpha j} \mathrm{U}^*_{\beta j}$ and $\Phi_{ij} = (m_i^2 - m_j^2) L/2E$. We can split the summation and use $\Re[a] = (a + a^*)/2$ to write equation 2.11 as:

$$\begin{aligned} \sum_{i,j} M^{ij}_{\alpha\beta} e^{-i\Phi_{ij}} &= \sum_{i=j} M^{ij}_{\alpha\beta} + \sum_{i>j} M^{ij}_{\alpha\beta} e^{-i\Phi_{ij}} + \sum_{i<j} M^{ij}_{\alpha\beta} e^{-i\Phi_{ij}} \\ &= \sum_i |\mathrm{U}_{\alpha i}|^2 |\mathrm{U}_{\beta i}|^2 + \sum_{i>j} \Big[M^{ij}_{\alpha\beta} e^{-i\Phi_{ij}} + M^{ij*}_{\alpha\beta} e^{i\Phi_{ij}} \Big] \\ &= \sum_i |\mathrm{U}_{\alpha i}|^2 |\mathrm{U}_{\beta i}|^2 + 2 \sum_{i>j} \Re[M^{ij}_{\alpha\beta} e^{-i\Phi_{ij}}] \end{aligned} \tag{2.12}$$

Using the unitarity condition $\sum_i \mathrm{U}^*_{\alpha i} \mathrm{U}_{\beta i} = \delta_{\alpha\beta}$ and multiply with its complex conjugate, we have

$$\begin{aligned} \delta_{\alpha\beta} &= \sum_{i,j} \mathrm{U}^*_{\alpha i} \mathrm{U}_{\beta i} \mathrm{U}_{\alpha j} \mathrm{U}^*_{\beta j} \\ &= \sum_i |\mathrm{U}_{\alpha i}|^2 |\mathrm{U}_{\beta i}|^2 + 2 \sum_{i>j} \Re[M^{ij}_{\alpha\beta}] \end{aligned} \tag{2.13}$$

Then we can rewrite equation 2.11 using equation 2.12 and equation 2.13 as:

$$\begin{aligned}
P(\nu_\alpha \to \nu_\beta) &= \delta_{\alpha\beta} - \sum_{i>j}[M^{ij}_{\alpha\beta} + M^{ij*}_{\alpha\beta}] + \sum_{i>j}\Big[M^{ij}_{\alpha\beta}e^{-i\Phi_{ij}} + M^{ij*}_{\alpha\beta}e^{i\Phi_{ij}}\Big] \\
&= \delta_{\alpha\beta} - \sum_{i>j}[M^{ij}_{\alpha\beta} + M^{ij*}_{\alpha\beta}] + \frac{1}{2}\sum_{i>j}\Big[(M^{ij}_{\alpha\beta} + M^{ij*}_{\alpha\beta})(e^{-i\Phi_{ij}} + e^{i\Phi_{ij}})\Big] \\
&\quad + \frac{1}{2}\sum_{i>j}\Big[(M^{ij}_{\alpha\beta} - M^{ij*}_{\alpha\beta})(e^{-i\Phi_{ij}} - e^{i\Phi_{ij}})\Big] \\
&= \delta_{\alpha\beta} - 2\sum_{i>j}\Re[M^{ij}_{\alpha\beta}](1-\cos\Phi_{ij}) - \frac{1}{2}\sum_{i>j}\Big[(M^{ij}_{\alpha\beta} - M^{ij*}_{\alpha\beta})(e^{-i\Phi_{ij}} - e^{i\Phi_{ij}})\Big] \\
&= \delta_{\alpha\beta} - 2\sum_{i>j}\Re[M^{ij}_{\alpha\beta}](1-\cos\Phi_{ij}) + 2\sum_{i>j}\Im[(M^{ij}_{\alpha\beta}]\sin\Phi_{ij} \qquad (2.14)
\end{aligned}$$

Substitute $M^{ij}_{\alpha\beta}$ and Φ_{ij} and rewrite to obtain:

$$\begin{aligned}
P(\nu_\alpha \to \nu_\beta) = \delta_{\alpha\beta} &- 4\sum_{i>j}\Re(\mathrm{U}^*_{\alpha i}\mathrm{U}_{\beta i}\mathrm{U}_{\alpha j}\mathrm{U}^*_{\beta j})\sin^2(\Delta m^2_{ij}\frac{L}{4E}) \\
&+ 2\sum_{i>j}\Im(\mathrm{U}^*_{\alpha i}\mathrm{U}_{\beta i}\mathrm{U}_{\alpha j}\mathrm{U}^*_{\beta j})\sin(\Delta m^2_{ij}\frac{L}{2E}) \qquad (2.15)
\end{aligned}$$

where $\Delta m^2_{ij} \equiv m^2_i - m^2_j$ is the mass-squared difference. The transition probability for antineutrinos, $P(\bar{\nu}_\alpha \to \bar{\nu}_\beta)$, is therefore:

$$\begin{aligned}
P(\bar{\nu}_\alpha \to \bar{\nu}_\beta) = \delta_{\alpha\beta} &- 4\sum_{i>j}\Re(\mathrm{U}^*_{\alpha i}\mathrm{U}_{\beta i}\mathrm{U}_{\alpha j}\mathrm{U}^*_{\beta j})\sin^2(\Delta m^2_{ij}\frac{L}{4E}) \\
&- 2\sum_{i>j}\Im(\mathrm{U}^*_{\alpha i}\mathrm{U}_{\beta i}\mathrm{U}_{\alpha j}\mathrm{U}^*_{\beta j})\sin(\Delta m^2_{ij}\frac{L}{2E}) \qquad (2.16)
\end{aligned}$$

Looking at equation 2.15, it is immediately clear that neutrino flavour change can only occur when at least two neutrinos are not degenerate in mass ($m^2_i \neq m^2_j$). If $m^2_i = m^2_j$, $\Delta m^2_{ij} = 0$ for all i, j, and equation 2.15 reduces to $P(\nu_\alpha \to \nu_\beta) = \delta_{\alpha\beta}$, i.e. no flavour change. Since U is unitary, $\sum_\beta P(\nu_\alpha \to \nu_\beta) = 1$ which means the total neutrino flux is constant while it is redistributed amongst the flavours. We can also see that the probability for a neutrino to oscillate depends on L/E; different neutrino experiments with a given baseline and energy range can probe different oscillation parameters phase space.

When deriving the antineutrino oscillation probability CPT invariance is assumed, therefore if U is complex, $P(\nu_\alpha \to \nu_\beta) \neq P(\bar{\nu}_\alpha \to \bar{\nu}_\beta)$ and violates CP symmetry. If U is real then there will be no CP violation. While the oscillation probability only depends on the mass-squared *difference*, Δm^2_{ij} (not the actual neutrino masses). This implies that neutrino oscillation measurements can only probe the differences between the masses of the different mass eigenstates but not their absolute scale. Other measurements are needed to probe the absolute mass, as described in Section 2.4.2.

Parameterisation of PMNS matrix in terms of mixing angles and phases

The PMNS matrix can be parameterised in terms of three mixing angles θ_{12}, θ_{13}, and θ_{23} and three CP-violating phases δ, α_1, and α_2:

$$\mathrm{U} = \underbrace{\begin{pmatrix} 1 & 0 & 0 \\ 0 & c_{23} & s_{23} \\ 0 & -s_{23} & c_{23} \end{pmatrix}}_{Atmospheric} \underbrace{\begin{pmatrix} c_{13} & 0 & s_{13}e^{-i\delta} \\ 0 & 1 & 0 \\ -s_{13}e^{i\delta} & 0 & c_{13} \end{pmatrix}}_{Cross-mixing} \underbrace{\begin{pmatrix} c_{12} & s_{12} & 0 \\ -s_{12} & c_{12} & 0 \\ 0 & 0 & 1 \end{pmatrix}}_{Solar} \underbrace{\begin{pmatrix} e^{i\alpha_1/2} & 0 & 0 \\ 0 & e^{i\alpha_2/2} & 0 \\ 0 & 0 & 1 \end{pmatrix}}_{Majorana} \tag{2.17}$$

where s_{ij} and c_{ij} $(i, j = 1, 2, 3)$ represent sin θ_{ij} and cos θ_{ij} respectively. U is commonly decomposed into four component matrices to make it easier to interpret. The first matrix is known as the atmospheric matrix which includes only the mixing angle θ_{23}, it dominates the mixing seen in atmospheric neutrinos. For atmospheric neutrinos, transitions of ν_e can be neglected and so this can approximated by a two-flavour neutrino oscillation; then the atmospheric mixing angle $\theta_{atm} \approx \theta_{23}$.

The second matrix is known as the cross-mixing matrix which depends on the mixing angle θ_{13} and the CP-violating phase δ_{CP} . A non-zero δ_{CP} would result in $P(\nu_\alpha \to \nu_\beta) \neq P(\bar{\nu}_\alpha \to \bar{\nu}_\beta)$.

The third matrix is known as the solar matrix which includes only the mixing angle θ_{12}, it dominates the mixing of solar neutrinos. Similar to the atmospheric neutrinos, $\theta_{12} \approx \theta_{sol}$ if we approximate solar neutrino mixing in a two-flavour model.

If neutrinos are Majorana fermions then the final matrix exist in equation 2.17 which includes the “Majorana” CP-violating phases (see Section 2.2.3). This has no impact on the oscillation probabilities as the additional phases cancel out in equation 2.15. It is not possible to determine whether neutrinos are their own antiparticles from observing neutrino oscillations.

Including the factors of $\hbar$ and c which have been omitted so far, the argument of the sin terms in equations 2.15 and 2.16 give:

$$\Delta m_{ij}^2 \frac{L}{4E} = 1.267 \Delta m_{ij}^2 (\mathrm{eV}^2) \frac{L(\mathrm{km})}{E(\mathrm{GeV})}$$

which means that an experiment with a given L and E can probe the mass-squared phase space $\sim 1.267(L/E)^{-1}$. T2K has a baseline of 295 km and a peak neutrino energy of 0.6 GeV, therefore it is sensitive to mass-squared splittings $\mathcal{O}(10^{-3}\mathrm{eV}^2) \gg \Delta m_{21}^2$. So the effect on neutrino oscillation due to Δm_{21}^2 can be neglected and oscillation probabilities can be approximately described by two mixing angles θ_{13} and θ_{23}. In T2K where ν_e appearance and ν_μ disappearance are observed, their probabilites can be written (to leading order) as:

$$P(\nu_\mu \to \nu_e) \approx 2\,\sin^2(2\theta_{13})\sin^2(\theta_{23})\sin^2\Big(1.267\Delta m_{32}^2(\mathrm{eV}^2)\frac{L(\mathrm{km})}{E(\mathrm{GeV})}\Big) \tag{2.18}$$

$$P(\nu_\mu \to \nu_\mu) \approx 1 - \cos^4(\theta_{13})\sin^2(2\theta_{23})\sin^2\Big(1.267\Delta m_{32}^2(\mathrm{eV}^2)\frac{L(\mathrm{km})}{E(\mathrm{GeV})}\Big) \tag{2.19}$$

If we write out the sub-leading terms of equation 2.19 we will find that a sinδ term is multiplied by the sine of all 3 mixing angles, therefore all mixing angles need to be non-zero to have CP violation. Confirmation of $\theta_{13} \neq 0$ has been a crucial finding since this is the smallest mixing angle and the last to be measured. $\theta_{13} \neq 0$ was first confirmed by the Daya Bay Neutrino Experiment in 2012 at 5σ [42], and then by T2K in 2014 [43].

Neutrino oscillations in matter

When neutrinos propagate through matter, they can be affected by coherent forward-scatterings with the medium. All flavours of neutrinos can undergo NC interactions with electrons and

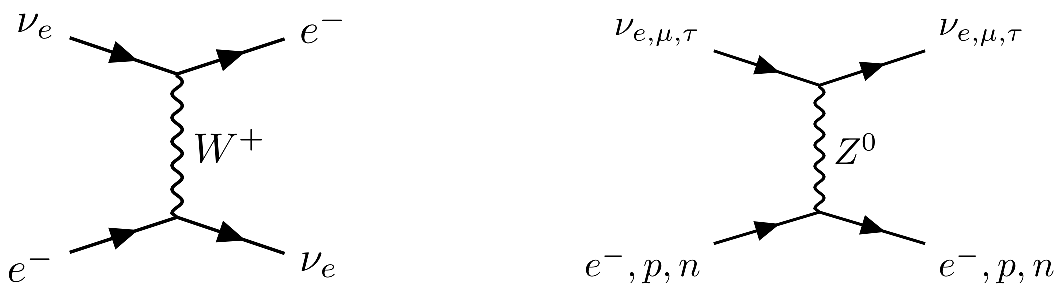

Figure 2.2: Feynman diagrams showing neutrino interactions in matter. Neutrinos can interact via the charged current (CC) (left) and neutral current (NC) (right) processes. The ν_e can interact via the CC mode due to electron presence in matter, while all three flavours can couple to the Z^0 for NC interactions.

nucleons in matter, while ν_e can undergo CC interactions with electrons in matter and experience an extra potential. The effect results in an additional potential V_{MSW} to the Hamiltonian in vacuum:

$$V_{MSW} = \pm\sqrt{2}G_F n_e \tag{2.20}$$

where G_F is the Fermi coupling constant and n_e is the number density of electrons. This matter effect was realised by L. Wolfenstein, S. Mikheyev and A. Smirnov and is also referred to as the MSW effect [44, 45]. Since matter itself is CP asymmetric (no anti-matter), neutrinos and anti-neutrinos experience opposite signs of the potential V_{MSW} in equation 2.20. The matter effect adds an extra source of CP violation into the oscillation probabilities resulting in a degeneracy with the intrinsic CP violation discussed in Section 2.2.4. A CP asymmetry can be observed in experiments with neutrinos passing through a significant amount of matter even if $\delta_{CP} = 0$. This degeneracy can be lifted by combining several experiments with different baseline to measure both ν_e and $\overline{\nu}_e$ appearance.

2.2.5 Mass hierarchy

While the mass squared differences between the neutrino mass states have been measured with high precisions, the sign of Δm^2_{32} (or Δm^2_{31}) is still yet to be determined since the oscillation

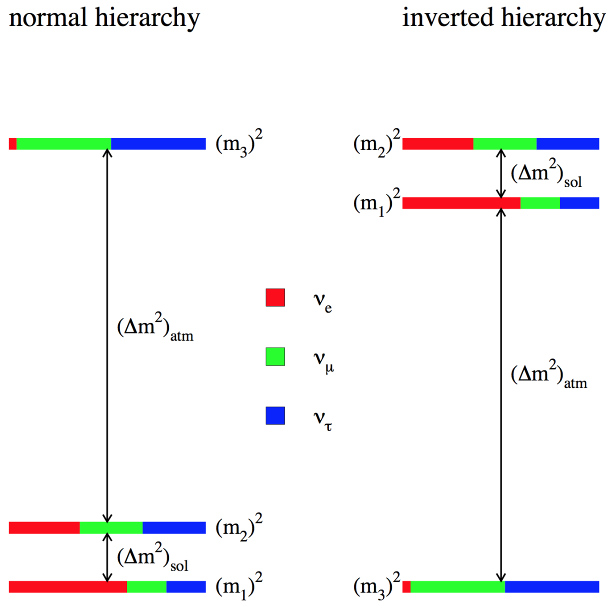

Figure 2.3: Relationship between neutrino mass and flavour eigenstates for normal and inverted hierarchy. The different colour indicates the flavour content of each mass eigenstate. Figure taken from [2].

probability in the leading order does not depend on the sign of Δm^2 (the sign of Δm^2_{21} has been determined through observing matter effect in solar neutrinos). As shown in Figure 2.3, positive Δm^2_{32} is referred to as "normal hierarchy" (NH or normal ordering) with the mass eigenstate m_3 having the largest mass, while negative Δm^2_{32} is referred to as "inverted hierarchy" (IH or inverted ordering) with m_3 having the smallest mass. Results throughout this thesis will be shown assuming each case separately.

2.3 Neutrino Oscillation Experiments

We saw in the previous section that neutrino oscillation probabilities are a function of both the distance that the neutrino travels (L) and the neutrino energy (E). Therefore experiments with different L and E are sensitive to different domains of oscillation space. In recent years, the solar neutrino puzzle, the atmospheric neutrino anomaly and other experimental facts indicated the presence of neutrino mixing phenomena. With θ_{13} being the last mixing angle that has been measured, neutrino oscillation physics has now entered the precision measurement era.

2.3.1 Solar Sector

Solar neutrino and long-baseline reactor neutrino experiments are sensitive to θ_{12} and Δm^2_{21} space. The disappearance of electron neutrinos from the sun has been measured by several experiments such as Homestake [35], GALLEX [46], SAGE [47], Borexino [48], SNO [49]. These results were confirmed by KamLAND [50] via the disappearance of electron antineutrinos from reactors in long baseline. Combined best fit values are $\Delta m^2_{21} = 7.37^{+0.17}_{-0.16} \times 10^{-5}$ eV^2 and $\sin^2\theta_{12} = 0.297 \pm 0.017$ from [1].

2.3.2 Atmospheric Sector

Atmospheric neutrino and long-baseline accelerator neutrino experiments are sensitive to θ_{23} and $|\Delta m^2_{32}|$ space. The disappearance of atmospheric muon neutrinos has been measured by experiments such as Super-K [38], MINOS [51], MACRO [52] and SOUDAN 2 [53]. This result was confirmed by long-baseline accelerator neutrino experiments (K2K, MINOS) by observing ν_μ disappearance. Combined best fit values for NH (IH) are $|\Delta m^2| = 2.50 \pm 0.04 \times 10^{-3}$ eV^2 ($2.46^{+0.05}_{-0.04} \times 10^{-3}$ eV^2) and $\sin^2\theta_{23} = 0.437^{+0.033}_{-0.02}$ ($0.569^{+0.028}_{-0.051}$) from [1]. Δm^2 is defined as $m_3^2 - (m_1^2 + m_2^2)/2$, with $+\Delta m^2$ for NH and $-\Delta m^2$ for IH.

Octant of θ_{23}

It was not yet determined whether the mixing angle θ_{23} is exactly at maximal ($\theta_{23} = \pi/4$). If not, whether the angle is larger or smaller than $\pi/4$. In the case of $\theta_{23} > \pi/4$ is referred to as the higher octant, and the case of $\theta_{23} < \pi/4$ is referred to as the lower octant.

It is harder to determine the octant of θ_{23} relying solely on ν_μ disappearance channel because the oscillation probability for this channel has a parameter dependence of the form $\sin^2 2\theta_{23}$. Therefore it was combined with ν_e channel to look for other subdominant oscillation effects. Combined ν_μ disappearance and ν_e appearance analyses have been made by MINOS and T2K and results are consistent with maximal mixing, $\theta_{23} = \pi/4$. Although recent ν_μ disappearance

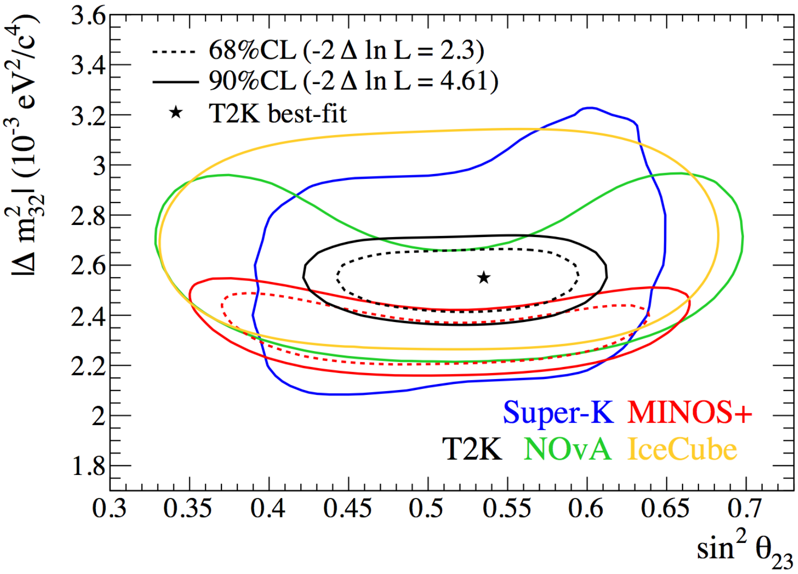

Figure 2.4: Comparison of the 68% and 90% confidence contours on the atmospheric oscillation parameters derived from the T2K, NOvA [3], MINOS+ [4], Super-Kamiokande [5], and Ice-Cube [6] experiments. The IceCubes log-likelihood profiles for individual oscillation parameters are also shown (right and top). NH is assumed. Figure taken from [7].

result from NOvA shows maximal mixing is disfavoured by 2.6σ [54], the result is still statistical-error dominated and will need further data taking to draw firm conclusions.

2.3.3 Accelerator and Reactor Sector

Short-baseline reactor neutrino and long-baseline accelerator neutrino experiments are sensitive to measure θ_{13}. The non-zero value of θ_{13} was first reported by T2K by observing ν_e appearance from a ν_μ beam in 2011 then followed by measurement from Daya Bay [42] by observing $\overline{\nu}_e$ disappearance from reactors in short baseline in 2012. Currently, θ_{13} is very precisely measured by reactor neutrino experiments (Daya Bay, RENO [55] and Double Chooz [56]). Combined best fit values for NH (IH) are $\sin^2\theta_{13} = 0.0214^{+0.0011}_{-0.0009}$ $(0.0218^{+0.0009}_{-0.0012})$ from [1].

δ_{CP} constraints

δ_{CP} can be probed by taking the difference of equation 2.15 and 2.16 while δ only appears in sub-leading term. Therefore a good constraint on δ_{CP} can be obtained by combining reactor

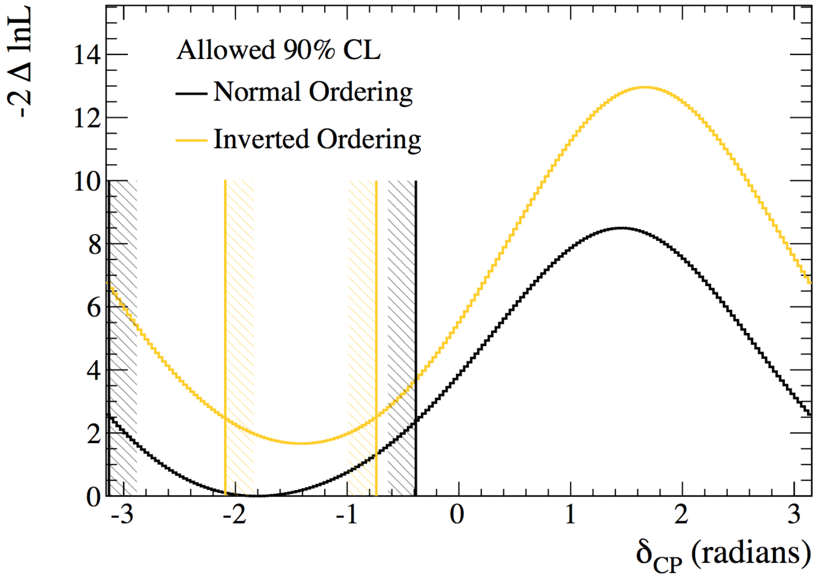

Figure 2.5: Preferred values of δ_{CP} from T2K 2016 analysis. The $2\Delta\ln\mathcal{L}$ value as a function of δ_{CP} for normal hierarchy (black) and inverted hierarchy (yellow). The likelihood is marginalised over $\sin^2 2\theta_{13}$, $\sin^2\theta_{23}$ and Δm^2_{32} . The vertical lines correspond to the allowed 90% confidence intervals, evaluated by using the Feldman-Cousins method. The δ_{CP} regions with values above the lines are excluded at 90% CL. Figure taken from [7].

$\overline{\nu}_e$ disappearance results with long baseline ν_e appearance results. T2K published results in 2016 [43] showing that δ_{CP} is excluded in some region at 90% using combined ν_e appearance results with θ_{13} value from reactor experiments. The result is shown in figure 2.5.

NOvA published their first results of ν_e appearance measurement [8] in 2016. They found a 3.3σ excess of events above background which disfavours $0.1\pi < \delta_{CP} < 0.5\pi$ in the inverted mass hierarchy at the 90% C.L (see Figure 2.6). The result is consistent with T2K.

2.4 Current Knowledge of Oscillation Parameters

A summary of the latest results of oscillation parameters are shown in Table 2.1.

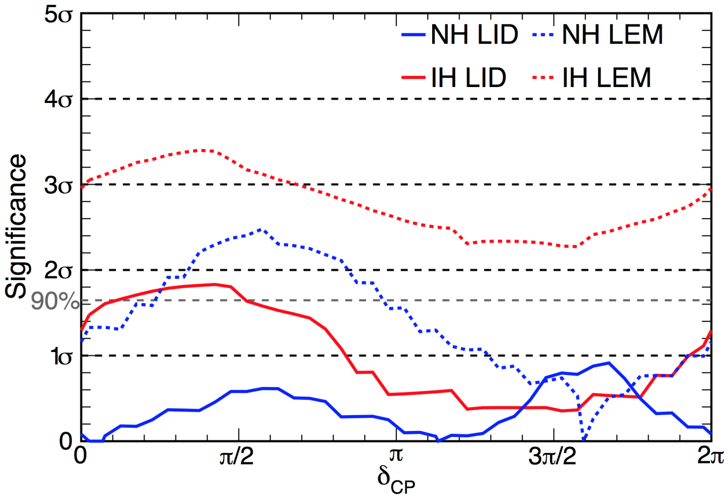

Figure 2.6: Results from NOvA 2016 ν_e appearance analysis. Significance of the difference between the selected and the predicted number of events as a function of δ_{CP} and the hierarchy. The primary (secondary) selection technique is shown with solid (dotted) lines. Figure taken from [8].

Table 2.1: Results of the global 3ν oscillation analysis, table taken from [1]. The CP violating phase $\delta$is taken in the (cyclic) interval $\delta/\pi \in [0,2]$.

Parameter	best-fit
Δm^2_{21}	$7.37^{+0.17}_{-0.16} \times 10^{-5}$ eV^2
$\sin^2\theta_{12}$	0.297 ± 0.017
Δm^2_{32} , NH	$2.50 \pm 0.04 \times 10^{-3}$ eV^2
Δm^2_{32} , IH	$2.46^{+0.05}_{-0.04} \times 10^{-3}$ eV^2
$\sin^2\theta_{23}$, NH	$0.437^{+0.033}_{-0.02}$
$\sin^2\theta_{23}$, IH	$0.569^{+0.028}_{-0.051}$
$\sin^2\theta_{13}$, NH	$0.0214^{+0.0011}_{-0.0009}$
$\sin^2\theta_{13}$, IH	$0.0218^{+0.0009}_{-0.0012}$
δ/π, NH	$1.35^{+0.29}_{-0.22}$
δ/π, IH	$1.32^{+0.35}_{-0.25}$

Although many of the oscillation parameters are measured to high precisions (error of the order of a few %), there are still many unresolved questions in the neutrino physics field that have not been answered yet. In the following section I will outline the unresolved questions.

2.4.1 Existence of sterile neutrinos

In 1996, LSND (Liquid Scintillator Neutrino Detector) measured an excess of $\overline{\nu}_e$ events when looking for $\overline{\nu}_e$ appearance in $\overline{\nu}_\mu$ beam [9]. With this excess coming from $\overline{\nu}_\mu \to \overline{\nu}_e$. The range

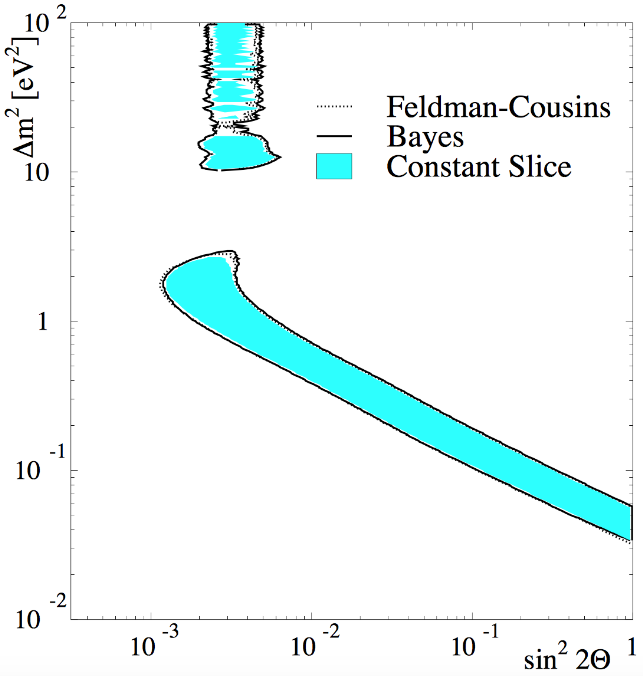

Figure 2.7: 90% CL region from the LSND appearance analysis. Figure taken from [9].

of parameters allowed by LSND is quite large, as shown on Figure 2.7. The data suggest that neutrino flavour oscillations occur with a Δm^2 in the range of $0.2 - 10$ eV^2. This large mass-squared splitting of the order of 1 eV^2 is substantially larger than $|\Delta m^2_{atm}| + |\Delta m^2_{solar}|$. Also, given the 3 independent mass splitting implies that there are at least 4 neutrino species. While the number of light neutrino species was determined to be three from the study of Z^0 decay, which means the other neutrino must be sterile i.e. they do not couple to the weak interaction. Such neutrinos are referred to as “sterile neutrinos”. The excess can be interpreted as the neutrino oscillation through the sterile neutrino $\overline{\nu}_\mu \rightarrow \overline{\nu}_s \rightarrow \overline{\nu}_e$.

MiniBooNE [57] also saw the excess and indicated the existence of sterile neutrino, while experiments such as KARMEN [58] and NOMAD [59] showed negative indications with their $\nu_\mu \rightarrow \nu_e$ ($\overline{\nu}_\mu \rightarrow \overline{\nu}_e$) searches.

A re-analyses of short baseline (SBL) reactor neutrino oscillation data using new reactor $\overline{\nu}_e$ fluxes [60] showed a possible disappearance of the reactor $\overline{\nu}_e$ (“reactor neutrino anomaly”) which could be a hint of existence of sterile neutrinos. Radioactive source calibration data from GALLEX [46] and SAGE [47] experiments also showed a deficit of the measured fluxes compared to the expected fluxes ("Gallium anomaly") which could be interpreted as hints for ν_e disappearance. While Daya Bay recently searched for relative spectral distortion in their reactor $\overline{\nu}_e$ data and showed negative indications of sterile neutrino mixing [61]. Dedicated experiments are planned in the next five years to exclude or confirm the remaining parameter space opened by all these anomalies.

2.4.2 Absolute mass of neutrinos and Dirac/Majorana masses

Neutrino oscillation experiments cannot provide information the absolute mass of neutrinos since the oscillation probability depends on the mass squared differences. By measuring the spectrum of electrons near the end point in ^{3}H β-decay ($^3\text{H} \rightarrow ^3\text{He} + e^- + \overline{\nu}_e$) the mass of $\overline{\nu}_e$ can be probed. Experiments such as KATRIN [62] is planned to reach sensitivity of $m_{\overline{\nu}_e} \sim 0.20$ eV by observing tritium-β-decay. The sum of the neutrino masses Σ can also be probed by cosmological measurements and are measured by the Planck Collaboration to be $\sum_j m_j <$ 0.23 eV at 95% C.L. [63]. The ratio of this upper limit of neutrino mass with masses of leptons/quarks are $\lesssim \mathcal{O}(10^{-6})$ which indicates the smallness of neutrino masses. A natural explanation of this is provided by the see-saw mechanism. Following from Section 2.2.3 if we combine equation 2.2 and 2.3 we have the full neutrino mass Lagrangian as:

$$\mathcal{L} = \frac{1}{2} \begin{pmatrix} \overline{\psi_L} & \overline{\psi_R^C} \end{pmatrix} \begin{pmatrix} 0 & m_D \\ m_D & m_M \end{pmatrix} \begin{pmatrix} \psi_L \\ \psi_R^C \end{pmatrix}, \tag{2.21}$$

The light and heavy neutrino masses can be obtained by diagonalising neutrino mass matrix M, which gives m_D^2/m_M and m_M respectively. And Δm^2 from experimental results ($\mathcal{O}(10^{-2})$ eV) can be reproduced for $m_M \sim 10^{14-15}$ GeV, which can potentially explain the fact that neutrinos have much smaller mass than the charged fermions.

If neutrinos were Majorana particles, lepton number violating process such as neutrinoless double beta decay ($0\nu\beta\beta$) would be allowed: $(A, Z) \rightarrow (A, Z+2) + e^- + e^-$, with the total lepton charge L changes by 2. Also, measuring the half-life or decay rate of this process [64] can give the absolute neutrino mass scale. Ongoing experiments searching for this process are

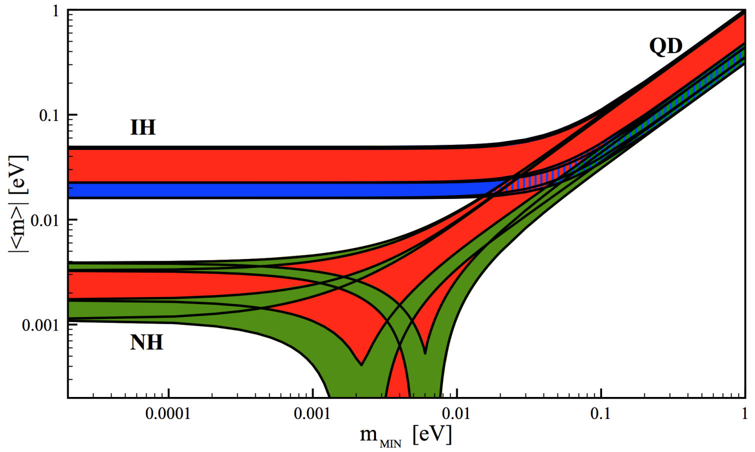

Figure 2.8: The effective Majorana mass ($|m_{\beta\beta}|$) as a function of the lightest neutrino mass (m_{min}) including a 2σ uncertainty. The top band corresponds to the IH regime, the bottom band corresponds to NH, with a degenerate region at high $|m_{\beta\beta}|$ and m_{min}. Figure from [10].

for example: SNO+ [65], KamLAND-Zen [66], GERDA [67] and MAJORANA [68]. The next generation ^{76}Ge experiment, LEGEND [69], is a proposed tonne-scale ^{76}Ge experiment that aims to build on the successes of GERDA and MAJORANA which is capable of discovery level sensitivity of $0\nu\beta\beta$ half-life of 10^{28} years, comparing to current sensitivity of 10^{25} years [70]. Figure 2.8 shows the possible values for the effective Majorana neutrino mass ($|m_{\beta\beta}|$) implied by neutrino oscillation data. Combining the knowledge of the mass hierarchy from oscillation experiments we would be capable of revealing the mass structure of neutrinos in the future.

2.4.3 Matter-Antimatter Asymmetry and Leptogenesis

It is clear that asymmetry exist between matter and antimatter in the Universe. Not only are we surrounded by matter, but also at larger scale if there were the same cluster galaxies as anti-galaxies, we should have seen strong γ-ray emission from annihilations. While it is believed that equal amount of matter and anti-matter were created in the Big Bang, the asymmetry we observe now must have been generated dynamically early in the history of the universe.

To dynamically generate a baryon asymmetry in the expanding early Universe the Sakharov conditions [71] have to be met:

- Baryon number violation: This condition is required in order to evolve from an initial state of baryon number symmetric to a baryon number asymmetric state.

- C and CP violation: If there is no C or CP violation, then processes involving baryons would proceed at precisely the same rate as the C- or CP-conjugate processes involving antibaryons, so there would be no baryon asymmetry effect generated.

- Out of equilibrium dynamics: Already satisfied by condition 1, there are no asymmetries in quantum numbers that are not conserved in chemical equilibrium.

Although evidence of CPV has been found in the quark sector, it is not sufficient enough to explain the asymmetry exist between matter and antimatter [72]. Lepton mixing allows for a new source of CP violation that can be studied with neutrinos. And CPV through δ_{CP} may be sufficient source for leptogenesis [73]. The leptogenesis mechanism proposed by Fukugita and Yanagida [74] presumes the existence of right-handed heavy Majorana neutrinos via the see-saw mechanism as described in section 2.4.2. These neutrinos could provide the extra source of CPV that could contribute to the lepton number violation ($\Delta L \neq 0$). The observation of $0\nu\beta\beta$ decay which is a lepton number violating process will also constitute a strong hint for leptogenesis. This lepton number asymmetry could be converted into baryon asymmetry by sphaleron processes in SM where anti-baryon are converted to leptons, anti-leptons are converted to baryons.

Thus, leptogenesis provides a natural extension to the SM that can give explanations to both the smallness of neutrino masses and baryon asymmetry. While leptogenesis gives an ideal way to provide a link between neutrino masses and matter-antimatter asymmetry, this may not necessary be the case and that there are many other models that could also provide explainations to what we observed. Nonetheless having a precise measurements of the light neutrino oscillation parameters allows different models to be tested, which could help understanding both early Universe history in cosmology and physics beyond the SM.

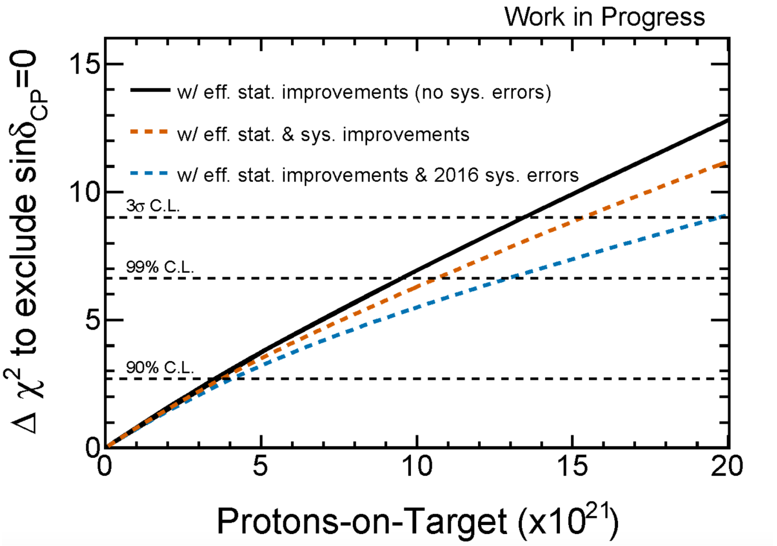

Figure 2.9: Sensitivity to CP violation as a function of POT with a 50% improvement in the effective statistics, assuming normal hierarchy and $\delta_{CP} = -\pi/2$. This shows a comparison between different assumptions for the T2K-II systematic errors with $\sin^2\theta_{23} = 0.50$. Figure from [11].

2.4.4 Future Prospect

Currently, the statistical error is predominant in neutrino oscillation measurements in T2K. Therefore it is important for T2K to accumulate more data. T2K has proposed an extended run (T2K-II) [11] which increase the current approved exposure of 7.8×10^{21} POT to 20×10^{21} POT. The sensitivity to CPV would improve significantly with the additional statistics. Figure **??** shows the expected evolution of the sensitivity to CP violation as a function of POT assuming that the T2K-II data is taken in roughly equal alternating periods of ν-mode and $\overline{\nu}$ -mode (assuming normal hierarchy and $\delta_{CP} = -\pi/2$. With the MR beam power eventually reaching 1.3 MW from current 450 kW, together with beamline and near detector upgrades, T2K could observe CPV with sensitivity greater than 3σ with proposed 20×10^{21} POT. A significant reduction of other oscillation parameters intervals are also possible.

NOA has a longer baseline (810 km) and higher peak neutrino energy (2 GeV) than T2K which started operation in 2014. Because of a longer baseline, their ν_e appearance measurement is more sensitive to the matter effect. Therefore has a greater sensitivity to the mass hierarchy. We can give even stronger constraints on the oscillation parameters and the mass hierarchy by combining the neutrino oscillation measurements of the two experiments. T2K-II will be taking data until 2026 when the next generation large water Cherenkov detector called Hyper-Kamiokande (Hyper-K) is proposed to start operating. With DUNE [75] starting to operate at about the same time as Hyper-K we will have a bright future in answering the unresolved questions.

Chapter 3

The T2K experiment

3.1 Experimental Setup

T2K [12] is a long-baseline accelerator neutrino experiment that is designed to make precision measurements of the neutrino oscillation ν_μ disappearance parameters θ_{23} and Δm^2_{32} and observe ν_e appearance events to infer θ_{13}. The overview of the experiment is shown in Figure 3.1. An intense ν_μ beam is made at the Japan Proton Accelerator Research Complex (J-PARC), described in Section 3.2. The beam is measured by a near detector complex called ND280 (Section 3.3), which is 280 m downstream from the neutrino production point. It monitors the neutrino beam prior to oscillation and constrains the neutrino flux parameterisation and cross

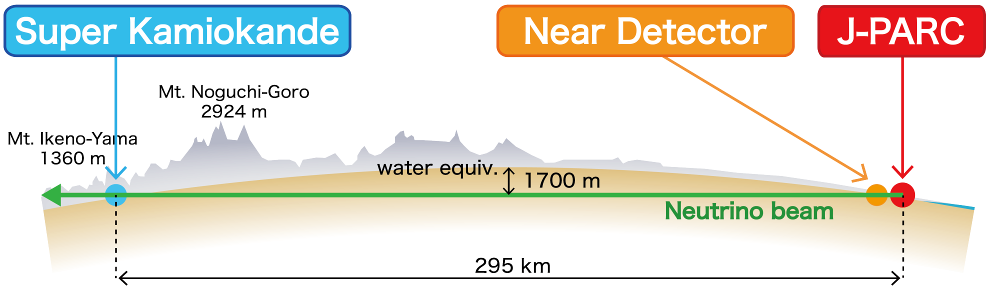

Figure 3.1: Overview of the T2K experiment.

sections. The beam is measured again at the far detector, Super-Kamiokande (SK), described in Section 3.11, which is 295 km from the production target in J-PARC.

3.2 Neutrino Beam

3.2.1 J-PARC Accelerators

J-PARC is located in Tokai, the eastern coast of Japan. It has a design power of 750 kW while it has been operating at 465 kW to date. The J-PARC beamline consists of 3 accelerators: LINear ACcelerators (LINAC), Rapid Cycling Synchrotron (RCS), and Main Ring (MR). First, an H^- beam is accelerated up to 400 MeV by the LINAC. At the downstream part of LINAC, electrons in H^- are removed by the carbon stripper foils and the stripped protons are delivered to the RCS. The RCS accelerates the proton beam up to 3 GeV and has a 25 Hz cycle and two bunches in each cycle. Around 5% of the beam bunches are supplied to the MR. The proton beam injected into the MR is accelerated up to 30 GeV and is delivered to the neutrino beamline. The rest of the beam is used in the muon and neutron beamline at J-PARC for other experiments. The MR beam has eight bunches and these are extracted within a single turn for use by the neutrino beamline. The eight bunches are separated by 500 ns, and this information is communicated to the far detector via a GPS system in order to trigger on the bunches.

3.2.2 Neutrino Beamline

The neutrino beamline, where each proton beam spill is extracted from the MR, consists of a primary beamline and secondary beamline. Figure 3.2a shows an overview of the neutrino beamline. The primary beamline transports and focuses the extracted proton beam to point towards the far detector. The secondary neutrino beam line consists of the target station, decay volume and the beam dump. This is shown in figure 3.2b. The bunches are incident upon a proton target which is comprised of a graphite rod of length 91.4 cm and diameter 2.6 cm which is cooled by a helium gas flow. The protons interact with the graphite to produce

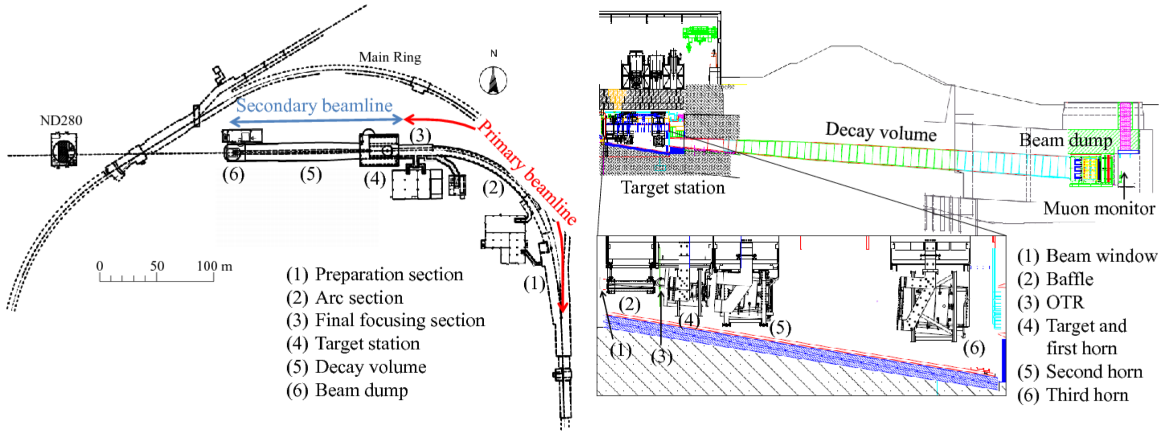

(a) (b)

Figure 3.2: Left: Overview of the T2K neutrino beamline. Right: Sideview of the secondary beamline. All of the components in the beamline (the target, horns, decay volume and beam dump) are contained in a single volume of 1500 m^3 filled with helium gas. Figure from [12].

large quantities of mesons, primarily pions along with kaons. These mesons are focused by three consecutive electromagnetic horns. Each horn consists of two coaxial (inner and outer) conductors which encompass a closed volume [76, 77]. A toroidal magnetic field is generated in that volume. The current driving the magnetic horns can be changed to deflect positive (negatively) charged mesons to create a neutrino (antineutrino) beam. These are referred to as Forward Horn Current (FHC) mode and Reverse Horn Current (RHC) mode.

As the mesons travel through the decay volume of 96 m, they decay to produce muon neutrinos according to equation 3.1 and antineutrinos according to equation 3.2.

$$\pi^+ \rightarrow \mu^+ + \nu_\mu \quad \text{and} \quad K^+ \rightarrow \mu^+ + \nu_\mu \tag{3.1}$$

$$\pi^- \rightarrow \mu^- + \overline{\nu}_\mu \quad \text{and} \quad K^- \rightarrow \mu^- + \overline{\nu}_\mu \tag{3.2}$$

However, the resulting neutrino beam is not pure because there is a small contamination of intrinsic ν_e /$\overline{\nu}_e$ due to these decays:

$$K^+ \rightarrow \pi^0 + e^+ + \overline{\nu}_e \quad \text{and} \quad \mu^+ \rightarrow e^+ + \nu_e + \overline{\nu}_\mu \tag{3.3}$$

$$K^- \rightarrow \pi^0 + e^- + \nu_e \quad \text{and} \quad \mu^- \rightarrow e^- + \overline{\nu}_e + \nu_\mu \tag{3.4}$$

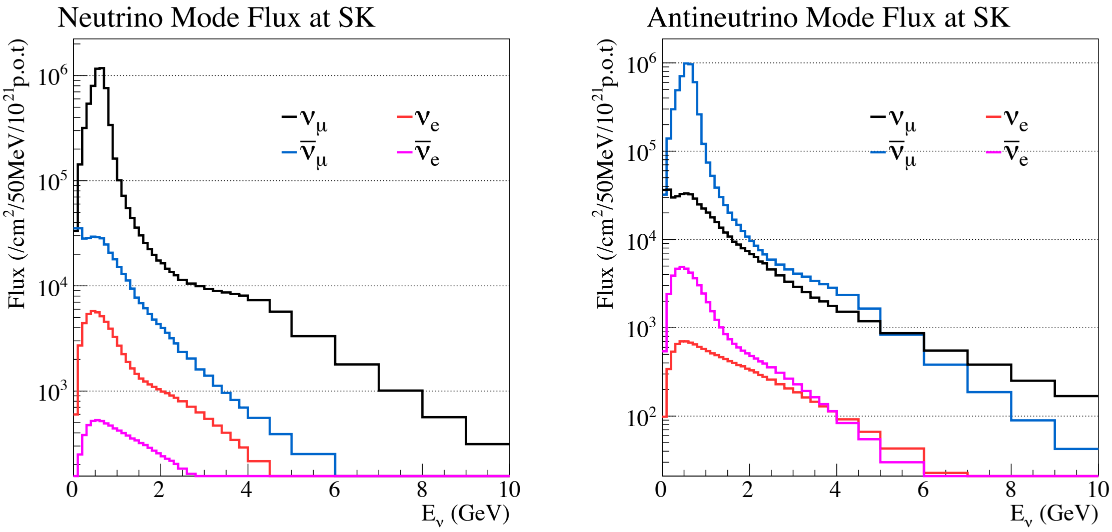

Figure 3.3: The SK flux prediction for Runs 1-8 with horns operating in 250 kA mode (FHC) on the left and -250 kA mode (RHC) on the right, broken down by neutrino flavour. Figure from [13].

for FHC and RHC respectively. Note the wrong-sign contamination ($\overline{\nu}$ in ν beam and ν in $\overline{\nu}$ beam) is much larger in RHC than in FHC. This is due to wrong-sign neutrinos being produced in meson decays. Since the beam originates from positively-charged protons we expect more positively-charged meson in FHC than negatively-charged meson in RHC. This is illustrated in figure 3.3 which shows the neutrino flux prediction at the far detector separately for each neutrino flavour (ν_μ , $\overline{\nu}_\mu$, ν_e and $\overline{\nu}_e$) for FHC mode (left) and RHC mode (right).

The muons produced in the meson decays are stopped in the beam dump at the end of the decay volume, these are measured by the muon monitors (MUMON) to monitor the beam flux and beam direction on a bunch-by-bunch basis.

3.2.3 The Off-Axis Technique

T2K is the first experiment to employ the off-axis technique [78] where the neutrino beam axis is displaced from the direction to the far detector. If we consider the 4-momentum of the outgoing neutrino in the pion rest frame:

$$p_\nu = (E_\nu, E_\nu \text{ sin } \theta, 0, E_\nu \text{ cos}\theta), \tag{3.5}$$

where E_ν is the neutrino energy and θ is the angle relative to the pion direction. Boosting by $-\beta$ so that the neutrino appears to be moving by $+\beta$ along direction of the pion, the 4-momentum of the outgoing neutrino in the lab frame can be written as:

$$p_\nu = (\gamma E_\nu^{'}(1+\beta\text{cos}\theta^{'}), E_\nu^{'}\text{sin}\theta^{'}, 0, \gamma E_\nu^{'}(\beta+\text{cos}\theta^{'})), \tag{3.6}$$

where $\gamma = E_\pi/m_\pi$ and $\beta = v_\pi/c$. Taking the ratio of x and z-component of eq. 3.6, a relation for the angle θ between the neutrino and pion can be written as:

$$\text{tan}\theta = \frac{E_\nu^{'}\text{sin}\theta^{'}}{\gamma E_\nu^{'}(\beta+\text{cos}\theta^{'})} \approx \frac{E_\nu^{'}\text{sin}\theta^{'}}{E_\nu}, \tag{3.7}$$

assuming $E_\pi \gg m_\pi$ and therefore $\beta \approx 1$. Since $\text{sin}\theta'$ cannot exceed unity, the maximum allowed angle for a given neutrino energy E_ν is:

$$\text{tan}\theta_{max} = \frac{E_\nu^{'}}{E_\nu} = \frac{29.8 \text{ MeV}}{E_\nu}, \tag{3.8}$$

where

$$E_\nu^{'} = \frac{(m_\pi^2 - m_\mu^2)}{2m_\pi^2} = 29.8 \text{ MeV}, \tag{3.9}$$

Therefore, for a given off-axis angle, the maximum neutrino energy is

$$E_\nu^{'max} = \frac{29.8 \text{ MeV}}{\text{tan}\theta}. \tag{3.10}$$

This is illustrated in Figure 3.4a. The neutrino beam is chosen to be 2.5° away from SK, producing a narrow-band of ν_μ beam, such that the energy peaks at $E_\mu = 2.54 \times \Delta m_{32}^2 L/\pi \approx 0.6$ GeV for $L = 295$ km and $\Delta m_{32}^2 = 2.5 \times 10^{-3}$ eV^2. This corresponds to the first oscillation minimum of the ν_μ survival probability at SK (see Figure 3.4b). Another benefit of applying this technique is to reduce backgrounds outside the energy range of interest.

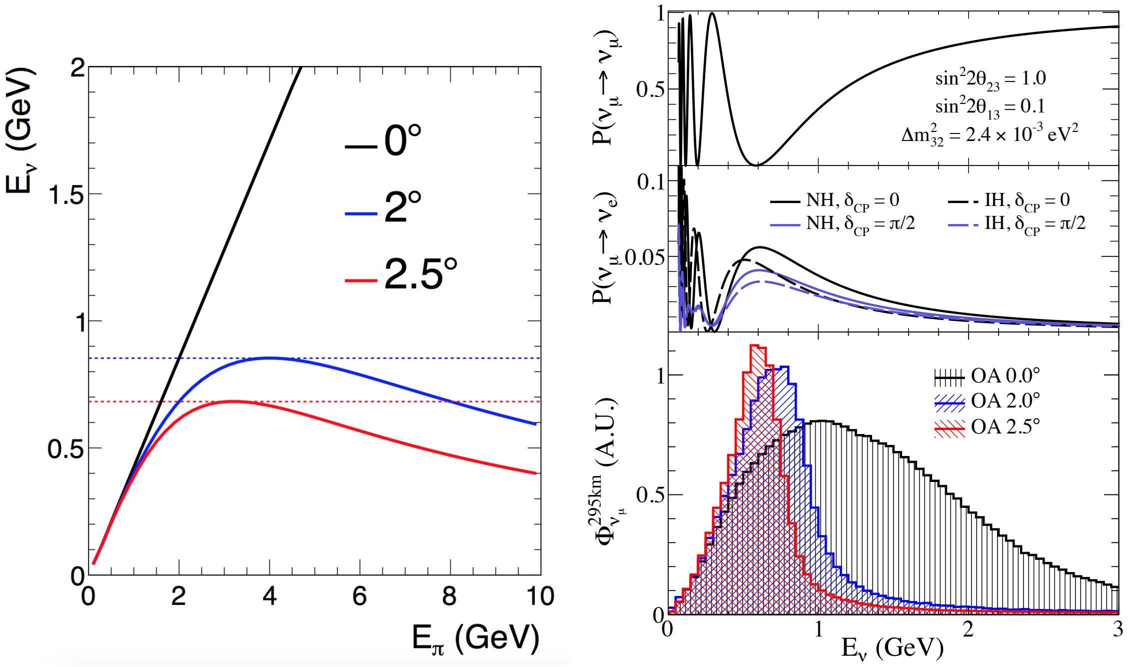

(a) (b)

Figure 3.4: Left: Neutrino energy dependence on pion energy for on-axis and two off-axis angles. Dotted lines show the maximum neutrino energy for the two off-axis angles using equation 3.10. Right: Muon neutrino survival probability (top), electron neutrino appearance probability (middle) at the far detector and the muon neutrino flux for different off-axis angles in the neutrino mode (bottom) as a function of neutrino energy. Figure from [14].

3.3 The T2K Near Detectors

A set of detectors are located 280 m from the production target to measure the neutrino energy spectrum, flavour content, and interaction rates of the unoscillated beam and are used to tune the prediction at the far detector. This near detector complex consists of two detectors: on-axis detector INGRID and off-axis detector ND280. All the detectors use the same coordinate convention: z is along the nominal neutrino beam axis, and x and y are horizontal and vertical respectively.

3.3.1 INGRID

The Interactive Neutrino GRID (INGRID) [15] is centred on the proton beam axis to directly monitor the neutrino beam profile and intensity. It is made up of 14 identical iron/scintillator modules arranged as two identical groups of 7 along the horizontal and vertical axis, and 2 more identical modules are placed at off-axis positions off the main cross, as shown in figure 3.5 to monitor the asymmetry of the beam.

INGRID detects about 10-20k events per day with a beam power around 100 kW. This sufficient statistics allows the neutrino beam profile to be monitored with 4% precision and determine neutrino beam direction with a precision of 10 cm or 0.4 mrad. These measurements determine the off-axis angle for ND280 and SK precisely to help reduce the systematic uncertainty on the neutrino energy spectra and absolute flux.

3.3.2 ND280

The off-axis detector ND280 needs to achieve several requirements in order to serve its purpose. Firstly, it needs to determine the ν_μ flux spectrum prior to oscillation to be able to propagate the prediction to the far detector. Secondly, it is intented to measure the ν_e component of the neutrino beam (or intrinsic ν_e) as this is an irreducible background for ν_e appearance search at SK ($\approx 1\%$ of ν_μ flux). Finally, it needs to be good at separating CC and NC interaction

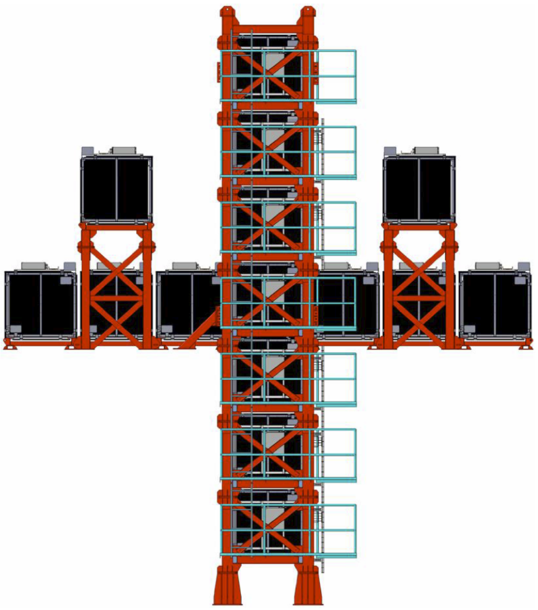

Figure 3.5: INGRID on-axis near detector. The 16 identical modules sample the neutrino beam in a transverse section of 10 m × 10 m . The center of the cross, with two overlapping modules, corresponds to the designed neutrino beam center. Figure from [15].

channels, in particular NCπ^0 and NCπ^+ which are backgrounds for ν_e and ν_μ analyses at SK. In order to achieve all of the above, the off-axis detector ND280 is composed of many sub-detectors as shown in figure 3.6. It consists of the π^0 detector (P0D) and the tracker made up of three time projection chambers (TPCs) and two fine grained detectors (FGDs), all of which are placed in a metal frame container called the basket. An electromagnetic calorimeter (ECal) surrounds the basket, and all of these are contained in the recycled UA1 magnet instrumented with scintillator to perform as a muon range detector (SMRD).

UA1 magnet and Side Muon Range Detector (SMRD)

The UA1 magnet, donated by CERN, has a magnetic field of 0.2 T perpendicular to the neutrino beam direction applied by the coil and returned by the outer iron yoke. Since a water Cherenkov detector cannot distinguish the charge of particles coming from either a neutrino or antineutrino interaction, a good understanding of the wrong-sign background in the near detector is essential for the δ_{CP} search. The SMRD consist of scintillator slabs which are placed in the gaps of the iron yokes. It acts as a Cosmic trigger for calibration runs.

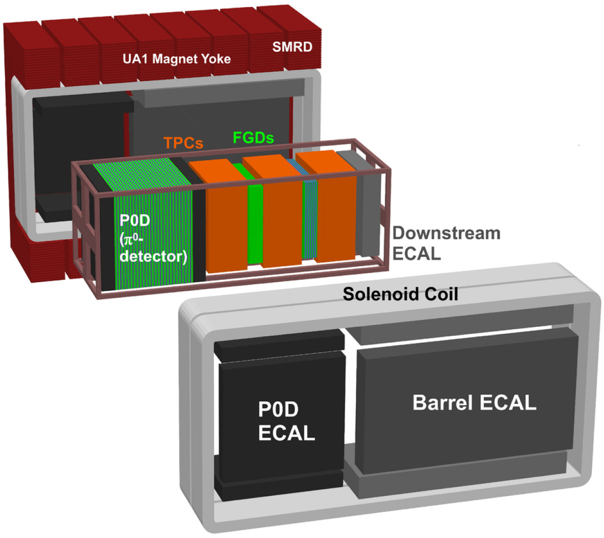

Figure 3.6: An exploded view of ND280. The neutrino beam comes from the left side. The P0D, the TPCs, and the FGDs are surrounded by the ECals. The SMRD is inter-spaced in the return yoke. The neutrino beam comes from the left side. Figure taken from [12].

π^0 Detector (P0D)

Situated at the most upstream end of the basket is the P0D, which is designed to measure π^0 production by the neutral-current process $\nu_\mu + N \rightarrow \nu_\mu + N + \pi^0 + X$ on water target with the same neutrino flux as the far detector. It is a scintillator detector consisting of fillable water target bags and lead and brass sheets interleaved with scintillator bars. It is necessary to have some water target in ND280; by having the same target material as the far detector, systematics due to different target materials can be cancelled out.

Tracker region

Downstream of the P0D is what it is described as the tracker region which consist of 2 FGDs sandwiched in 3 TPCs. FGD1 which sits on the upstream side is composed solely of scintillator trackers oriented alternately in x and y directions; FGD2 is composed of scintillator bars and water targets (similar to the P0D). They provide the main target mass for neutrino interactions as well as tracking of charged particles coming from the interaction vertex. By comparing the measured total energy deposit for a given particle range in the FGD to the theoretically expected

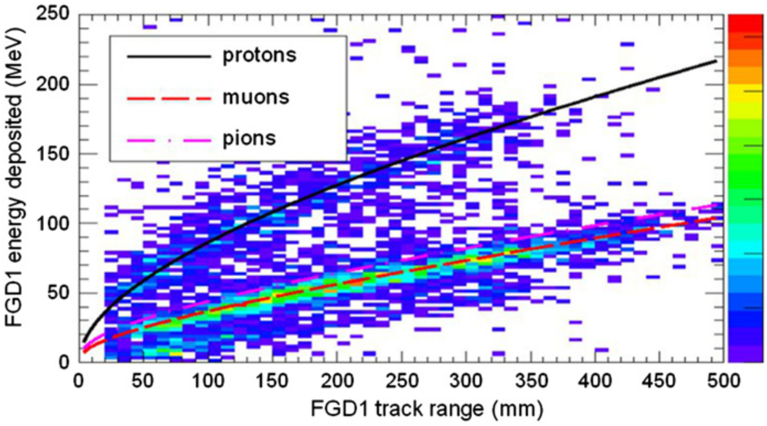

Figure 3.7: Deposited energy versus range for particles stopping in FGD1. The scatterplot shows stopping particles in neutrino beam data, while the curves show the MC expectations for protons, muons, and pions. Figure from [16].

energy deposit for particles with that range, protons can be distinguished from muons and pions. Figure 3.7 shows a scatterplot of deposited energy versus range for particles produced by neutrino interactions and stopping in FGD1. A clear population of protons can be distinguished.

Once an interaction occurs in one of the FGDs and the interaction products enter one of the TPCs, the TPCs can measure the particles with good momentum resolution and particle identification (PID). The TPCs are filled with an argon gas mixture that is ionised by passing charged particles. This allow 3D reconstruction of the charged particle trajectories. The momentum of each particle is determined from its curvature in the magnetic field with a resolution of $< 2\%$ below 1 GeV/c. PID is done by comparing energy loss and momentum of charged particles in the gas. The resolution of deposited energy is $7.8 \pm 0.2\%$ for minimum ionising particles, better than the design requirement of 10%. This allows muons to be distinguished from electrons in the TPCs. Fig. 21 shows the TPC PID capability by comparing energy loss and momentum for positively charged particles.

Electromagnetic Calorimeters (ECals)

The detectors contained in the basket are surrounded on all sides by the ECals to detect particles that exit the inner detectors and veto particles originating from outside. Each ECal consists of alternating planes of scintillator bars and lead for generating electromagnetic showers. The

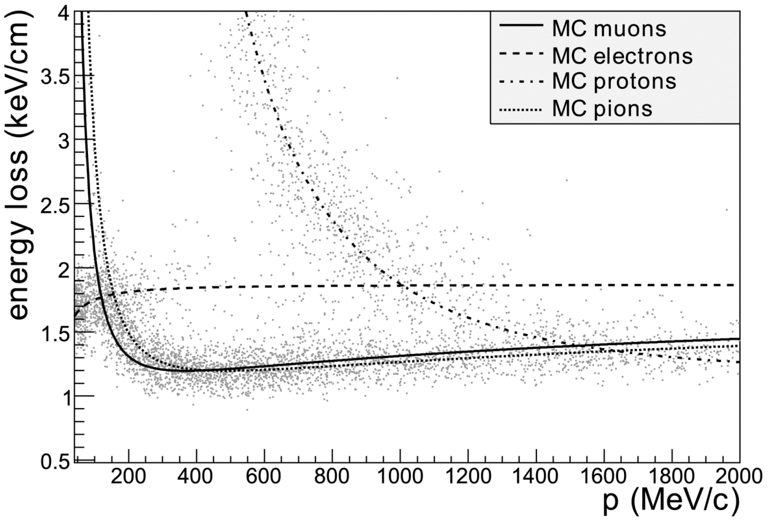

Figure 3.8: Each point shows measurements by a single TPC of the energy loss and momentum of positively charged particles produced in neutrino interactions. The curves show the expected relationships for muons, positrons, protons, and pions. Figure from [12].

tracker ECals are capable of detecting photons that originate from π^0 decays in the tracker and measuring their energies and directions [79].

3.4 The T2K Far Detector: Super-Kamiokande

Situated 295 km away from the production target in J-PARC is the far detector, Super-Kamiokande (SK) [80]. It is a 50 kt water Cherenkov detector located about 1 km deep in Mt. Ikeno. Figure 3.9 shows an overview of the detector. It has been operating since 1996 and the primary purposes of the detector are nucleon decay searches and the detection of neutrinos from various sources including solar, atmospheric, accelerator neutrinos and supernova relic neutrinos.

The detector is a cylindrical tank made up of stainless steel, 41.4 m tall and 39.3 m in diameter, it is filled with ultra-pure water. The volume is optically separated into two compartments by photomultiplier tubes (PMTs) - the inner detector (ID) and outer detector (OD). The inner detector (ID) is 36.2 m tall and 33.8 m in diameter. There are 11129 20-inch inward-facing PMTs on the ID wall corresponding to a spatial coverage of 40%. There are 1885 8-inch outward-facing PMTs on the OD wall which is covered with a high reflective material. The

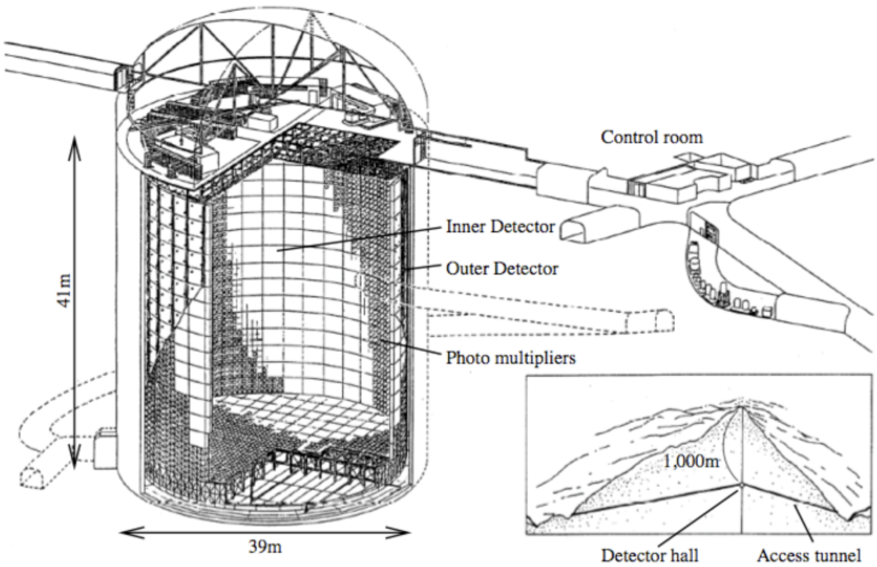

Figure 3.9: Diagram of the Super-Kamiokande Detector (taken from [17]).

purpose of the OD PMTs to veto background events like cosmic muons and to discriminate charged particles which exit the ID. The fiducial volume (FV) has recently been re-defined (see Section 5.3.1 for discussions). The timing and charge distributions of the PMTs provides kinematic information about neutrino such as vertex position, event timing, zenith and azimuthal angles to the neutrino beam axis, and momentum, numbers of ring and particle type.

When a charged particle passes through a medium at a speed greater than the speed of light in that medium, it emits Cherenkov light:

$$v > \frac{c}{n} \tag{3.11}$$

where c is the speed of light in vacuum and n is the index of refraction (1.33 for pure water). Therefore the Cherenkov threshold (which is the minimum energy to generate Cherenkov radiation) is given by:

$$E = \frac{m}{\sqrt{1-(1/n)^2}} \tag{3.12}$$

so particles with higher mass must have higher energy to be detected because they have a higher Cherenkov threshold.

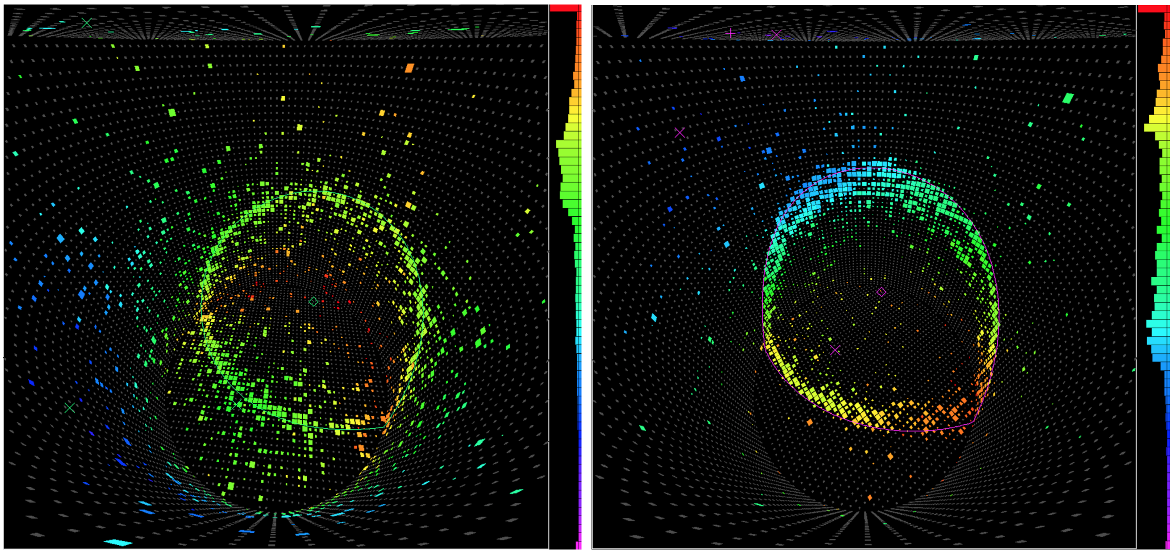

Figure 3.10: Example of a SK event displays: e-like ring (left) and μ-like ring (right). Figures taken from [18].

Cherenkov light is emitted in a cone with opening angle defined by:

$$\cos\,\theta_C = \frac{1}{\beta n} \tag{3.13}$$

where $\beta = v/c$. For ultra-relativistic particles ($\beta \approx 1$), $\theta_C \approx 42^\circ$ in water. In order to measure ν_μ disappearance and ν_e appearance we rely on a good particle identification (PID) to distinguish between electrons and muons at SK. Muons, because of their relatively large mass, are insensitive to changes in their momenta as they scatter on particles in water and therefore they produce a well-defined cone of Cherenkov radiation as they travel through the detector. They tend to produce a clear, sharp ring of PMT hits seen on the detector wall. Whereas electrons, because of their smaller mass, scatter more easily inside the detector. Electron-induced shower produces a“fuzzy” ring pattern seen by the PMTs, which can be thought of as the sum of many overlapping Cherenkov light cones. Figure 3.10 shows an example of event displays of typical neutrino events at SK. The sharpness of a ring can be used to distinguish between muons and electrons with $< 1\%$ of muon events being misidentified as electrons.

3.5 Simulations at T2K

In order to fully understand the T2K experiment we use Monte Carlo Simulation (MC) to model the neutrino flux, neutrino-nucleus interactions, and particle propagation and energy deposit in the detectors. Neutrino interaction simulation is detailed in the next chapter.

3.5.1 Flux Simulation

Neutrino flux simulation begins by simulating proton beam interacting with graphite target; the production of mesons in the target is modelled using data from the NA61/SHINE experiment [81]. NA61/SHINE experiment (SPS Heavy Ion and Neutrino physics Experiment) is a fixed target experiment which uses the CERN SPS accelerator. It studies the particles produced when a 30 GeV proton beam interacts with a graphite target. Other hadronic interactions inside the target and surrounding area are simulated using FLUKA [82]. Interactions outside the target are simulated using GEANT3/GCALOR [83, 84] with the interaction cross sections tuned to experimental data. The neutrino flux is estimated from the simulated kinematics of the particles that decay in the decay volume. Figure 3.3 shows the flux predictions at SK. The flux prediction and uncertainties used for the analysis described is this thesis is referred to as “13av2”.

3.5.2 Detector Simulation

Neutrino-nucleus interactions in both ND280 and SK are simulated primarily with NEUT [85]. Details about NEUT and how interactions modelled are described in the next chapter. SK detector response is simulated by SKDETSIM, a package that interfaces with GEANT3 [83]. The SK MC version used for the analysis described is this thesis is referred to as “14a”.

The scintillators and electronics response at ND280 are simulated using custom written software elecSim [12]. The simulation of final state particles in ND280 are performed using Geant4 [86], whereas NEUT is used in SK. Implications of this is described in the next chapter.

Chapter 4

Neutrino-nucleus interactions

To infer neutrino oscillation parameters in practice we compare the number of neutrino events measured at ND280 first to measure the neutrino spectrum before oscillations, and then at SK after the neutrinos have oscillated. In a simplified picture, the number of events in SK can be measured and compared to the prediction:

$$N_{SK} \sim P(\nu_\alpha \to \nu_\beta) \cdot \Phi_{SK}(E_\nu) \cdot \sigma(E_\nu) \cdot \epsilon_{SK}(E_\nu), \tag{4.1}$$

where N_{SK} is the number of predicted events at SK, $P(\nu_\alpha \to \nu_\beta)$ is the probability of oscillation, $\Phi_{SK}(E_\nu)$ is the initial flux, $\sigma(E_\nu)$ is the cross-section of the neutrino for ν_β to interact with water in SK, and $\epsilon_{SK}(E_\nu)$ is the SK detector efficiency.

In order to have good predictions on the number of events that are required to make precise measurements of oscillation parameters, we need good predictions of the neutrino flux, neutrino interaction simulation, SK detector simulation, beam intensity measurements, and near detector measurements to constrain flux and neutrino interaction uncertainties. Therefore a good understanding of the neutrino flux, detector response as well as neutrino interaction cross sections are essential in order to predict accurately the observables at the far detector, as the lack of understanding will result in non-neglectable systematic uncertainties when comparing measurements with predictions. In this chapter I will describe neutrino interactions at T2K,

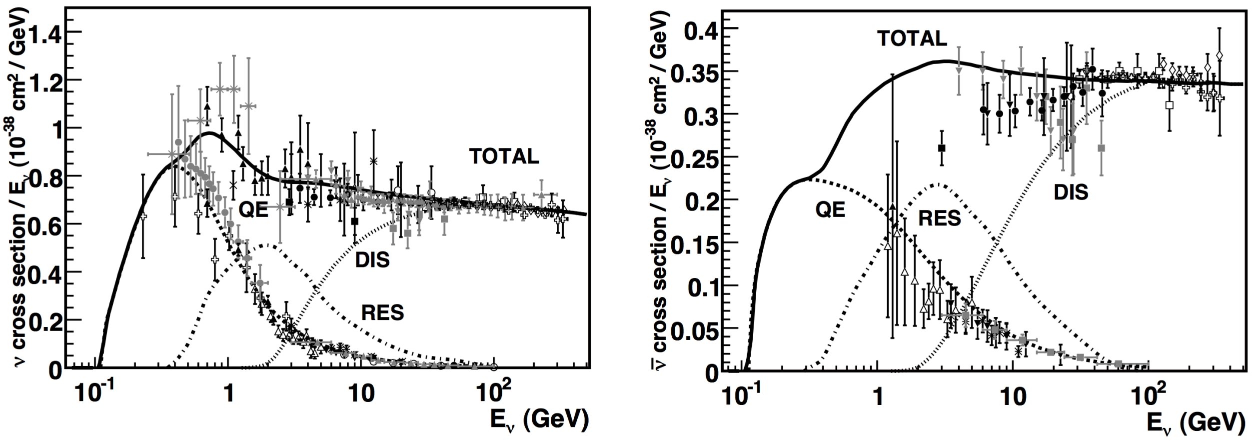

(a) ν (b) $\overline{\nu}$

Figure 4.1: ν and $\overline{\nu}$ per nucleon CC total cross sections as a function of neutrino energy. The dominant process at T2K peak energy of at 0.6 GeV is quasi-elastic scattering (QE), other processes such as resonance production (RES) and deep inelastic scattering (DIS) also possible in higher energy. Figures taken from [19].

with emphasis on my study on nucleon FSI using NEUT neutrino event generator and tuning nucleon FSI parameters using external scattering data. Comparison of predictions from various neutrino interaction event generators (NEUT [85], GENIE [87], Geant4 [86], NuWro [88] and FLUKA [82]) with thin-target nucleon scattering data. A new tune of the cascade model has been performed for improvements from the current NEUT parameters using external data.

4.1 Neutrino Interactions at T2K

According to the Standard Model, neutrinos can undergo charged-current (CC)and neutral-current (NC) weak interactions. Only the CC interactions are of interest for extracting oscillation parameters because the neutrino flavour can be implied from the charged lepton produced in the interaction, thus allowing us to determine whether neutrinos have changed flavour between the near and far detectors (as described in section 3.11).

The energy dependent neutrino interaction cross-sections for various interaction processes are shown in Figure 4.1. The dominant process at T2K peak energy of at 0.6 GeV is quasi-elastic scattering (QE), where the neutrino (antineutrino) interacts with a neutron (proton) from a nucleus to produce a proton (neutron) and a charged lepton of corresponding flavour, which can be written as:

$$\nu_l + n \rightarrow p + l^- \tag{4.2}$$

$$\bar{\nu}_l + p \rightarrow n + l^+ \tag{4.3}$$

Since it is a 2-body process, assuming the interaction occurs on a single bound nucleon at rest, the energy of the incoming neutrino can be reconstructed using the energy and direction of the lepton:

$$E_\nu^{\text{rec}} = \frac{m_p^2 - (m_n^2 - E_b)^2 - m_l^2 + 2(m_n^2 - E_b)E_l}{2(m_n - E_b - E_l + p_l \cos\theta_l)}, \tag{4.4}$$

where m_n, m_p and m_l are masses of neutron, proton and charged lepton, E_b is the neutron binding energy in oxygen (27 MeV) and E_l, p_l and θ_l are the energy of charged lepton, its momentum and its emission angle relative to the beam direction, respectively. In reality there will be uncertainties coming from imperfect nuclear modelling and interactions with nucleons that are not at rest in the nucleus.

Two other interaction modes are also relevant at T2K energy range: resonance production (RES) and deep inelastic scattering (DIS). While the dominant process is QE, there are contributions from RES at higher energies. There are also small contributions from DIS interactions at the high-energy tail of the neutrino spectrum, as shown in Figure 4.1. This could become problematic if processes are misidentified; If particles are missed or misidentified, such processes could be mistakenly identified as CCQE, resulting the neutrino energy being wrongly reconstructed.

Recently T2K has included a non-CCQE signal event to the oscillation analysis, which is RES interactions from ν_e : $\nu_e + p \rightarrow p + e^- + \pi^+$. Details about the event selections are in Section 5.3.2. However, in cases when the pion is emitted below Cherenkov threshold (and its decay products are not detected), only a single Cherenkov ring will be seen in the detector and such events will be considered as CCQE events which leads to neutrino energy being wrongly reconstructed. There are also further complications due to nuclear effects which will be described in Section 4.3.

4.2 NEUT: the Neutrino Event Generator

NEUT [85] is a MC neutrino event generator that is used to simulate neutrino interactions and their product particles based on theoretical models. It is the primary generator used in T2K and is capable of simulating the following neutrino CC and NC interactions:

- (Quasi-)elastic (QE) scattering: $\nu + N \rightarrow l(\nu_l) + N'$
- single meson or photon production via baryon resonance (RES): $\nu + N \rightarrow l(\nu_l) + N' + m$
- deep inelastic scattering (DIS): $\nu + N \rightarrow l(\nu_l) + N' + \text{hadrons}$
- coherent pion production (COH): $\nu + A \rightarrow l(\nu_l) + \pi + A$

where N and N' represent nucleons which can be either free or inside nucleus, l represents a lepton, m represents π, K, η, γ and A is the target nucleus.

For CCQE interactions, the Llewellyn-Smith formalism [89] is used to predict neutrino quasi-elastic scattering cross-section. The model contains several form factors, all of which can be measured by electron scattering experiments except the axial form factor, which is characterised by the axial vector mass parameter M_A^{QE}; the shape of the differential cross section as a function of Q^2 and the total cross section also depends on this parameter.

In a simple picture a neutrino interacts with one nucleon at rest, However nuclear effects should be considered since each nucleon is bound in a nucleus and has a Fermi momentum, and Pauli blocking effects where a nucleon cannot change to a new state that is already occupied by other nucleons. While the spectral function (SF) model [90] was used by default in NEUT to describe the momentum distribution of nucleons inside a nucleus, the RFG model by Smith and Moniz [91] was found to give a more realistic description than the SF model. Recently the relativistic Random Phase Approximation (RPA) correction has been included in NEUT which takes into account the long range nucleon-nucleon correlation that modifies the interaction strength as a function of four-momentum transfer, Q^2 [92]. These models have different effects to the energy distribution of CCQE events. While NEUT simulations are performed using SF

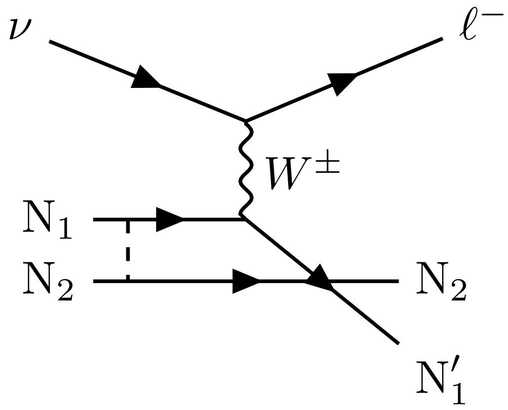

Figure 4.2: Feynman diagram of a charged current meson exchange current (CCMEC) interaction.

model, RFG+RPA model was chosen by fitting to external data sets [93] and therefore the MC are tuned to this model using a MC reweighting method.

In reality neutrinos can interact simultaneously with more than one nucleons. These interactions are referred to as the meson exchange current (MEC or 2p2h) [92] as the nucleons which interact with the neutrino are coupled via meson exchange. An example of this is shown in Figure 4.2. Since these interactions are indistinguishable from CCQE interactions at SK (nucleons are typically below Cherenkov threshold) the resulting reconstructed energy would be smaller than the true energy (since the reconstruction assumes a proton mass rather than a heavier nucleon-nucleon pair). Recent NEUT has included such interaction modelled by Nieves et al. [92]. Although multi-nucleon interactions should be possible for all processes, only CCQE process is considered for analysis purpose. Resonant meson production is modelled by the Rein-Sehgal model [94] with revised form factors from Graczyk and Sobczyk [95] and tuned using ANL and BNL bubble chamber data [96]. These interactions are considered in NEUT for $W < 2$ GeV/c^2. Pionless Delta decay (PDD) processes are considered in NEUT which takes into account the baryon resonance absorption. Coherent pion production is modelled by simulating the neutrino coherently scattering off the whole nucleus by Rein-Sehgal [97]. These interactions typically have small Q^2 so the angular distribution of the outgoing lepton and meson are peaked in the forward direction.

Deep inelastic scattering (DIS) is modelled by simulating production of multiple hadrons from neutrino scattering. The cross section for W > 1.3 GeV/c^2 is calculated using nucleon structure functions based on the GRV98 parton distribution functions [98]. Corrections in low Q^2 region is applied from Bodek and Yang [99] to improve the agreement with the experiments.

Summary of the neutrino interaction systematic parameters can be found in Section 6.4.3.

4.3 Modelling Nuclear Effects

When a neutrino interacts with a nucleus, the hadrons produced from a neutrino interaction must propagate through the nucleus before being observed in a detector. They can re-interact inside the nucleus and such re-interaction, which is called Final-state interactions (FSI), can affect the reconstruction of final state particles. Secondary interactions (SI) can occur when secondary particles from a neutrino interaction interact with materials inside a detector but outside of the target nucleus; these SI can also affect the kinematics of observed particles. These interactions can obscure the true interaction mode and could be problematic as mentioned in Section 4.1. Interactions of pions, kaons, etas and nucleons in the nucleus are all simulated in NEUT. A cascade model is used to model these interactions but implementations are slightly different for different hadrons.

Pion and nucleon FSI/SI are one of the dominant systematics in the near detector of T2K. The current treatment of systematic uncertainties of FSI/SI are independent, and different models of FSI/SI are used for near and far detector (c.f. Section 3.5.2). Unifying treatment of FSI/SI in T2K near and far detectors for nucleons and pions would allows us to have a consistent way of retuning free parameters in order to evaluate correlations between them. Since pions are the most frequently seen hadrons from neutrino interactions at T2K, pion FSI treatment has been rigouriously studied with a recent re-tune of the parameters [20], however proton FSI are becoming increasingly important for many current analyses and this effect hasn't been studied to be able to take into account in analyses. Unifying the treatment of FSI/SI would be a long term work and the following section shows the first step of achieving this aim.

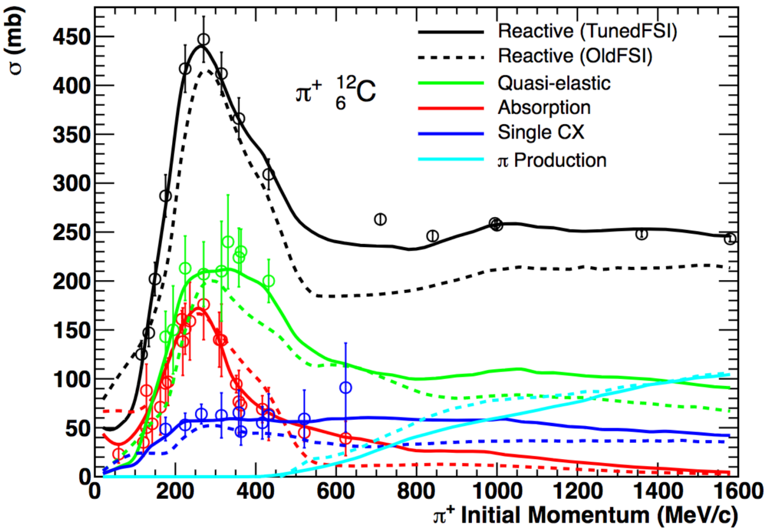

Figure 4.3: π^+-C cross-section predictions from NEUT, Different colours represent different interaction channels. The data points are measurements from π^+-C scattering experiments. The dash lines are predictions before tuning and solid lines are after tuning. Figure taken from [20].

4.3.1 The Cascade Model

NEUT simulates FSI using a semi-classical intra-nuclear cascade model. The hadron production vertex position is chosen based on a Woods-Saxon nuclear density profile [100] shown in Figure 4.5. The momentum of the initial hadrons are based on the neutrino interaction kinematics.

After a hadron is produced, it is propagate through the nucleus step-by-step. The step size is chosen as $dx = R_N/100$, where R_N is the size of the nucleus and is defined as 2.5 times the nuclear radius from [101]. The probabilities of each interaction are calculated at each step and a random number is generated to determine which, if any, interaction occurs at a given step. This allows the hadron to undergo multiple interactions during its journey through the nucleus. Pauli blocking effect is incorporated by requiring the nucleon momentum after interaction to be larger than the Fermi momentum. If no interactions occur at this step, the hadron are moved to the next step. This procedure is repeated until the hadron undergoes an interaction or when the hadron exits the nucleus.

For pions, momentum < 500 MeV/c, momentum and density dependence of the mean free path

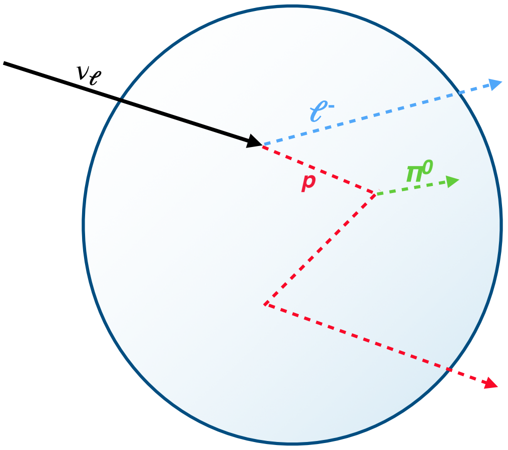

Figure 4.4: Schematic representation of the intra-nuclear cascade. In this example, the proton produced from a neutrino interaction undergoes single π production and elastic interactions before exiting the nucleus.

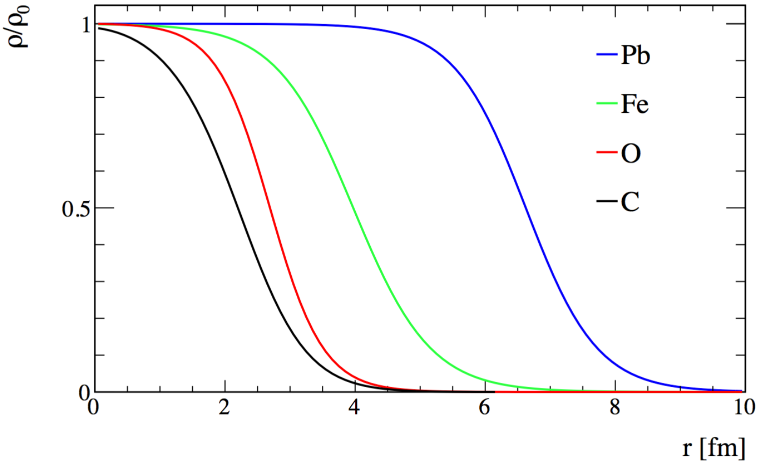

Figure 4.5: Normalised nuclear density distributions for various nuclei modelled by Woods-Saxon distributions.

(MFP) is calculated based on the Delta-hole model from Oset et. al. [102]. For higher momentum, MFP is calculated from free π-p scattering data. For nucleon FSI, MFP is calculated from free nucleon-nucleon cross-section using MECC-7 parameterisation [103]. There are seven scaling parameters to scale the microscopic interaction probabilities for the pion FSI model: three each for low-energy and high-energy region for Quasi-Elastic (QE), Absorption (ABS) and Charge Exchange (CX) microscopic scattering probabilities, and one parameter for overall scaling. For nucleon FSI model there was only one parameter for overall scaling, but three more parameters have been added with the same functionality as the pion FSI parameters, namely: Quasi-Elastic, single and double pion production microscopic interaction probabilities.

4.4 Proton scattering simulation

NEUT has been modified so that it can simulate proton scattering MC events. MC are generated by simulating large number of protons scattering on a carbon target with uniform energy spectrum. Interaction channels are defined based on final state (FS) particles for each event:

- Quasi-elastic (QE) Scattering: Only 1[1] proton in the FS.
- Single π production (SPD): Only 1 pion (of any charge) in the FS. Equal probabilities are assigned to produce the pion of any charge in order to keep the model simple.
- Double π production (DPD): Only 2 pion (of any charge) in the FS.

Pions produced from single/double π production can subsequently undergo the FSI cascade routine. The cross-section for each channel can be found using:

$$\sigma_i = \pi R_N^2 \frac{N_i}{N_T}, \tag{4.5}$$

where N_i is the number of events selected and N_T is the total number of events generated. Figure 4.6 shows the proton-Carbon scattering cross-section predictions for each interaction

---

[1] Although this is a common definition of a quasi-elastic event, it will be shown later that NEUT is not capable of simulating such events.

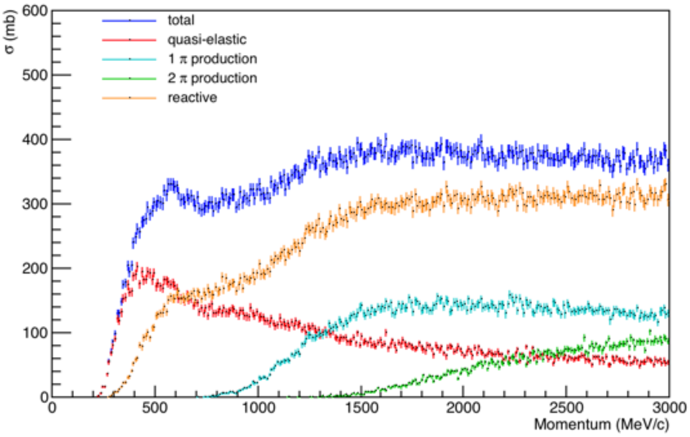

Figure 4.6: NEUT interaction cross-sections predictions of p-C scattering as a function of momentum of the incident proton. The reactive cross-section prediction here is defined as total minus quasi-elastic process.

channel. It is natural to divide the interaction categories based on what kind of microscopic interactions are available in the FSI model (see Section 4.3.1), although it should be emphasised that in cases such as only one pion in FS, it could be a result from a DPD interaction with a pion absorbed during the cascade while it doesn't necessary imply a SPD interaction has occurred. Note that the total cross-section prediction is not the same as sum of all three interaction channels; N_i is selected whenever a proton interacts and this includes events which have multiple nucleons in FS. The reactive cross-section prediction here defines as total minus quasi-elastic process. There is a parameter which scales the microscopic probability of interactions at each step. Three scaling parameters are added which scale the probability of each of the three interactions. The effect of varying each of these scaling parameters on the cross-section predictions are illustrated in Figure 4.7.

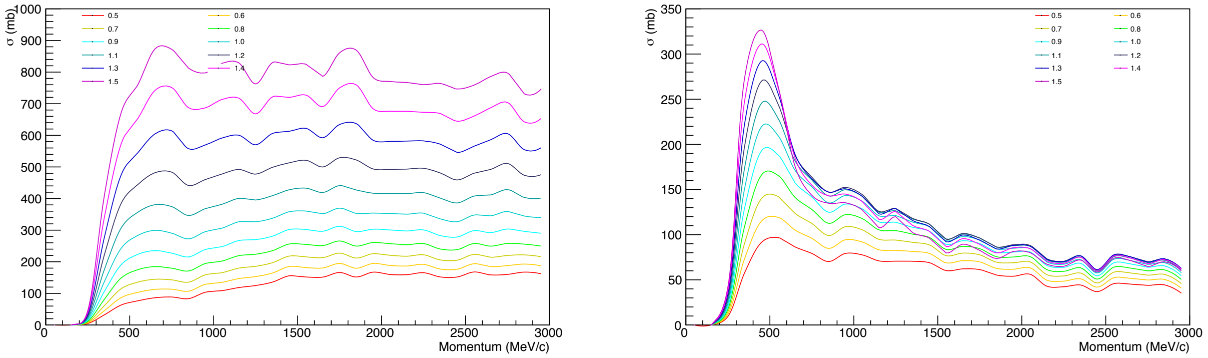

(a) Total

(b) Quasi-elastic

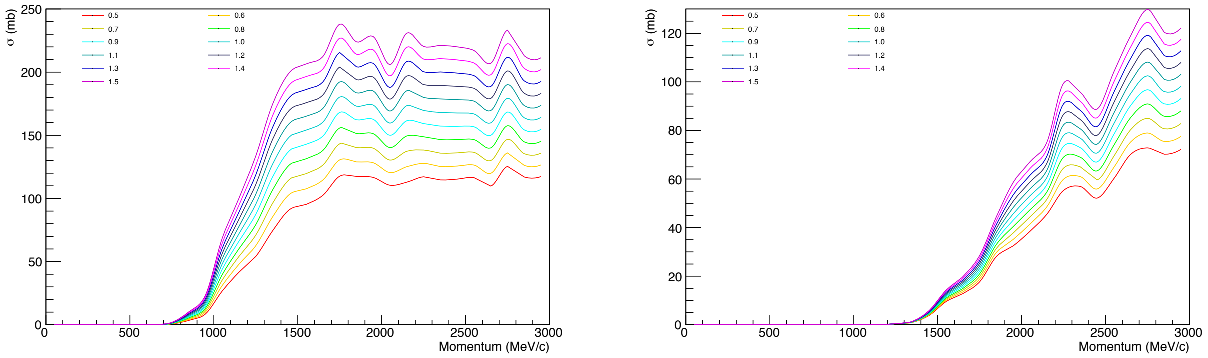

(c) Single π production

(d) Double π production

Figure 4.7: p-C scattering cross-section predictions for each of the interaction channels. The different colour lines show different scaling parameters used to generate the MCs.

4.5 FSI Parameter Tuning using External Scattering Data

The scaling parameters can be tuned using external scattering data. Proton beam scattering data are used for tuning FSI parameters as they isolate the hadronic processes involved in FSI. Data compiled from various experiments are in three categories: total cross-section, reactive cross-section and elastic cross-section measurements. There are no pion production measurements available for tuning. When considering which NEUT predictions are comparable with these measurements, recall that quasi-elastic channel in NEUT is defined as only 1 proton in the final state, however since the target nucleon always gets knocked out in NEUT simulations, there is no separate "pure" elastic channel. In other words, if there is an interaction, there are always two or more particles in the FS with one being the initial proton and one nucleon that got knocked out. Therefore, the total cross-section prediction should be compared to reactive cross-section measurements. The scaling factor which modifies the total cross-section prediction is referred to as the "total factor". Lists of external data used to compare with NEUT prediction are gathered in table 4.1. More data with other targets are listed in [104]. It was realised that NEUT is not capable of modelling the peak below 500 MeV/c therefore the data points in the low momentum region are excluded for tuning.

A simple 1-D fit is performed using minimum χ^2 method. χ^2 value is defined as:

$$\chi^2 = \frac{1}{n}\sum_{i=1}^{i=n}\Big(\frac{\sigma_{data}(p_i) - \sigma_{simu}(p_i)}{\delta(\sigma_{data}(p_i))}\Big)^2, \tag{4.6}$$

where n is the number of data points, and $\delta(\sigma_{data}(p_i))$ is the error on the data points given in references. MC reweighting scheme is employed to calculate χ^2 values for different values of total factor. Data/prediction discrepancy is seen in the low momentum region, as the FSI parameters do not allow NEUT to model this region (or Pauli blocking is too strong), no tuning can result to a good fit to all the data, therefore reactive cross-section data points below 500 MeV/c are excluded for fitting. The best-fit value for the total factor comes to 0.537 ± 0.029. The prediction using best-fit value with data points is shown in Figure 4.8.

Table 4.1: Lists of p-C reactive cross-section scattering data used for comparison with NEUT prediction. Only the bottom half of the table is used for tuning (see paragraph).

Reference	momentum (MeV/c)
Wilkins, Bruce D. [105]	137-138
Dicello, J. F. [106]	137-192
Motoji Q. Makino [107]	175-231
Slaus, I. [108]	205-253
McGill, W. F. [109]	231-303
Renberg, P. U. [110]	698-1158
Millburn, G. P. [111]	618-816
R. Goloskie [112]	389-517
Chen, Francis F. [113]	1534
dubna-exp db data [114]	180-2238

4.6 Comparing generator predictions

In this section the NEUT cascade model using best-fit results from previous section and the selection of external data used for its tuning are compared with various neutrino generators. The following generators are used for comparison:

- GENIE hA model is an effective cascade model which uses an interpolation of external data of cross-section for each possible interaction channel as a function of energy (up to 1.2 GeV) to determine the final state.
- The Bertini/Binary cascade models of Geant 4.9.4 uses GHEISHA and Barashenkov parameterisation driven models [115] as input cross-sections to the cascade model.
- FLUKA and NuWro also use semi-classical cascade model based on the Oset et al. model but are tuned by different cross-section data.

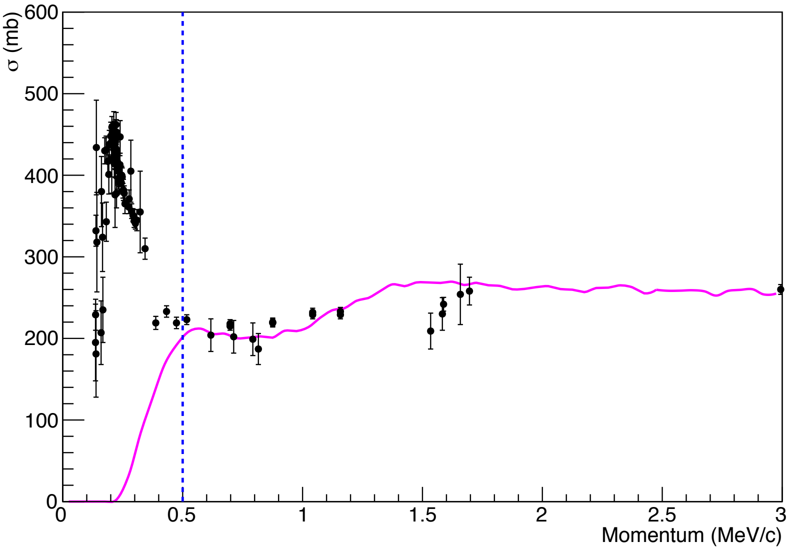

Figure 4.8: Proton-Carbon scattering cross-section predictions using best-fit value for total factor. Data points are described in table 4.1. It was realised that NEUT is not capable of modelling the peak below 500 MeV/c therefore the data points in that region are excluded for tuning.

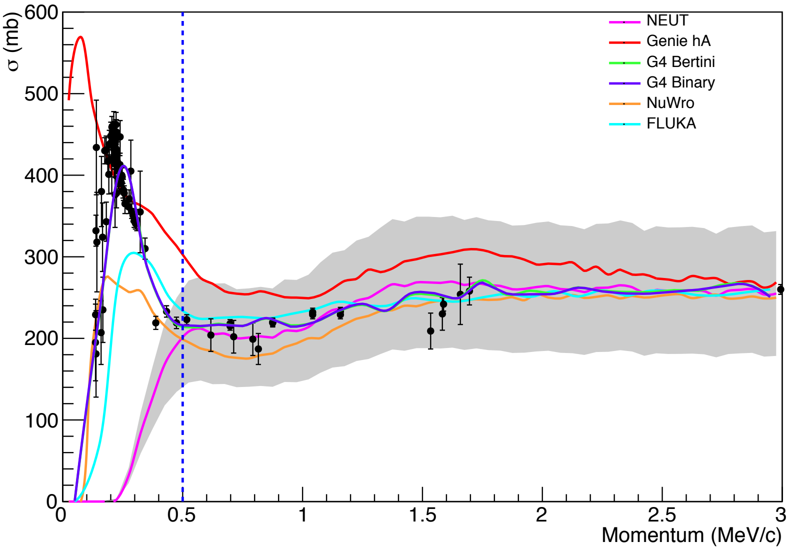

Figure 4.9: Proton-Carbon scattering cross-section predictions using best-fit value for total factor overlayed with other generator predictions. An uncertainty band of 30% is added to the NEUT prediction. Data points are described in table 4.1. Data points below 500 MeV/c are not used for fitting.

Since the error from the 1D fit seems too small to cover the data points and there are known limitations to the model, an uncertainty of 30% is used to the NEUT prediction to cover all generator predictions and the data points including errors above 500 MeV/c. While there are good agreements in this region, the predictions are vastly different at low momentum region. NEUT fails to model the peak at low momentum region indicates that it would need major modifications to the model. It is also interesting to see that both the Geant4 models agree very well with the data points. It would be better to adapt the Geant4 models into NEUT, or to re-define the model parameters such that more data can be used to tune the parameters. In principle, heavier target data and differential cross-section data are also available for tuning, however the FSI model in NEUT is not complicated enough to model the angle of outgoing nucleon. After all, this is the first attempt of tuning proton FSI parameters, and this would require much effort to be used in future analyses.

Chapter 5

Neutrino Event Selections at near and far detectors

This chapter describes the measurements at ND280 and SK which are used for this analysis. The total accumulated data used in this oscillation analysis corresponds to 2.23×10^{21} POT, 1.47×10^{21} POT in FHC and 0.76×10^{21} POT in RHC (equivalent to T2K Runs 1-8 in FHC and Runs 5-7 in RHC).

5.1 Event Samples as inputs to Oscillation Analysis

Figure 5.1 shows the general analysis strategy to extract oscillation parameters. Firstly, a near detector fit is done using the ND280 data as inputs to constrain neutrino flux uncertainties and cross-section uncertainties. Then the reduced uncertainties are used together with SK data for a far detector fit. Prior to far detector fit using actual data, the fitting framework used for this analysis has been thoroughly validated through comparing results with two other oscillation analysis groups. The following sections describes the data that are used for each of the fit.

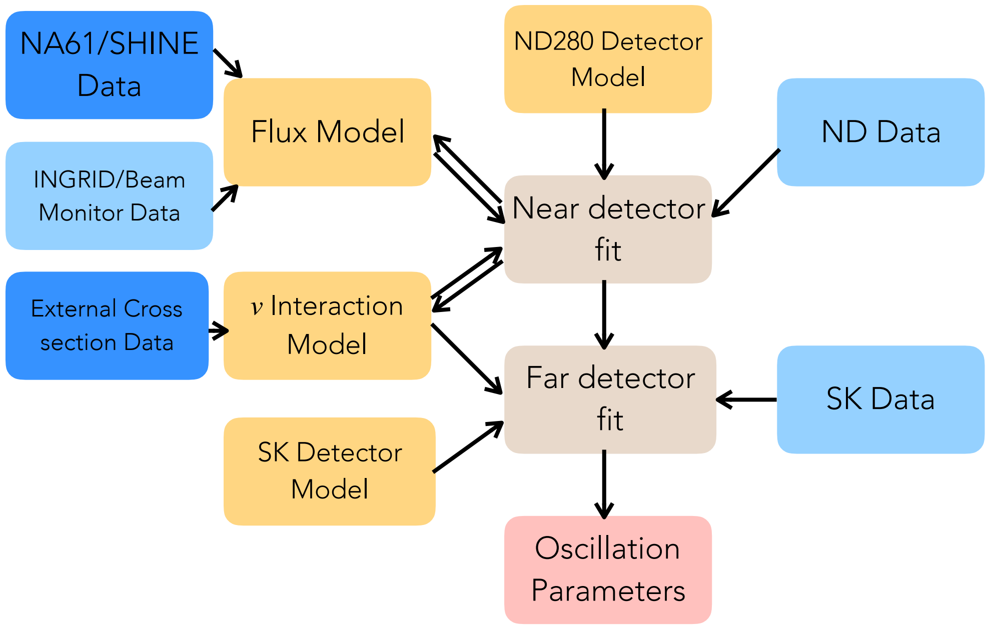

Figure 5.1: Basic work flow to extract oscillation parameters.

5.2 Event Selections at ND280

Event selections at ND280 in both the neutrino mode and the antineutrino mode data with interactions in FGD1 and FGD2 are used to constrain neutrino flux uncertainties and cross-section uncertainties at SK. The data used are described in detail in [7, 116, 117, 118, 119, 120]. They are used to predict the event rate and spectra of selected samples at the far detector.

In order to constrain the uncertainties of flux and cross-section, the ND280 data samples are binned in muon momentum and cosine of muon angle and all 14 samples are fitted simultaneously to obtain best fit values for the cross section parameters, which are shown in table 5.1, and the flux parameters, which are just the normalisation factors for the 4 neutrino species at SK in bins of neutrino energy. This is referred to as the Beam And Nd280 Flux Fit (BANFF) fit [121].

Table 5.1 shows the number of POT, the event rates in each sample for the data, pre-fit and post-fit, with the post-fit rates taken from the BANFF result. The 13av2 flux tuning weights, the ND280 detector systematic prior weights and the cross-section weights are all applied to

Sample	Data	Postfit	Prefit
FGD1 ν_μ CC0π (ν mode)	17136	17122.22	16723.69
FGD1 ν_μ CC1π (ν mode)	3954	4061.65	4381.48
FGD1 ν_μ CC Other (ν mode)	4149	4095.58	3943.95
FGD1 $\bar{\nu}_\mu$ CC 1-Track ($\bar{\nu}$ mode)	3527	3503.79	3587.65
FGD1 $\bar{\nu}_\mu$ CC N-Tracks ($\bar{\nu}$ mode)	1054	1052.69	1066.91
FGD1 ν_μ CC 1-Track ($\bar{\nu}$ mode)	1363	1353.44	1272.17
FGD1 ν_μ CC N-Tracks ($\bar{\nu}$ mode)	1370	1354.02	1357.45
FGD2 ν_μ CC0π (ν mode)	17443	17494.56	16959.19
FGD2 ν_μ CC1π (ν mode)	3366	3416.28	3564.23
FGD2 ν_μ CC Other (ν mode)	4075	3915.36	3570.95
FGD2 $\bar{\nu}_\mu$ CC 1-Track ($\bar{\nu}$ mode)	3732	3685.46	3618.27
FGD2 $\bar{\nu}_\mu$ CC N-Tracks ($\bar{\nu}$ mode)	1026	1097.38	1077.24
FGD2 ν_μ CC 1-Track ($\bar{\nu}$ mode)	1320	1330.49	1262.63
FGD2 ν_μ CC N-Tracks ($\bar{\nu}$ mode)	1253	1263.12	1246.71
Total	64768	64746.02	63632.53
FHC POT	58.00×10^{19}	1219.65×10^{19}	
RHC POT	38.58×10^{19}	558.62×10^{19}	

Table 5.1: Comparison of the event rates for data, pre-fit MC and post-fit MC broken by samples.

the MC, which is then weighted by the ratio of data POT over MC POT for each run period.

The ND280 measurement constrains the SK flux parameters due to correlation between ND280 and SK flux derived from the neutrino beam simulation. It also constrains the cross-section parameters which are strongly correlated between ND280 and SK. Table 5.2 show the best-fit, prefit and postfit errors for the cross-section parameters. Uncertainties on these parameters are reduced by the ND280 constraint. The ND fit reproduced the data well with a p-value of 0.47. When the ND280 constraint is applied, strong anti-correlations between the SK flux parameters and the cross section parameters appear as shown in figure 5.2. This is because the error constraint is actually done on the event rate, which is the product of flux and cross section, as shown in equation 4.1. Further details about the binning of the SK flux parameters and parameterisation of the cross-section model are described in next chapter.

Table 5.2: Summary of the cross-section parameters and their 1σ fractional errors pre/post BANFF fit.

Parameter	Best-fit	1σ prefit fractional error	1σ postfit fractional error
M_A^{QE}	0.903	0.025	0.066
p_F	0.916	0.058	0.067
2p2h norm. ν	1.426	1	0.195
2p2h norm. $\overline{\nu}$	0.522	1	0.231
2p2h norm. C to O	0.940	0.2	0.167
2p2h shape O	0.997	3	0.347
C_A^{RES}	0.977	0.149	0.063
M_A^{RES}	0.822	0.158	0.047
BG_A^{RES}	0.979	0.308	0.197
CC other shape	0.519	0.028	0.028
CC coherent	0.906	0.028	0.028
NC coherent	0.939	0.4	0.197
BeRPA A	0.663	0.118	0.057
BeRPA B	1.647	0.21	0.12
BeRPA D	0.988	0.17	0.13
BeRPA E	0.876	0.35	0.35

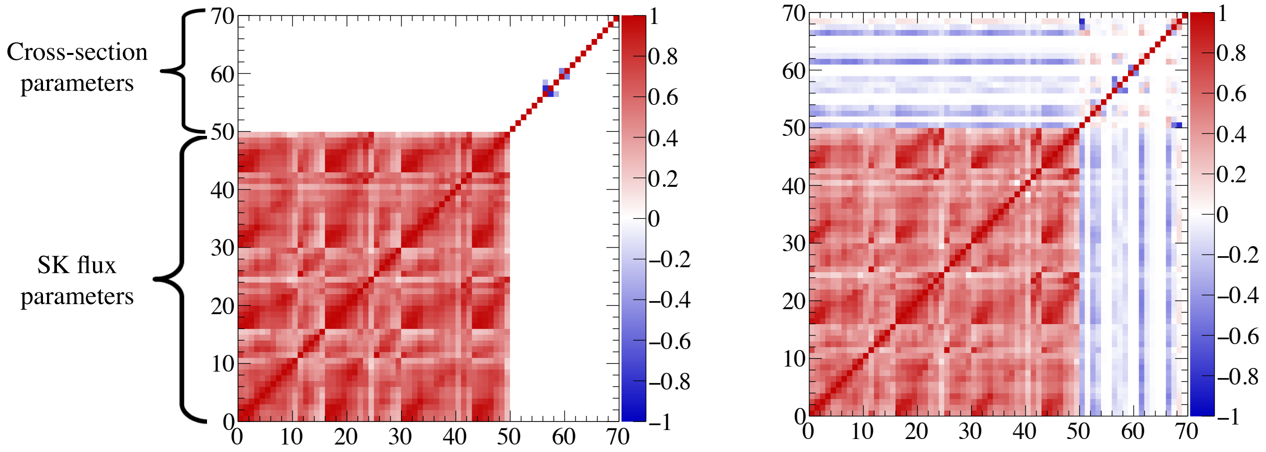

(a) without ND280 constraint (b) with ND280 constraint

Figure 5.2: The parameter correlations without (left) and with (right) the ND280 constraint.

5.3 Event Selections at SK

Since the 2016 results were released [7], some studies were performed to optimise the event selection at SK using fiTQun reconstruction [122]. fiTQun is an event reconstruction algorithm which uses maximum likelihood method and performs reconstruction under various particle hypotheses like electron, muon, and π^0 , hence providing enhanced particle identification capability and allows better π^0 and π^+ background rejection. In the following subsections I will outline the selection cuts to select each of the samples.

5.3.1 1Rμ and 1Re samples

A series of selection cuts is applied to SK MC and data to obtain the 1Re and 1Rμ samples. The selections are optimised to select CCQE interactions since it allows the energy of the incoming neutrino to be reconstructed using lepton momentum and angle as show in equation 4.4, it also provides a clear way to distinguish between ν_e and ν_μ interactions (as described in section 3.11).

Since the 2016 analysis, the fiducial volume (FV) has been re-optimised to increase the statistics which is described by combined variables *wall* and *towall*; they are defined as the shortest distance from vertex to detector wall, and distance to detector wall along the reconstructed particle track respectively. The two variables are optimised individually for each sample. The fiTQun ν_μ event selection criteria are as follow:

1. Fully-contained in SK fiducial volume (FCFV): classified as fully contained events, *wall* $>$ 50cm, *towall* $>$ 250cm
2. Number of rings found by the fiTQun ring counting algorithm is one
3. The ring is identified as muon-like by the PID algorithm: $\ln\,(L_e/L_\mu) < 0.2 \times p_e$, where L_e is the fiTQun 1Re-like hypothesis likelihood, L_μ is the fiTQun 1Rμ-like likelihood, and p_e is the reconstructed electron momentum of 1Re-like hypothesis
4. Reconstructed muon momentum (p_μ) of the 1Rμ-like hypothesis is larger than 200 MeV

5. Number of sub-events is 1 or 2 (i.e. number of decay electrons is 0 or 1)

6. fiTQun π^+ rejection cut: ln $(L_{\pi^+}/L_\mu) < 0.15 \times p_\mu$, where ln L_{π^+} is the log likelihood of fiTQun 1Rπ^+ hypothesis

Same event selections are used between the forward and reverse horn current samples. The π^+ rejection cut is optimised by evaluating $\sin^2\theta_{23}$ measurement precision. Two-dimensional distributions of the fiTQun π^+ cut variables p_μ and $\ln(L_{\pi^+}/L_\mu)$ after cut 5 is shown in Figure 5.3. Figure 5.4 shows the distribution of reconstructed neutrino energies for the final ν_μ and $\overline{\nu}_\mu$ candidates. We see a clear oscillation dip at the peak energy of 600 MeV, and small contributions from irreducible background of wrong sign ν_μ , CC non-QE and NC events.

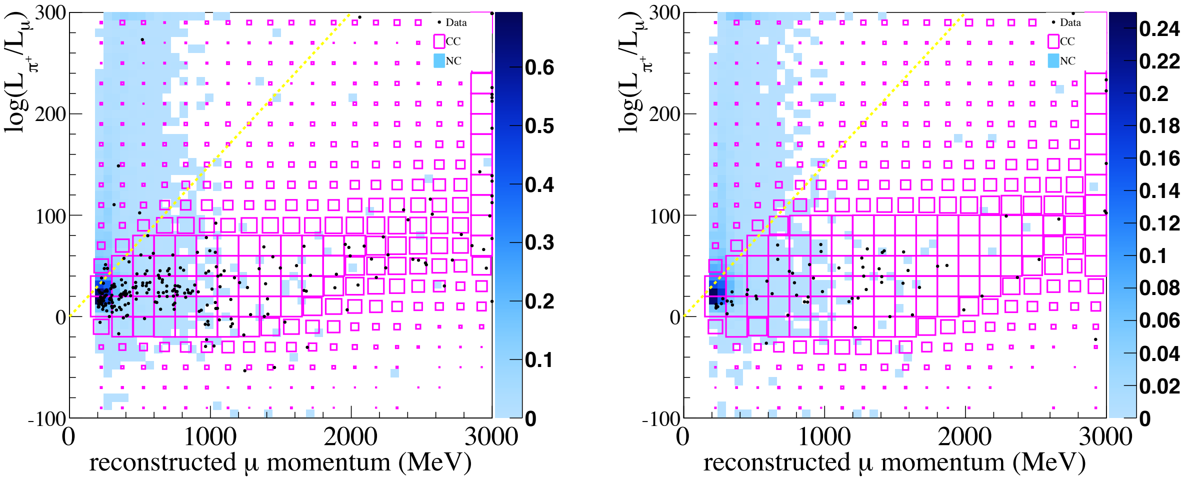

(a) ν_μ (b) $\overline{\nu}_\mu$

Figure 5.3: Two-dimensional distributions of the fiTQun π^+ cut variables p_μ and ln (L_{π^+}/L_μ) for ν_μ candidates in Runs 1-8 neutrino mode data (left) and $\overline{\nu}_\mu$ candidates in Runs 5-7 antineutrino mode data (right). The π^+ cut is shown in dotted yellow line, with events below the line selected as event candidates. MC distributions are made using oscillation parameters shown in Table 6.1 and are normalised to data using POT.

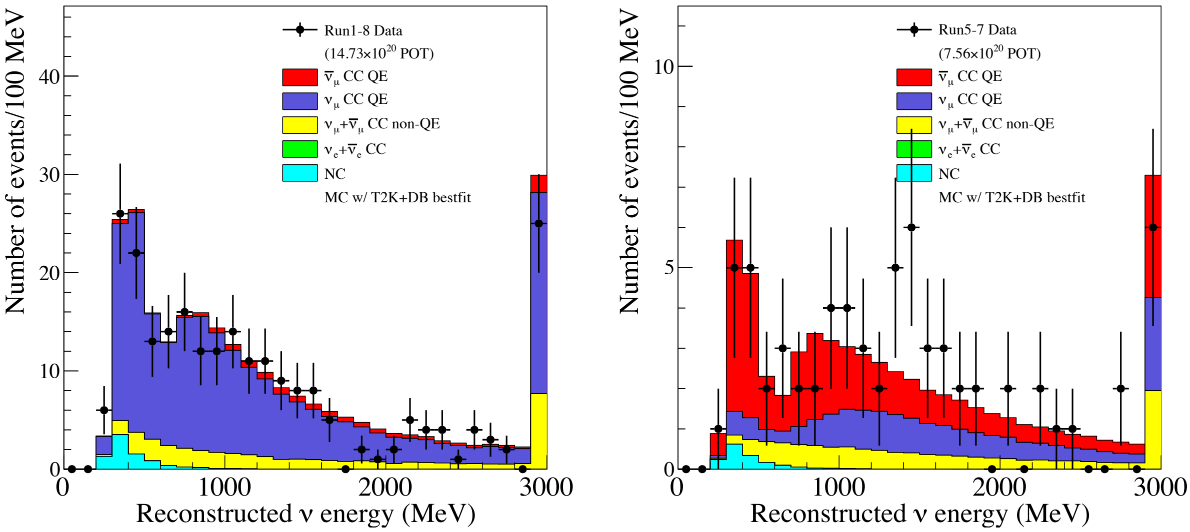

(a) ν_μ (b) $\overline{\nu}_\mu$

Figure 5.4: Reconstructed neutrino energy distribution for the final selected ν_μ candidates for Runs 1-8 neutrino mode data (left) and $\overline{\nu}_\mu$ candidates for Runs 5-7 antineutrino mode data (right). MC distributions are made using oscillation parameters shown in Table 6.1 and are normalised to data using POT.

The fiTQun ν_e event selection criteria are as follow:

1. Fully-contained in SK fiducial volume (FCFV): classified as fully contained events, *wall* $>$ 80 cm, *towall* $>$ 170 cm
2. Number of rings found by the fiTQun ring counting algorithm is one
3. The ring is identified as e-like by the PID algorithm: $\ln\,(L_e/L_\mu) > 0.2 \times p_e$
4. Visible energy (fiTQun single-ring e-like hypothesis reconstructed energy) is greater than 100 MeV
5. Number of sub-events is 1 (number of decay electrons is 0)
6. Reconstructed neutrino energy (E_{rec}) is less than 1250 MeV
7. fiTQun π^0 rejection cut: $\ln\,(L_{\pi^0}/L_e) < 175 - 0.875 \times m_{\pi^0}$, where $\ln L_{\pi^0}$ is the log likelihood of fiTQun 1Rπ^0 hypothesis and m_{π^0} is the fitted π^0 mass from 2 photons

Similar to the 1Rμ samples, the π^0 rejection cut is optimised by evaluating $\delta_{CP} \neq 0$ significance. Two-dimensional distributions of the fiTQun π^0 cut variables m_{π^0} and ln (L_{π^0}/L_e) after cut 6 is applied are shown in Figure 5.5. Figure 5.6 shows the distribution of reconstructed neutrino energies for the final ν_e and $\overline{\nu}_e$ candidates. We see the distributions peak at the peak neutrino energy of 600 MeV, and and contributions from irreducible background of intrinsic ν_e , wrong sign ν_e and NC events.

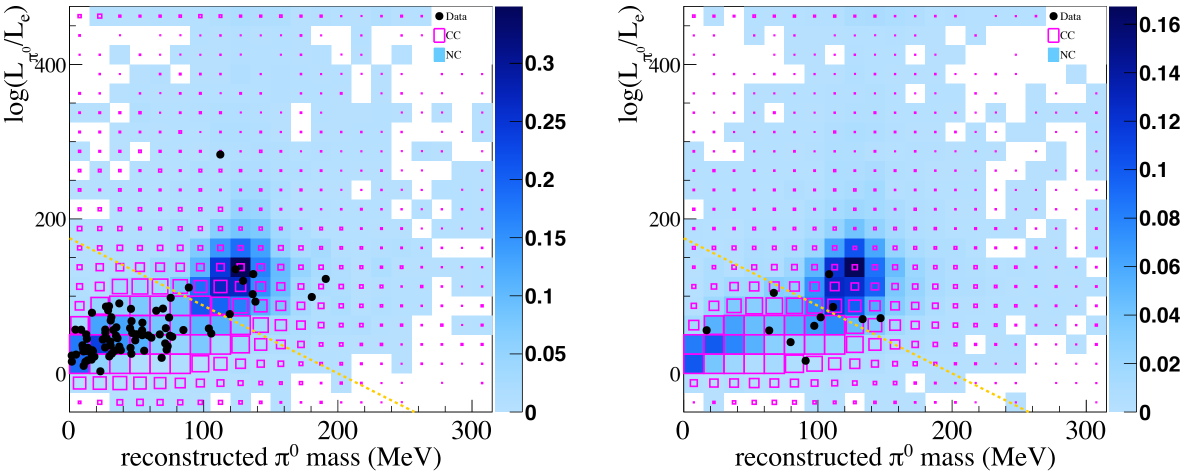

(a) ν_μ (b) $\overline{\nu}_\mu$

Figure 5.5: Two-dimensional distributions of the fiTQun pi^0 cut variables m_{π^0} and ln (L_{π^0}/L_e) for ν_e candidates in Runs 1-8 neutrino mode data (left) and $\overline{\nu}_e$ candidates in Runs 5-7 antineutrino mode data (right). The π^0 cut is shown in dotted yellow line, with events below the line selected as event candidates. MC distributions are made using oscillation parameters shown in Table 6.1 and are normalised to data using POT.

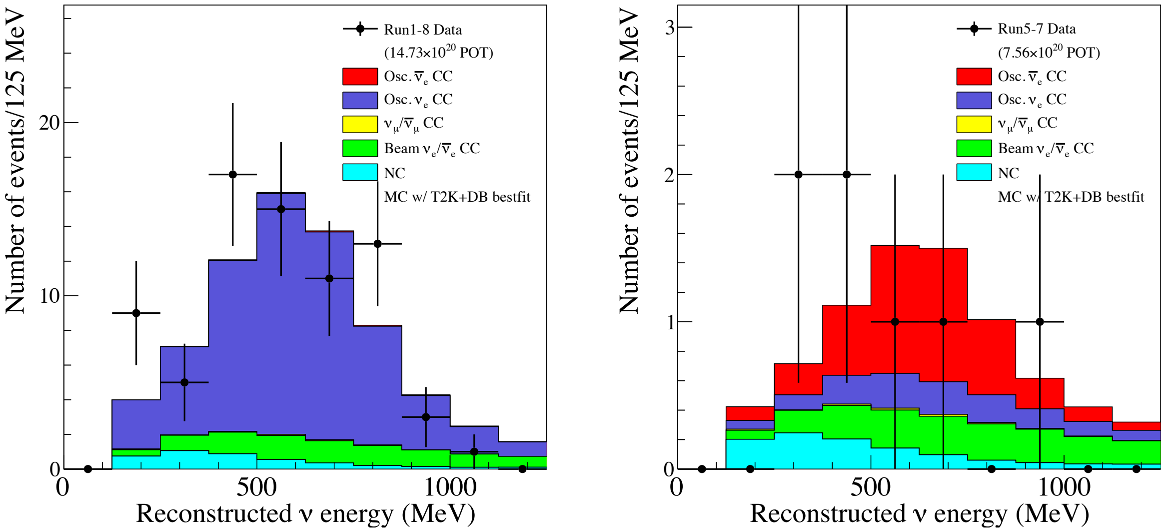

(a) ν_e (b) $\overline{\nu}_e$

Figure 5.6: Reconstructed neutrino energy distribution for the final selected ν_e candidates for Runs 1-8 neutrino mode data (left) and $\overline{\nu}_e$ candidates for Runs 5-7 antineutrino mode data (right). MC distributions are made using oscillation parameters shown in Table 6.1 and are normalised to data using POT.

5.3.2 1Re with 1 decay e

As mentioned in 4.1, T2K has recently added a non-CCQE signal events to increase the statistics available for the ν_e appearance analysis. The events considered are categorised as CC single pion (CC1π) production, which are mainly from RES interactions. These events would need to have good reconstruction efficiencies and good reconstructed energies. It has been realised that additional events can be selected by applying the same selection cuts for 1Re sample, expect having one extra sub-events (number of decay electrons is 1 instead of 0), with the sub-event being delayed electrons originating from pion decays. The events selected are categorised as the 1Re ν_eCC1π^+ sample and they are selected by applying the following cuts:

1. Fully-contained in SK fiducial volume (FCFV): classified as fully contained events, *wall* > 50 cm, *towall* > 270 cm

2. Number of rings found by the ring counting algorithm is one

3. The ring is identified as electron-like by the PID algorithm: $\ln\,(L_e/L_\mu) > 0.2 \times p_e$

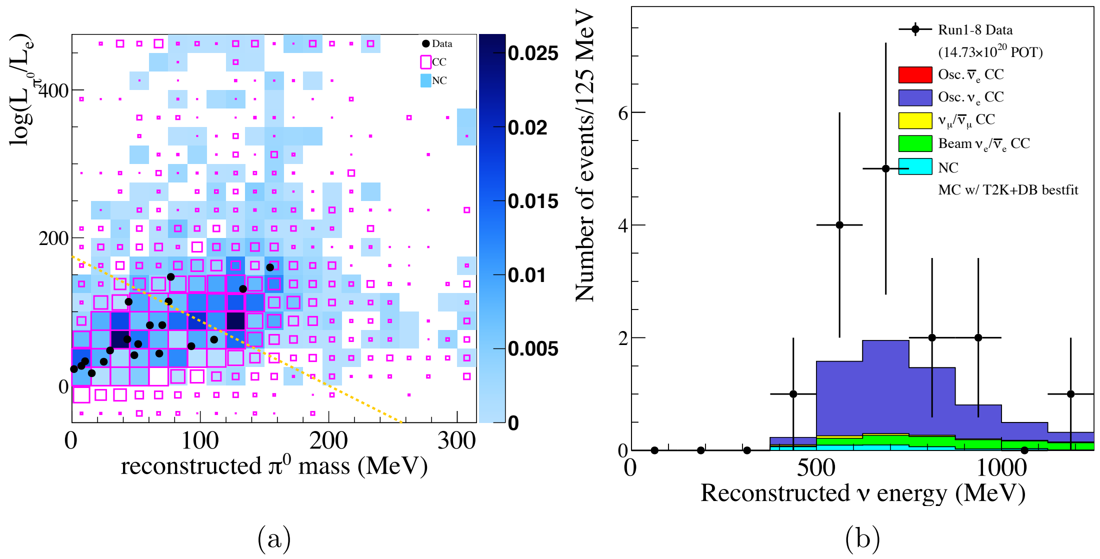

Figure 5.7: Left: Two-dimensional distributions of the fiTQun π^0 cut variables m_{π^0} and ln (L_{π^0}/L_e) for Runs 1-8 neutrino mode data. The yellow line indicates the fiTQun π^0 cut, below which events are chosen as ν_e CC1π^+-like candidates. Right: Reconstructed neutrino energy distribution for the final selected ν_e CC1π^+ candidates. MC distributions are made using oscillation parameters shown in Table 6.1 and are normalised to data using POT.

4. Visible energy (fiTQun single-ring e-like hypothesis reconstructed energy) is greater than 100 MeV
5. Number of sub-events is 2 (number of decay electrons is 1)
6. Reconstructed neutrino energy (E_{rec}) is less than 1250 MeV
7. fiTQun π^0 rejection cut: ln $(L_{\pi^0}/L_e) < 175 - 0.875 \times m_{\pi^0}$

Energies for these events are reconstructed using Δ^{++} mass of 1232 MeV/c^2 (instead of proton mass in case for neutrino interaction in the CCQE picture described in eq. 4.3). Two-dimensional distributions of the fiTQun π^0 cut variables m_{π^0} and ln (L_{π^0}/L_e) after cut 6 is shown in Figure 5.7a. Figure 5.7b shows the distribution of reconstructed neutrino energies for the final ν_e CC1π^+ candidates.

Chapter 6

Oscillation Analysis

6.1 Analysis overview

In this chapter, I will describe the oscillation analysis of the five samples (FHC/RHC 1Rμ, FHC/RHC 1Re and FHC 1Re with 1 decay e) discussed in the previous chapter. This analysis assumes the standard three neutrino PMNS framework, the parameters of interest being θ_{13} , δ_{CP} , θ_{23} , and $|\Delta m^2_{32}|$ (the solar parameters Δm^2_{21} and $\sin^2 2\theta_{12}$ are fixed in this analysis). The behaviour of the fitting framework used for this analysis has been validated by comparing the events rates in each sample, the effect of each systematic error and the sensitivity contours two other independent oscillation analysis groups (VALOR [123] and MaCh3 [124]). All the results are consistent between the groups.

6.2 Analysis strategy

This analysis uses the lepton momentum p_l and scattering angle θ_l with respect to the beam direction to bin the 1Re-like samples as they are both reconstructable quantities at SK. The distribution of the momentum p_l and scattering angle θ_l of reconstructed electrons (positrons) is different for the signal and background categories, as shown in Fig. 6.1 (6.2). The $p - \theta$

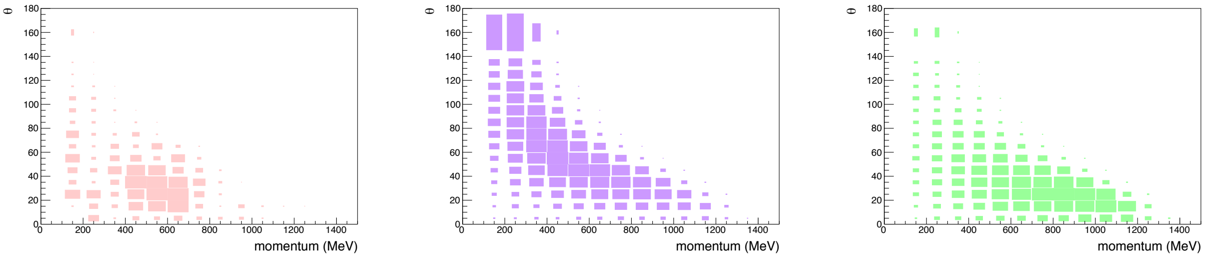

(a) CCν_μ + CC$\bar{\nu}_\mu$ (b) CCν_e (c) CC$\bar{\nu}_e$

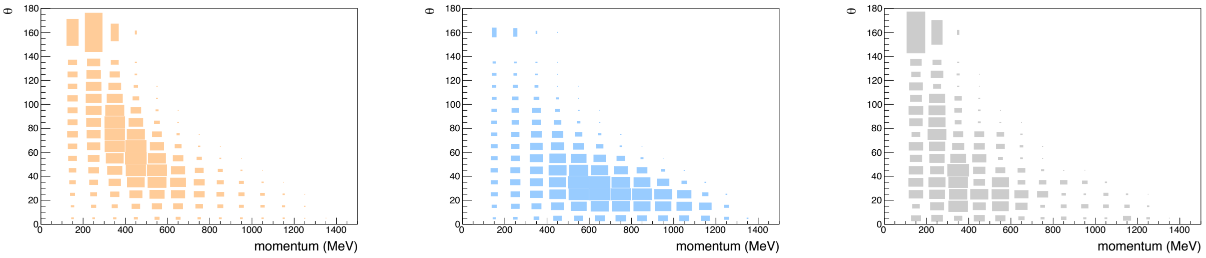

(d) Osc. CCν_e (e) Osc. CC$\bar{\nu}_e$ (f) NC

Figure 6.1: Distributions of the lepton momentum and angle for the FHC 1Re-like samples for the signal (6.1d) and the five background categories. These figures assumes the oscillation parameters Set A listed in Table 6.1.

distribution thus provides additional power to distinguish between signal and background events (including ν vs. $\bar{\nu}$). 1Rμ-like samples are binned using reconstructed energy.

This analysis aims to constrain four oscillation parameters and in particular δ_{CP} . We consider a combined likelihood based on multiple data samples and marginalise over nuisance parameters to produce one- and two-dimensional confidence limits and credible intervals. The complete likelihood would have far too many parameters to scan over the whole space so the marginalisation process is built into the likelihood calculation. Marginalisation is a well-defined process in Bayesian statistics, here the nuisance parameters are assumed to have Gaussian priors and can integrate over to calculate the likelihood (more details on Section 6.3.2). This is achieved by summing over a set of pre-calculated parameter throws, including the appropriate correlations, at each point in a low (i.e. manageable) dimensional space. This method is preferred over profiling method because profiling involves maximising (or minimising) the likelihood with respect to all other nuisance parameters, which involves using minimisation package that takes significantly more computational time given the number of parameters considered in this analysis, using marginalisation also avoids problems with convergence that may arise.

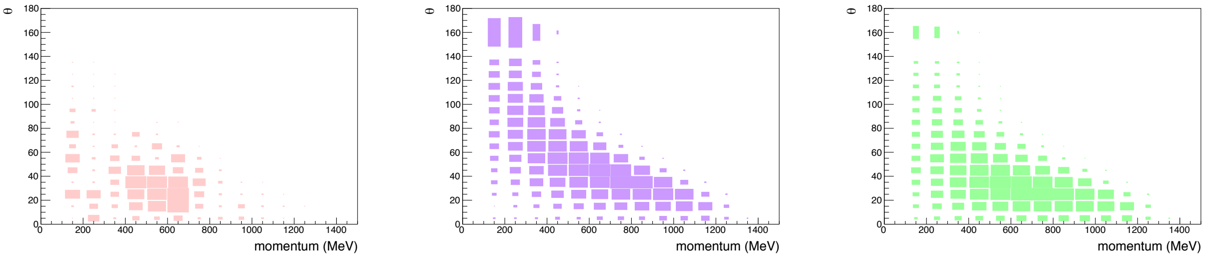

(a) $\mathrm{CC}\nu_\mu + \mathrm{CC}\bar{\nu}_\mu$ (b) $\mathrm{CC}\nu_e$ (c) $\mathrm{CC}\bar{\nu}_e$

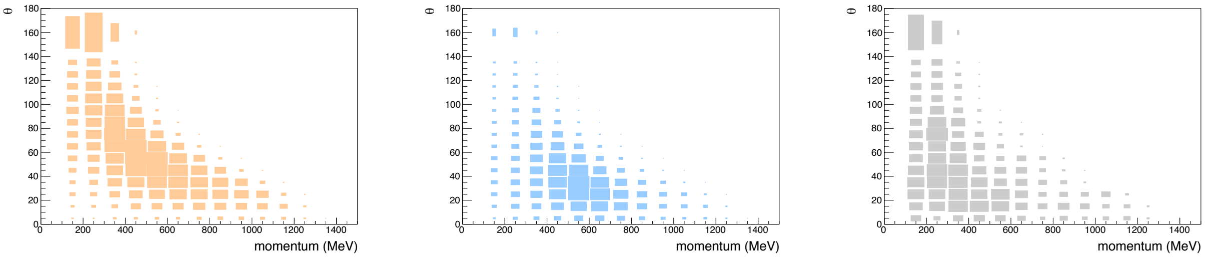

(d) Osc. $\mathrm{CC}\nu_e$ (e) Osc. $\mathrm{CC}\bar{\nu}_e$ (f) NC

Figure 6.2: Distributions of the lepton momentum and angle for the RHC 1Re-like samples for the signal (6.2e) and the five background categories. This figures assumes the oscillation parameters Set A listed in Table 6.1.

With the addition of RHC data, T2K has developed greater sensitivity to δ_{CP} by itself, however the statistics are still low so results have also been produced including in the fit an additional Gaussian constraint on $\sin^2 2\theta_{13}$ based on the combined results of reactor experiments ($\sin^2 2\theta_{13} = 0.0857 \pm 0.0046$) [10] which serves to break the degeneracy between $\sin^2 2\theta_{13}$ and δ_{CP} . This constraint is either included in the prior used to generate the throws for marginalisation described above, if $\sin^2 2\theta_{13}$ is being marginalised, or it is added explicitly as an extra factor in the likelihood.

6.2.1 Definition of likelihood

The analysis is based on a maximum likelihood method. The likelihood is defined as:

$$\mathcal{L}(N_e^{obs.}, N_\mu^{obs.}, \boldsymbol{x}_e, \boldsymbol{x}_\mu, \boldsymbol{o}, f) = \mathcal{L}_e(N_e^{obs.}, \boldsymbol{x}_e, \boldsymbol{o}, f) \times \mathcal{L}_\mu(N_\mu^{obs.}, \boldsymbol{x}_\mu, \boldsymbol{o}, f) \times \mathcal{L}_{\mathrm{syst.}}(f), \tag{6.1}$$

where e and μ represents each of the e-like or μ-like sample considered in this analysis. The variables have the following meaning:

- $N^{obs.}_{e/\mu}$ is the number of candidate e-like or μ-like events observed in SK
- $\boldsymbol{x}_{e/\mu}$ represents measurement variables (momentum p and angle θ for e-like events, and reconstructed energy E_{rec} for μ-like events)
- $\boldsymbol{o}$ represents the oscillation parameters we are trying to measure
- $\mathcal{L}_{\text{syst.}}(f)$ is likelihood term for systematic uncertainties. There is a total of 119 systematic parameters, and their prior uncertainties is taken to be multivariate normal, defined by a covariance matrix and mean values of the parameters.

$\mathcal{L}_{e/\mu}$, the likelihood ratio, can be written as

$$\mathcal{L}_{e/\mu} = \frac{\prod_{i}^{N} P(N^{obs.}, N^{exp.}(\boldsymbol{o}, f))}{\prod_{i}^{N} P(N^{obs.}, N^{obs.})} \tag{6.2}$$

where i runs through each E_{rec} or p—θ bin depending on the sample considered. $\prod_{i}^{N} P(N^{obs.}, N^{exp.}(\boldsymbol{o}, f))$ is the Poisson probability of observing $N^{obs.}$ events with a mean of expected number of events at SK $N^{exp.}(\boldsymbol{o}, f)$. Similarly $\prod_{i}^{N} P(N^{obs.}, N^{obs.})$ is the Poisson probability of observing $N^{obs.}$ when $N^{obs.}$ is expected.

Minimising $-2\times\ln\,\mathcal{L}_{e/\mu}$ is the same as maximising $\mathcal{L}_{e/\mu}$. Therefore the likelihood ratio can be written as the log-likelihood which is calculated by:

$$-2 \times \ln\,\mathcal{L}_{e/\mu} = 2 \times \sum_{i}((N_i^{exp.} - N_i^{obs.}) + N_i^{obs.} \cdot \ln(N_i^{obs.}/N_i^{exp.})), \tag{6.3}$$

The total log-likelihood is then given by the sum of $2\times\ln\,\mathcal{L}_{e/\mu}$ for all 5 samples considered:

$$-2 \times \ln\,\mathcal{L} = \sum_{samples} -2 \times \ln\,\mathcal{L}_{e/\mu} \tag{6.4}$$

6.2.2 Oscillation parameters

This analysis uses marginalisation for all oscillation parameters including the mass hierarchy (described in later sections) with the exception of the solar oscillation parameters which are fixed (their uncertainties have a negligible impact on the results). Two sets of reference oscillation parameters are defined which are derived from the previous neutrino mode joint fit to evaluate a reference expected number of events. The event rates are used as a cross check between the three oscillation analysis groups. Set A represents parameter values close to the T2K best fit for Run 1-7, whilst Set B modifies these parameters such that CP is conserved and $\sin^2\theta_{23}$ is changed to the non-maximal mixing value preferred by NOvA, so that the effect of those have on the expected sensitivities can be seen. Both parameter sets have been used for consistency checks between different oscillation analysis groups and to evaluate the sensitivity.

Table 6.1: Reference values of the neutrino oscillation parameters for Set A and B and earth matter density. The oscillation parameters are the best fit values from the neutrino mode joint fit results from previous analysis with $\sin^2 2\theta_{13}$ shifted to the new reactor best-fit point.

Parameters	Set A	Set B
Δm^2_{21}	7.53×10^{-5} eV^2	7.53×10^{-5} eV^2
Δm^2_{32}	2.509×10^{-3} eV^2	2.509×10^{-3} eV^2
$\sin^2\theta_{23}$	0.528	0.45
$\sin^2\theta_{12}$ ($\sin^2 2\theta_{12}$)	0.304 (0.846)	0.304 (0.846)
$\sin^2\theta_{13}$ ($\sin^2 2\theta_{13}$)	0.0219 (0.0857)	0.0219 (0.0857)
δ_{CP}	-1.601	0
Earth matter density	2.6 g/cm^3	2.6 g/cm^3
Baseline length	295 km	295 km
Mass hierarchy	Normal	Normal

6.2.3 Neutrino flavours considered in this analysis

Contributions from six types of neutrino propagation are considered in the analysis: $\nu_\mu \rightarrow \nu_\mu$, $\overline{\nu}_\mu \rightarrow \overline{\nu}_\mu$, $\nu_e \rightarrow \nu_e$, $\overline{\nu}_e \rightarrow \overline{\nu}_e$, $\nu_\mu \rightarrow \nu_e$, $\overline{\nu}_\mu \rightarrow \overline{\nu}_e$. Since ν_τ and $\overline{\nu}_\tau$ cannot undergo CC interactions in the energy range spanned by the T2K flux such events can be neglected. $\nu_e \rightarrow \nu_\mu$ ($\overline{\nu}_e \rightarrow \overline{\nu}_\mu$) transitions are negligible. All three flavours undergo NC interactions at the same rate so the unoscillated flux is used to simulate NC events.

6.2.4 Categories of neutrino interaction modes

A recent implementation of the CC multi-nucleon mode (2p2h) in NEUT has been considered in this analysis. We group the NEUT neutrino interaction modes into a set of nine categories: charged-current quasi-elastic interactions (CCQE), 2p2h, charged-current interactions associated with single-pion resonant production (CC1π), charged-current coherent pion production (CC coherent), other charged-current processes (CC other), neutral current interactions with single pion production (NC1π), NC coherent, NC1γ, and other neutral current interactions (NC other). These categories are the same for all samples.

6.2.5 Initial Xsec reweight

The input SK MC files were generated using the spectral function (SF) model, but it has been decided to use instead the relativistic Fermi gas (RFG) model and relativistic random phase approximation (rel. RPA) because it gave the best agreement with external data (as mentioned in Section 4.2). A reweighting is applied to reflect this change.

There are two further weightings applied. True NC1γ events are increased by 100% (a weight of 2) based on recent data from [125]. CC coherent pion events have been tuned as a function of the pion energy to the Berger-Sehgal model ([126]) following recent MINERνA results (see Table 6.2).

Table 6.2: Weights applied to CC coherent pion events

E_π (GeV)	Weight
0-0.25	0.135
0.25-0.5	0.4
0.5-0.75	0.294
0.75-1.0	1.206

Range	Size of one bin	Number of bins
0 - 1500 MeV/c	100 MeV/c	15
0 - 140 degree	10 degree	14
140 - 180 degree	40 degree	1

Table 6.3: Binning used for lepton momentum and angle PDF for 1Re samples and FHC ν_e CC1π sample.

Range	Size of one bin	Number of bins
0 - 3 GeV	50 MeV	60
3 - 4 GeV	250 MeV	4
4 - 6 GeV	500 MeV	4
6 - 10 GeV	1 GeV	4
10 - 30 GeV	20 GeV	1

Table 6.4: Binning used for the reconstructed energy PDF for 1Rμ sample.

6.2.6 Calculation of the nominal event rates

To begin the analysis in practice, we first generate histograms which contain the probability density in momentum p and scattering angle θ of outgoing electron in case for 1Re samples and ν_e CC1π^+ sample, and reconstructed energy E_{rec} in case for 1Rμ samples for each flavour, interaction category, and true neutrino energy (E^{true}). 15 × 15 bins are used in the $p - \theta$ distribution, 73 bins are used for the reconstructed neutrino energy spectrum distribution and 201 bins are used for the true neutrino energy spectrum distribution. The full binning scheme is shown in tables 6.3, 6.4 and 6.5.

To obtain the expected event rates and the $p - \theta$ distribution, first oscillation probabilities are applied to the input probability density files and stored in templates giving the expected nominal numbers of events for the $p - \theta/E_{rec}$ bins b, the E^{true} bin, interaction mode I and flavour category C:

Range	Size of one bin	Number of bins
0 - 10 GeV	50 MeV	200
10 - 30 GeV	20 GeV	1

Table 6.5: Binning used for the true neutrino energy spectrum.

$$T(E^{true}, C, I, b) = \int db \; dE^{true} \; \Phi(E^{true}, C) \; \sigma(E^{true}, C, I) \; N_t \; \epsilon(E^{true}, C, I) \; P_{osc}(E^{true}, C, I) \tag{6.5}$$

$$= M(E^{true}, C, I, b) \; P_{osc}(E^{true}, C, I) \tag{6.6}$$

where:

- $\Phi(E^{true}, C)$ is the predicted neutrino flux at SK
- $\sigma(E^{true}, C, I)$ is the neutrino-nucleus interaction cross section on water
- N_t is the number of target nuclei
- $\epsilon(E^{true}, C, I)$ is the SK detection and selection efficiency
- $P_{osc}(E^{true}, C, I)$ is the oscillation probability calculated by Prob3++ which is a software package developed by the Super-Kamiokande collaboration [127], It is open source and has been used in many neutrino oscillation analyses.
- $T(C, e, I, b)$ represents the output template.

The event rates for interaction mode I and flavour category C are calculated by applying reweighting factors derived for given values of the systematic parameters to the templates and summing over the $p - \theta/E_{rec}$ and E^{true} bins.

$$N_{\text{pred}}(C, I) = \sum_{E^{true}, b} T(E^{true}, C, I, b) \; R(E^{true}, C, I, b) \tag{6.7}$$

where $R(E^{true}, C, I, b)$ is the reweighting factor which is the product of the BANFF and xsec reweighting factors (see Section 6.2.5).

The $p - \theta/E_{rec}$ spectra are obtained in the same manner.

$$N_{\text{pred}}(b) = \sum_{E^{true}, C, I} T(E^{true}, C, I, b) \; R(E^{true} C, I, b) \tag{6.8}$$

6.2.7 Nominal event rates and predicted spectra for the reference values of the oscillation parameters

Using the inputs and the calculation method discussed above, expected event rates with 1.47×10^{21} POT in FHC mode and 7.56×10^{20} POT in RHC mode which corresponds to the data taken up to end of Run 8 are shown in Tables 6.6-6.10. These numbers assumes the oscillation parameters Set A listed in Table 6.1. Corresponding rates for Set B can be found in Appendix A. Table 6.11 shows the expected event rates using oscillation parameters Set A but with δ_{CP} at $-\pi/2$, 0, $\pi/2$ and π.

Table 6.6: Nominal event rate table for 1Rμ, with reweighing factors applied to SK MC, 1.47×10^{21} POT in FHC.

Event Type	$\nu_\mu \to \nu_\mu$	$\nu_e \to \nu_e$	$\bar{\nu}_\mu \to \bar{\nu}_\mu$	$\bar{\nu}_e \to \bar{\nu}_e$	$\nu_\mu \to \nu_e$	$\bar{\nu}_\mu \to \bar{\nu}_e$	Total
CCQE	175.635	0.004	11.028	0.000	0.022	0.000	186.689
CCMEC	35.525	0.002	1.409	0.000	0.026	0.000	36.961
CC 1π	27.696	0.002	2.616	0.000	0.024	0.000	30.338
CC coh.	0.288	0.000	0.092	0.000	0.000	0.000	0.380
CC other	5.467	0.001	0.406	0.000	0.000	0.000	5.874
NC 1π	5.523	0.116	0.197	0.011	-	-	5.847
NC coh.	0.000	0.000	0.000	0.000	-	-	0.000
NC 1γ	0.000	0.000	0.000	0.000	-	-	0.000
NC other	2.056	0.074	0.131	0.009	-	-	2.270
Subtotal	252.191	0.199	15.879	0.021	0.072	0.000	
Total	268.361						

6.2.8 Priors for the oscillation parameters

In this analysis, all but one or two oscillation parameters are marginalised [1] to generate a lower dimensional likelihood. Intervals can then be calculated for the remaining parameters. In order to marginalise the oscillation parameters, this analysis uses uncorrelated one-dimensional prior distributions described in Table 6.12.

---

[1] Solar parameters are fixed.

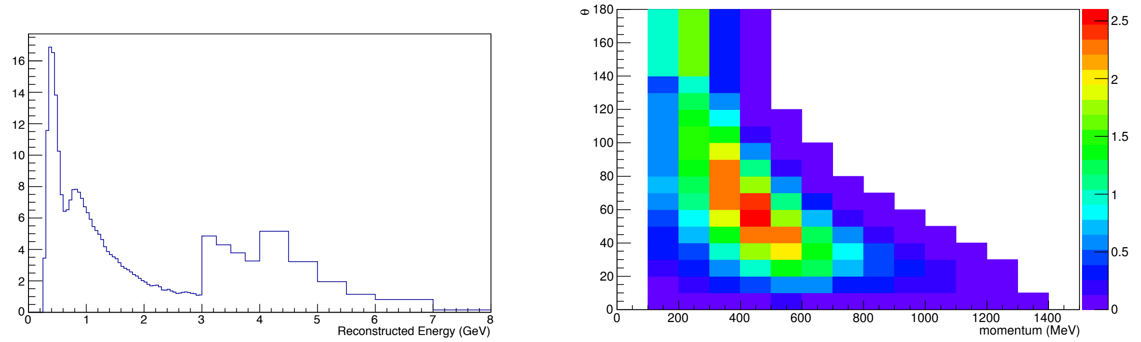

(a) FHC 1Rμ (b) FHC 1Re

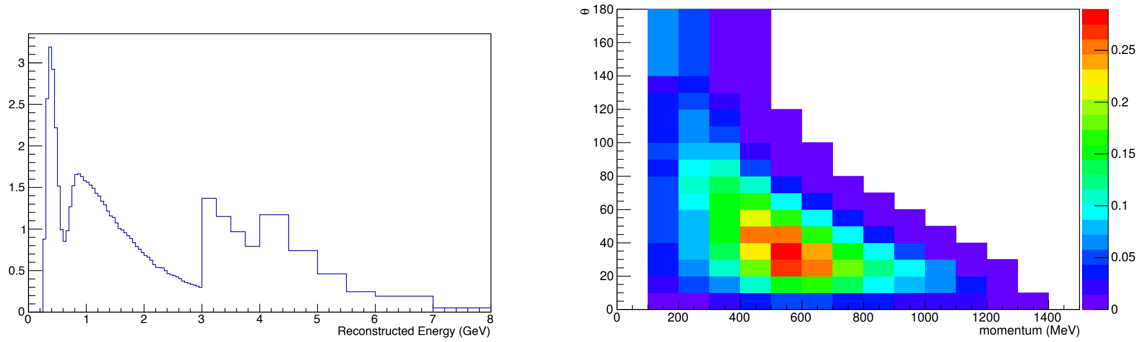

(c) RHC 1Rμ (d) RHC 1Re

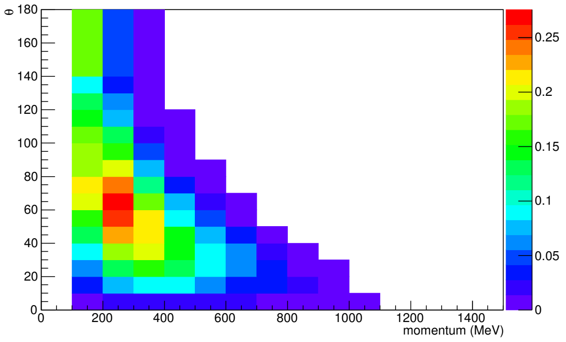

(e) FHC 1R ν_e CC1π^+

Figure 6.3: Predicted spectra for each sample. Distributions for 1Rμ samples are a function of E_{rec} whereas distributions for 1Re samples and ν_e CC1π sample are a function of p and θ. These figures assumes the oscillation parameter set A listed in Table 6.1.

Table 6.7: Nominal event rate table for 1Re, with reweighing factors applied to SK MC, 1.47 × 10^{21} POT in FHC.

Event Type	$\nu_\mu \to \nu_\mu$	$\nu_e \to \nu_e$	$\bar{\nu_\mu} \to \bar{\nu_\mu}$	$\bar{\nu_e} \to \bar{\nu_e}$	$\nu_\mu \to \nu_e$	$\bar{\nu_\mu} \to \bar{\nu_e}$	Total
CCQE	0.161	6.306	0.006	0.255	46.282	0.278	53.288
CCMEC	0.030	1.597	0.001	0.025	8.689	0.023	10.399
CC 1π	0.047	0.932	0.003	0.067	4.495	0.047	5.591
CC coh.	0.000	0.008	0.000	0.004	0.034	0.003	0.050
CC other	0.013	0.128	0.000	0.009	0.089	0.003	0.242
NC 1π	1.870	0.042	0.070	0.004	-	-	1.987
NC coh.	0.528	0.007	0.048	0.003	-	-	0.586
NC 1γ	0.942	0.017	0.050	0.002	-	-	1.011
NC other	0.318	0.017	0.021	0.001	-	-	0.357
Subtotal	3.910	9.054	0.200	0.390	59.589	0.371	
Total	73.514						

Table 6.8: Nominal event rate table for 1Rμ, with reweighing factors applied to SK MC, 7.56 × 10^{20} POT in RHC.

Event Type	$\nu_\mu \to \nu_\mu$	$\nu_e \to \nu_e$	$\bar{\nu_\mu} \to \bar{\nu_\mu}$	$\bar{\nu_e} \to \bar{\nu_e}$	$\nu_\mu \to \nu_e$	$\bar{\nu_\mu} \to \bar{\nu_e}$	Total
CCQE	15.293	0.001	29.874	0.001	0.001	0.001	45.171
CCMEC	4.470	0.000	2.838	0.000	0.000	0.000	7.310
CC 1π	3.955	0.000	4.533	0.000	0.001	0.001	8.490
CC coh.	0.047	0.000	0.176	0.000	0.000	0.000	0.223
CC other	0.942	0.000	0.606	0.000	0.000	0.000	1.548
NC 1π	0.420	0.017	0.522	0.014	-	-	0.973
NC coh.	0.000	0.000	0.002	0.000	-	-	0.002
NC 1γ	0.000	0.000	0.000	0.000	-	-	0.000
NC other	0.316	0.016	0.201	0.008	-	-	0.541
Subtotal	25.443	0.035	38.751	0.023	0.002	0.002	
Total	64.256						

6.2.9 Priors for the systematic parameters

To marginalise the systematic parameters, this analysis uses a MC integration method using throws from the multivariate Gaussian distribution described by the BANFF output (postfit) covariance matrix and central values that constitutes the prior for flux and cross-section parameters. The same is done for the SK detector parameters using SK detector error matrix provided by the T2K-SK group. Effects of these uncertainties are evaluated using the Cholesky method [128]. To generate correctly correlated distributions, the systematic parameters are

Table 6.9: Nominal event rate table for 1Re, with reweighing factors applied to SK MC, 7.56×10^{20} POT in RHC.

Event Type	$\nu_\mu \rightarrow \nu_\mu$	$\nu_e \rightarrow \nu_e$	$\bar{\nu_\mu} \rightarrow \bar{\nu_\mu}$	$\bar{\nu_e} \rightarrow \bar{\nu_e}$	$\nu_\mu \rightarrow \nu_e$	$\bar{\nu_\mu} \rightarrow \bar{\nu_e}$	Total
CCQE	0.013	0.509	0.024	0.848	1.027	2.859	5.280
CCMEC	0.003	0.144	0.001	0.065	0.233	0.191	0.825
CC 1π	0.008	0.101	0.007	0.144	0.143	0.334	0.738
CC coh.	0.000	0.001	0.000	0.011	0.001	0.031	0.044
CC other	0.004	0.021	0.001	0.012	0.010	0.007	0.055
NC 1π	0.163	0.007	0.196	0.005	-	-	0.371
NC coh.	0.048	0.002	0.203	0.003	-	-	0.256
NC 1γ	0.079	0.004	0.175	0.004	-	-	0.262
NC other	0.057	0.002	0.027	0.001	-	-	0.087
Subtotal	0.374	0.792	0.636	1.141	1.415	3.562	
Total	7.920						

Table 6.10: Nominal event rate table for 1R ν_e CC$1\pi^+$, with reweighing factors applied to SK MC, 1.47×10^{21} POT in FHC.

Event Type	$\nu_\mu \rightarrow \nu_\mu$	$\nu_e \rightarrow \nu_e$	$\bar{\nu_\mu} \rightarrow \bar{\nu_\mu}$	$\bar{\nu_e} \rightarrow \bar{\nu_e}$	$\nu_\mu \rightarrow \nu_e$	$\bar{\nu_\mu} \rightarrow \bar{\nu_e}$	Total
CCQE	0.029	0.024	0.001	0.002	0.212	0.003	0.270
CCMEC	0.010	0.022	0.000	0.001	0.160	0.001	0.195
CC 1π	0.076	0.761	0.003	0.004	4.854	0.002	5.699
CC coh.	0.000	0.018	0.000	0.000	0.111	0.000	0.129
CC other	0.038	0.112	0.001	0.003	0.121	0.002	0.276
NC 1π	0.085	0.002	0.005	0.000	-	-	0.092
NC coh.	0.000	0.000	0.000	0.000	-	-	0.000
NC 1γ	0.028	0.000	0.001	0.000	-	-	0.029
NC other	0.206	0.008	0.013	0.001	-	-	0.228
Subtotal	0.472	0.948	0.024	0.011	5.458	0.008	
Total	6.919						

thrown using the following equation,

$$V_i^{sys} = L_{ij}^{sys} R_j, \tag{6.9}$$

where L^{sys} is a lower triangular matrix such that for the covariance matrix M, $M = LL^\dagger$ (Cholesky decomposition) R is a vector which consists of Gaussian distributed random numbers, and V^{sys} is the systematic variations used for marginalising the systematic parameters. It should be noted that some of the systematic parameters (e.g. NIWG parameters) have hard boundaries and if the generated systematic variations exceed the boundaries, the entire set are

Table 6.11: Event rate table using oscillation parameter set A while varying δ_{CP} , with reweighing factors applied to SK MC.

	$\delta_{CP} = -\pi/2$	$\delta_{CP} = 0$	$\delta_{CP} = \pi/2$	$\delta_{CP} = \pi$
FHC 1Rμ	267.755	267.409	267.725	268.163
FHC 1Re	73.512	61.463	49.931	61.980
RHC 1Rμ	63.054	62.910	63.055	63.211
RHC 1Re	7.921	9.035	10.044	8.930
FHC 1R ν_e CC1π^+	6.923	6.010	4.868	5.781

Table 6.12: Oscillation parameter prior distributions

Parameter	Prior
$\sin^2 2\theta_{13}$	Uniform(0, 0.4)
w/ PDG reactor constraint	Gaussian($\mu = 0.0857$, $\sigma = 0.0046$)
$\sin^2 \theta_{23}$	Uniform(0.3, 0.7)
δ_{CP}	Uniform(-π, π)
Δm^2_{32}	Uniform(0.002, 0.003)
$\sin^2 2\theta_{12}$	0.846 (Fixed)
$\lvert\Delta m^2_{21}\rvert$	7.53×10^{-5} eV^2 (Fixed)

regenerated until the values are within the boundaries. There is always a boundary to prevent values that would result in a negative event weight.

6.3 Fitting method

This section describes how the model is used to measure the oscillation parameters, producing best fit values and intervals for those parameters.

6.3.1 Global best fit point

We define the best fit point as the set of values of the parameters for which the likelihood $\mathcal{L}(N_e^{obs.}, N_\mu^{obs.}, x_e, x_\mu, \boldsymbol{o}, \boldsymbol{f})$ is maximum. This corresponds to a maximum likelihood estimate for the oscillation and nuisance parameters $\boldsymbol{o}$ and $\boldsymbol{f}$:

$$(o, f)_{Bestfit} = argmax_{o,f}(\mathcal{L}(N_e^{obs.}, N_\mu^{obs.}, x_e, x_\mu, o, f)) \tag{6.10}$$

To obtain this best fit point in practice, the Minuit2 root package is used to minimise $-ln(\mathcal{L})$ with respect to all the parameters. When fitting for θ_{23} using the parameterisation $\sin^2(\theta_{23})$, the likelihood can have a local minimum in each octant, and the minimising algorithm will not be able to compare the two local minima in a single run. The fit is therefore done twice, with a starting point in each octant, and the result ofthose two fits giving the lowest value of the negative log likelihood is kept as best fit point. The fit is performed separately for the normal and inverted hierarchy hypotheses.

6.3.2 Marginal likelihood

The likelihood is defined previously in Section 6.2.1 as:

$$\mathcal{L}(N_e^{obs.}, N_\mu^{obs.}, \boldsymbol{x}_e, \boldsymbol{x}_\mu, \boldsymbol{o}, f) = \mathcal{L}_e(N_e^{obs.}, \boldsymbol{x}_e, \boldsymbol{o}, f) \times \mathcal{L}_\mu(N_\mu^{obs.}, \boldsymbol{x}_\mu, \boldsymbol{o}, f) \times \mathcal{L}_{\text{syst.}}(f), \tag{6.11}$$

and so for a given measurement $\mathcal{L}(N_e^{obs.}, N_\mu^{obs.}, \boldsymbol{x}_e, \boldsymbol{x}_\mu, \boldsymbol{o}, f)$ depends on both the values of the parameters we are trying to measure $\boldsymbol{o}$ and on the values of the nuisance parameters $\boldsymbol{f}$. $\mathcal{L}_{\text{syst}}$

is the systematic term of the likelihood. If the difference of one systematic parameter i from its centre value is called v_i, the likelihood is calculated as:

$$\mathcal{L}_{\text{syst}} = \exp(-0.5 \sum_{i,j} v_i M_{ij} v_j), \tag{6.12}$$

where M_{ij} is the element (i, j) of the inverted covariance matrix. The systematic parameters used in the analysis to model the systematic uncertainties are described in Section 6.4. To be able to extract information about the parameters $\boldsymbol{o}$ and build intervals, we need to construct a likelihood function that depends only on $\boldsymbol{o}$ while taking into account the effect of the systematic uncertainties. We use for this a Bayesian marginalisation method, in which we compute the marginal likelihood by integrating the full likelihood over the nuisance parameters f:

$$\mathcal{L}_{marg}(N_e^{obs.}, N_\mu^{obs.}, \boldsymbol{x}_e, \boldsymbol{x}_\mu, \boldsymbol{o}) = \int \mathcal{L}(N_e^{obs.}, N_\mu^{obs.}, \boldsymbol{x}_e, \boldsymbol{x}_\mu, \boldsymbol{o}, f)\mathrm{d}f. \tag{6.13}$$

The confidence level intervals and Bayesian credible intervals for the parameters of interest $\boldsymbol{o}$ are then constructed based on the distribution of this marginal likelihood $\mathcal{L}_{marg}(N_e^{obs.}, N_\mu^{obs.}, \boldsymbol{x}_e, \boldsymbol{x}_\mu, \boldsymbol{o})$ a function of $\boldsymbol{o}$, which is obtained by evaluating numerically $\mathcal{L}_{marg}(N_e^{obs.}, N_\mu^{obs.}, \boldsymbol{x}_e, \boldsymbol{x}_\mu, \boldsymbol{o})$ for a number of fixed values of $\boldsymbol{o}$ summarised in table 6.13.

Marginalisation of the likelihood over the systematic parameters

We marginalise over the nuisance parameters using a numerical integration technique: we throw the systematic parameters $\boldsymbol{f}$ N times according to their prior distributions $\mathcal{P}_{syst.}(\boldsymbol{f})$, and evaluate:

$$\mathcal{L}_{marg}(N_e^{obs.}, N_\mu^{obs.}, \boldsymbol{x}_e, \boldsymbol{x}_\mu, o) = \frac{1}{N}\sum_{i=1}^{N} \mathcal{L}_e(N_e^{obs.}, \boldsymbol{x}_e, o, f_i) \times \mathcal{L}_\mu(N_\mu^{obs.}, \boldsymbol{x}_\mu, o, f_i), \tag{6.14}$$

where we use, unless otherwise stated, N=10,000 throws of the systematic parameters for this numerical integration. A more detailed description of this method and of its limitations can be found in section 2.1 of [129] and Appendix A.4. It is possible to produce a four-dimensional marginal likelihood (marginalising over all of the systematic parameters but none of the oscillation parameters) to find a four-dimensional best fit point.

Table 6.13: Binning used to evaluate the marginal likelihood for the different oscillation parameters

Parameter	Number of points	First point	Last point
$\sin^2(2\theta_{13})$ (without reactor constraint)	81	0	0.4
$\sin^2(2\theta_{13})$ (with reactor constraint)	81	0.06	0.14
δ_{CP}	51	$-\pi$	$+\pi$
$\lvert\Delta m^2_{32}\rvert$	21	$2 \times 10^{-3}\mathrm{eV}^2$	$3 \times 10^{-3}\mathrm{eV}^2$
$\sin^2(\theta_{23})$	81	0.3	0.7

Marginalisation of the likelihood over some oscillation parameters

We want to fit the T2K data for the four oscillation parameters $\sin^2(\theta_{23})$, $|\Delta m^2_{32}|$, $\sin^2(2\theta_{13})$ and δ_{CP}. However as it is difficult to produce or display intervals in four dimensions, we will in practice look at the results for only one or two parameters at a time. The remaining oscillation parameters become effectively nuisance parameters, which are marginalised over. As we will be using flat prior distributions for those parameters, they will be thrown with uniform probability over the ranges defined in table 6.12 to evaluate the marginal likelihood following equation 6.14. The only exception is for $\sin^2(2\theta_{13})$ when using the results of the reactor experiments, in which case the parameter will be thrown with Gaussian probability ($\overline{x} = 0.0857$, $\sigma = 0.0046$), and the physical constraint $0 \leq \sin^2(2\theta_{13}) \leq 1$.

6.3.3 Confidence level intervals

Frequentist confidence level intervals have been built using the fixed $\Delta\chi^2$ method. The $\Delta\chi^2$ function is defined as:

$$\Delta\chi^2(\boldsymbol{o}) = -2 \times ln\left(\frac{\mathcal{L}_{marg}(\boldsymbol{o})}{\mathcal{L}^{max}_{marg}}\right), \tag{6.15}$$

where $\mathcal{L}_{marg}^{max}$ is the maximum of the marginal likelihood over the range of values of $\boldsymbol{o}$ considered. It has to be noted that it is the maximum of the marginal likelihood $\mathcal{L}_{marg}(N^{obs.}, \boldsymbol{x}, \boldsymbol{o})$ for the one or two parameters we are building intervals for and not of the full likelihood $\mathcal{L}(N^{obs.}, \boldsymbol{x}, \boldsymbol{o}, \boldsymbol{f})$, so that this maximum will not necessarily correspond to the best fit point defined in section 6.3.1, or to the maximum of a marginal likelihood for the four oscillation parameters (as we are marginalising over some of those four parameters to build 1D or 2D intervals).

We then define the interval as the region of the parameter space for which the $\Delta\chi^2$ is inferior to a certain fixed value $\Delta\chi^2_f$, which depends on the target coverage and number of parameters. We will be using the standard values presented in table 6.14, which would give the desired coverage for the intervals assuming the likelihood is approximately Gaussian and takes its significant values far away from physical boundaries. Otherwise, the Feldman-Cousins method [130] can be used to obtain intervals with correct coverage. This is done when fitting the T2K data for one-dimensional δ_{CP} where we are especially concerned about showing the correct coverage, all other confidence level intervals will be made using the fixed values from table 6.14 since it is very computationally intensive especially in two-dimensions.

Table 6.14: Fixed $\Delta\chi^2$ values used to build intervals

Target coverage	1 parameter	2 parameters
68.3%	1	2.3
90%	2.71	4.61

6.3.4 Credible intervals

It is also possible to use the marginalised likelihoods to produce Bayesian credible intervals. This is particularly useful when considering fits close to a boundary where the fixed $\Delta\chi^2$ method may not have the correct coverage. It is also less computationally intensive than calculating critical χ^2 values with the Feldman-Cousins method.

The marginal likelihood is generated in bins, so to improve the accuracy of the interval calculation the first step is to increase the number of bins through interpolation. The bins with the highest likelihood are then selected until the desired fraction of the likelihood lies within the interval. The bin size is kept uniform so that the probability density is proportional to the likelihood.

$$\int_{interval} p(\boldsymbol{o} \mid N_e^{obs.}, N_\mu^{obs.}, \boldsymbol{x}_e, \boldsymbol{x}_\mu) = \alpha\%, \tag{6.16}$$

where the posterior probability for $\boldsymbol{o}$ after measurement $(N_e^{obs.}, N_\mu^{obs.}, \boldsymbol{x}_e, \boldsymbol{x}_\mu)$ is defined by:

$$p(\boldsymbol{o} \mid N_e^{obs.}, N_\mu^{obs.}, \boldsymbol{x}_e, \boldsymbol{x}_\mu) \quad = \quad \frac{\mathcal{L}_{marg}(N_e^{obs.}, N_\mu^{obs.}, \boldsymbol{x}_e, \boldsymbol{x}_\mu, \boldsymbol{o}) \cdot p(\boldsymbol{o})}{\int \mathcal{L}_{marg}(N_e^{obs.}, N_\mu^{obs.}, \boldsymbol{x}_e, \boldsymbol{x}_\mu, \boldsymbol{o}') \cdot p(\boldsymbol{o}')\, d\boldsymbol{o}'}, \tag{6.17}$$

with $p(\boldsymbol{o})$ the prior probability for $\boldsymbol{o}$.

6.4 Systematic parameters

A large number of systematic uncertainties are taken into account when calculating the expected number of events used to evaluate the likelihood. Uncertainties in the beam flux prediction, the neutrino interaction cross-section model and in the event detection efficiency are all considered and are described in this section. Many of the uncertainties are constrained using fits to the near detector data. The parameters which can be constrained by near detector data use the results of the BANFF fit as prior distribution in the analysis.

6.4.1 Implementation in the Analysis

The systematic uncertainties are incorporated into the analysis as systematic error factor f^{Beam}, f^{xsec}, $f^{SK+FSI+PN}$ and $f^{E-scale}$ that scale the predicted number of events. Which events are reweighted by each factor depends on the neutrino flavour and interaction mode. There are 119 parameters in total. Within the likelihood calculation these parameters are treated as a set of Gaussian degrees of freedom (see equation 6.12).

6.4.2 Beam flux parameters

The uncertainties on the neutrino and antineutrino-beam flux predictions are applied as a set of reweighting factors divided up by neutrino flavour and true energy. There are 50 parameters in total described in Table 6.15. The beam parameters are incorporated into the BANFF framework and thus the uncertainty on these parameters is reduced through constraints from the near detector data and the central value is fitted.

6.4.3 Neutrino interaction and cross-section parameters

The interaction and cross-section uncertainties have been updated substantially for the 2017 analyses. This analysis includes new parameterisations of the uncertainties on 2p-2h and RPA

Table 6.15: Binning of f^{Beam} parameters

Event category	Beam ν flavour	Energy Binning (GeV)	# of bins
Oscillated $\bar{\nu}_e$ $\bar{\nu}_\mu$	$\bar{\nu}_\mu$ flavour	0-0.4, 0.4-0.5, 0.5-0.6, 0.6-0.7, 0.7-1.0, 1.0-1.5, 1.5-2.5, 2.5-3.5, 3.5-5.0, 5.0-7.0, 7.0-30.0	11
Oscillated ν_e ν_μ	ν_μ flavour	0-0.7, 0.7-1.0, 1.0-1.5, 1.5-2.5, 2.5-30.0	5
$\bar{\nu}_e$	$\bar{\nu}_e$ flavour	0-0.5, 0.5-0.7, 0.7-0.8, 0.8-1.5, 1.5-2.5, 2.5-4.0, 4.0-30.0	7
ν_e	ν_e flavour	0-2.5, 2.5-30.0	2

modelling, other parameters remain the same as in the previous analysis. There are 20 parameters in total, all of which are included in the near detector fit, though not all receive a significant constraint.

CCQE interactions are described by the relativistic Fermi gas (RFG) model with relativistic random phase approximation (rel. RPA) applied, as mentioned in Section 4.2. The Nieves RPA model [92] has been included as an E_ν and Q^2 dependent effect on the CCQE cross section, but it was found that having one correction term for rel. RPA is not flexible enough. Therefore, Bernstein Random Phase Approximation (BeRPA) function was developed which aimed to have the same Q^2 dependence as the Nieves RPA model, but to provide variable parameters as a function of Q^2 which would roughly cover the theoretical errors. Five parameters named A, B, D, E and U allows variation of various Q^2 region of the RPA function. The nominal BeRPA parameter set and recommended uncertainties are given in Table 6.16. The nominal parameter set was found by fitting Nieves RPA as a function of Q^2 to most closely match the shape. The uncertainties are chosen to approximately cover the 1σ theoretical uncertainties provided Nieves as shown in Figure 6.4. U is fixed because it introduces complicated correlations between parameters and is therefore not included in Table 6.17.

Table 6.16: Nominal values and uncertainties for the five BeRPA parameters. Note that U should not be varied and no uncertainty is provided. All the parameters must be positive and are uncorrelated between them.

Parameter	Nominal value	Uncertainty
A	0.59	20%
B	1.05	20%
D	1.13	15%
E	0.88	40%
U	1.20	fixed

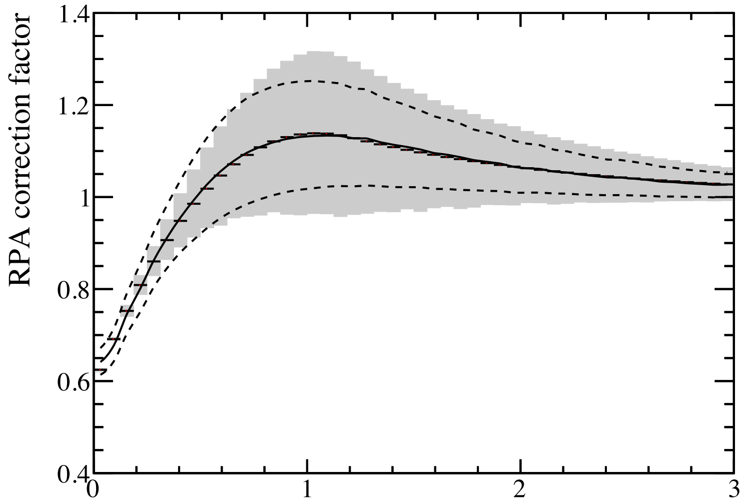

Figure 6.4: The BeRPA best fit value is shown (black data points) compared to the Nieves nominal RPA model as a function of Q^2 (black solid line). The nominal BeRPA 1σ uncertainties are also shown with the theoretical 1σ uncertainties from Nieves for comparison (dashed black lines).

The binding energy E_b (on oxygen) parameter was deprecated since the last analysis because of the phase-space issues meant that the parameter did not properly model variations of the binding energy.

In the previous analysis, there was an overall normalisation parameter for the 2p2h interactions (on oxygen) and an extra normalisation parameter for $\overline{\nu}$ 2p2h interactions such that $\overline{\nu}$ 2p2h interactions receive a weight of $f_{2p2h_O} \times f_{2p2h_{\overline{\nu}}}$. For this analysis, there are separate normalisation parameters for ν and $\overline{\nu}$ 2p2h interactions each of which apply to both carbon and oxygen. An additional normalisation parameter (2p2h norm. C to O) is introduced which has an error of 20% to take into account the difference between carbon and oxygen.

An additional shape uncertainty for 2p2h model is introduced to test the effect of other relevant degrees of freedom in the 2p2h model. This parameter is allowed to vary between -1 to +1 to artificially redistributing the 2p2h cross section strength between "non-PDD like" to "PDD like" 2p2h. The effect of this parameter have on the bias in energy reconstruction for 2p2h events at ND280 is shown in Figure 6.5. Therefore, all ν 2p2h interactions at SK receive a weight of $f_{2p2h_\nu} \times f_{2p2h_{CtoO}} \times f_{2p2h_{shape}}$ and all $\overline{\nu}$ $2p2h$ interactions at SK receive a weight of $f_{2p2h_{\overline{\nu}}} \times f_{2p2h_{CtoO}} \times f_{2p2h_{shape}}$.

All other interactions receive the same systematic treatment as in the previous analysis. Since ND280 is incapable of precisely measuring ν_e and $\overline{\nu}_e$ interaction cross sections, a theoretically motivated error is applied based on [131]. Addition uncertainties from neutral current modes are also considered which are not constrained by ND280. Table 6.17 shows the summary of the neutrino interaction parameters. Norm type parameters are normalisation parameters and shape type parameters have kinematic (energy, p, θ, E_{rec}) dependence.

6.4.4 Super-K detector uncertainties

The SK detector uncertainty and FSI+SI+PN uncertainty have been revised for the new fiTQun reconstruction method. The detector errors describe the mis-characterisation of final states (FS) based on the measured cut parameters values. The systematic errors are calculated for

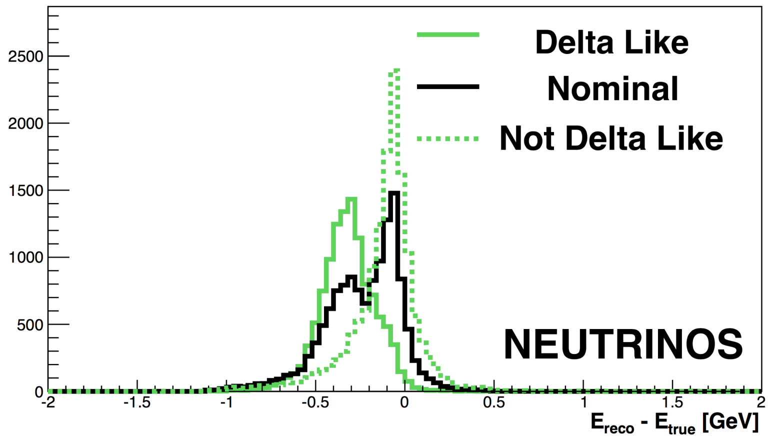

Figure 6.5: Bias in neutrino energy reconstruction for 2p2h events at ND280. The two extreme cases of “Not Delta Like” and “Delta Like” are obtained by setting the 2p2h shape parameter to -1 and 1 respectively.

Table 6.17: Summary of the neutrino interaction parameters using the results of ND280 fit. Starred errors are not constrained by the near detector.

Parameter	interaction categories applied	type
M_A^{QE}	CCQE	shape
p_F	CCQE	shape
2p2h norm. ν	2p2h	norm
2p2h norm. $\overline{\nu}$	2p2h	norm
2p2h norm. C to O	2p2h	norm
2p2h shape O	2p2h	shape
C_A^{RES}	CC1π and NC1π	shape
M_A^{RES}	CC1π and NC1π	shape
BG_A^{RES}	CC1π and NC1π	shape
CC other shape	CC other	shape
CC coherent	CC coherent	norm
NC coherent	NC coherent	norm
NC 1γ	NC 1γ	norm*
NC other	NC other	norm*
$\sigma_{\nu_e}/\sigma_{\nu_\mu}$	CC	norm*
$\sigma_{\bar{\nu}_e}/\sigma_{\bar{\nu}_\mu}$	CC	norm*
BeRPA A	CCQE	shape
BeRPA B	CCQE	shape
BeRPA D	CCQE	shape
BeRPA E	CCQE	shape

Event Type	Selection criteria
ν_e CC1e	ν_e CC && $N_{\pi^0} == 0$ && $N_{\pi^\pm} == 0$ && $N_P == 0$
ν_e CC other	ν_e CC && !(ν_e CC1e)
ν_μ CC1μ	ν_μ CC && $N_{\pi^0} == 0$ && $N_{\pi^\pm} == 0$ && $N_P == 0$
ν_μ CC	ν_μ CC && $N_{\pi^0} == 0$ && !(ν_μ CC1μ)
ν_μ CC$\mu\pi^0$ other	ν_μ CC && $N_{\pi^0} > 0$
NC 1π^0	NC && !(NCγ) && $N_{\pi^0} == 1$ && $N_{\pi^\pm} == 0$ && $N_P == 0$
NC π^0 other	NC && !(NCγ) && $N_{\pi^0} \geq 1$ && !(NC 1π^0)
NC γ	mode == 38 || mode == 39
NC 1$\pi^\pm$	NC && !(NCγ) && $N_{\pi^0} == 0$ && $N_{\pi^\pm} == 1$ && $N_P == 0$
NC other	NC && !(NC 1π^0) && !(NC π^0 other) && !(NCγ) && !(NC 1$\pi^\pm$)

Table 6.18: Criteria for event categorisation using final state information. Mode refers to the NEUT interaction mode number. The number of charged pions ($N_{\pi^\pm}$) and protons (N_P) only includes those particles produced with momentum above Cherenkov threshold set at 156.0 MeV/c and 1051.0 MeV/c respectively.

Table 6.19: Momentum binning of f^{sk} parameters for appearance samples

Neutrino Flavour	Interaction mode	Momentum Binning (GeV/c)
Osc. $\nu_e/\bar{\nu}_e$	CC	0-0.3, 0.3-0.7, 0.7-1.5
$\nu_\mu/\bar{\nu}_\mu$	CC	0-0.3, 0.3-0.7, 0.7-1.5
Bckgd. $\nu_e/\bar{\nu}_e$	CC	0-0.3, 0.3-0.7, 0.7-1.5
All	NC	0-0.3, 0.3-0.7, 0.7-1.5

the SK FS modes using the SK atmospheric neutrino control sample. The different FS modes are described in Table 6.18. The SK FS type error estimations are applied by generating 10^6 toy MC events and assign random Gaussian fluctuations of the FS mode errors for each event. The toy MC method is used to study fractional errors of event rates categorised by neutrino flavour, charged and neutral current, and $p - \theta$ or E_{rec} bins. The fractional shifts from the nominal values and correlation between each sample category are calculated and converted into a covariance matrix.

Appearance samples are divided into oscillated $\nu_e/\bar{\nu}_e$CC, $\nu_\mu/\bar{\nu}_\mu$CC, beam $\nu_e/\bar{\nu}_e$CC and NC modes. Disappearance samples into $\nu_\mu/\bar{\nu}_\mu$CCQE, $\nu_\mu/\bar{\nu}_\mu$CC Other, $\nu_e/\bar{\nu}_e$CC and NC modes. Some modes are divided into three bins in E_{rec} or P_{lepton}. This gives a total of 12+6+12+6+12 = 48 bins which are summarised in tables 6.19 and 6.20.

Table 6.20: Energy binning of f^{sk} parameters for disappearance samples

Neutrino Flavour	Interaction mode	Energy Binning (GeV)
$\nu_\mu/\bar{\nu}_\mu$	CCQE	0-0.4, 0.4-1.1, 1.1-30.0
$\nu_\mu/\bar{\nu}_\mu$	CC Other	0-30.0
$\nu_e/\bar{\nu}_e$	CC	0-30.0
All	NC	0-30.0

Final state interaction and secondary interaction model uncertainties Uncertainties from hadron re-interactions in the target nucleus (Final State Interaction, or FSI) and in the detector (Secondary Interaction, or SI) at SK are are added in quadrature to the SK matrix in order to reduce the total number of parameters in the analysis. Since the same model is used for FSI and SI, it is possible to evaluate the uncertainties in both FSI and SI simultaneously.

Photo-nuclear effect The SK detector simulation contains a model of the photo-nuclear effect i.e. the interaction of $\gamma - ray$ photons with nuclei. This process can lead to the absorption of a photon before it can pair-produce and generate Cherenkov light, in which case the photon would not be reconstructed. This has important consequences for the detection of π^0 which decay to two photons. This is also added in quadrature to the SK matrix.

Energy scale uncertainty The SK energy uncertainty is applied after the other nuisance parameters to find how the energy spectrum changes after multiplying the E_{rec} of all of the events by the $f^{E-scale}$ systematic parameter. We assume that events are uniformly distributed in each bin and thus that if a fraction $\alpha\%$ of the energy range covered by bin i moves into the range of bin $i+1$, that $\alpha\%$ of the events would behave in the same manner. The final pdf used in the likelihood is produced after this event migration has been calculated.

6.4.5 Effect of the systematic parameters

The effects of the systematic parameters are described in this section. By making a large number of throws of different subsets of the systematic parameters, as well as all in concert, we can determine the contribution to the uncertainty from each error source (Beam flux, cross-section model etc.) and the reduction in the uncertainty due to the near-detector constraint.

The uncertainties on the predicted event rates are estimated by making 10,000 throws of the systematic and oscillation parameters and evaluating the RMS of the predicted event rates among the throws. Table 6.21 summarises the systematic errors from each error source, using oscillation parameter Set A in Table 6.1 and 1.47×10^{21} POT and 0.76×10^{21} POT for FHC and RHC respectively. Tables A.6-A.10 shows comparisons between pre-BANFF fit and post-BANFF fit.

The non-constrained parameters here are NC1γ, NC other, and the ν_e/ν_μ and $\bar{\nu}_e/\bar{\nu}_\mu$ cross-section ratio parameters whose error sizes hardly change with BANFF constraint. The constrained parameters here are the flux parameters and the other xsec parameters. The variation of the event rates with BANFF non-constrained parameters is not so large between when BANFF prefit parameters are used and when BANFF postfit parameters are used.

Table 6.21: Percent errors on the predicted event rates in each sample. The last column is the error on the ratio of predicted event rates in the neutrino and antineutrino mode 1Re samples.

	1Rmu		1Re			
Error Source	FHC	RHC	FHC	RHC	FHC 1 d. e.	FHC/RHC
SK Detector	1.9	1.6	3.0	4.2	16.5	1.6
SK FSI+SI+PN	2.2	2.0	2.9	2.5	11.3	1.6
SK Detector+FSI+SI+PN	2.9	2.5	4.2	4.8	19.2	2.1
ND280 const. flux & xsec	3.3	2.7	3.2	2.9	4.1	2.5
$\sigma(\nu_e)/\sigma(\nu_\mu)$, $\sigma(\overline{\nu}_e)/\sigma(\overline{\nu}_\mu)$	0.0	0.0	2.6	1.5	2.6	3.1
NC1γ	0.0	0.0	1.1	2.6	0.3	1.5
NC Other	0.3	0.3	0.1	0.3	1.0	0.2
Syst. Total	4.4	3.8	6.3	6.4	19.6	4.7

6.5 Sensitivity studies

This section describes sensitivity studies for the five sample fit assuming 1.47×10^{21} POT in FHC and 0.76×10^{21} POT in RHC which is equal to the total T2K-SK Run1-8 data.

The same two sets of "true" oscillation parameter values were used as in Section 6.2.2. Rather than average over the results of many toy data sets throwing the systematic parameters, the sensitivities presented are derived only from a fit to a single data set generated with all of the systematic parameters at their central values. This is referred to as the "Asimov" data set [132], a single data set representative of the distribution of possible data sets. Within the fit itself, the systematic parameters are marginalised. This method saves a great deal of computation time. The result of the fits can be viewed as a "Asimov Sensitivity": the contours from this Asimov fit will indicate the ability to measure the oscillation parameters, in the absence of statistical fluctuations if the true parameter values are the input values.

The sensitivities have been evaluated both with and without the reactor constraint. The best fit point, denoted by a triangle marker, is the centre of the highest bin in the likelihood surface. For the two-dimensional contours the normal and inverted hierarchy $\Delta\chi^2$ are calculated with respect to their own χ^2 minima. For the one-dimensional case a single global minimum is used. We use the posterior probability for the hierarchies to evaluate the datas preference for one hierarchy or the other, the Asimov fit results are shown in section 6.5.2. The results have been compared with the other two fitting frameworks and we see consistent sensitivities for Asimov Set A and Asimov Set B.

The results for Set A are presented in Figures 6.6-6.8. As expected, the best fit points from the fits are close to the input oscillation parameters set values. Note in Figure 6.6 the change in octant preference from low to high when the reactor constraint is applied and δ_{CP} is constrained towards negative values. A stronger preference of mass hierarchy is seen in figure 6.8b with the difference of $\Delta\chi^2$ values at best-fit point between the two hierarchies is larger when including reactor constraint. This is expected since a stronger constraint on $\sin^2\theta_{13}$ gives additional power to separate between the two hierarchies.

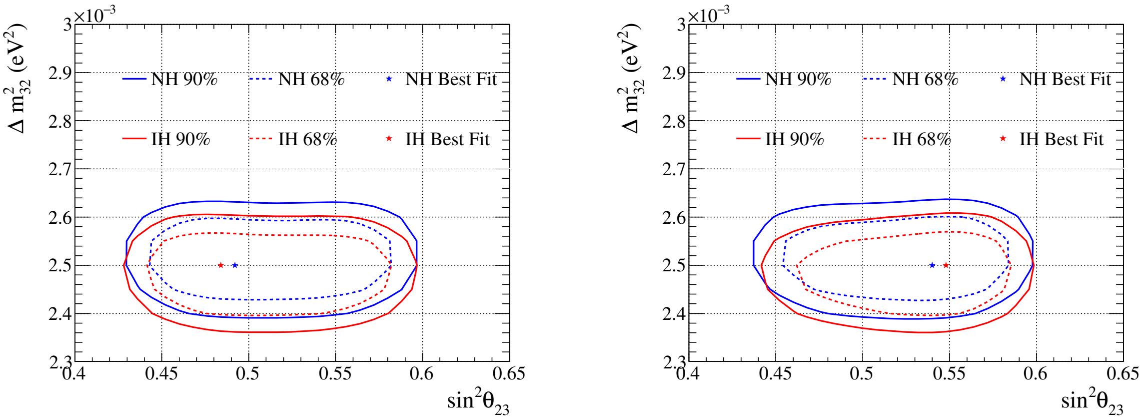

(a) T2K only (b) T2K + reactor

Figure 6.6: Asimov sensitivity 2D confidence level contours in $|\Delta m^2_{32}|$ vs.$\sin^2\theta_{23}$ for normal and inverted hierarchy using Set A

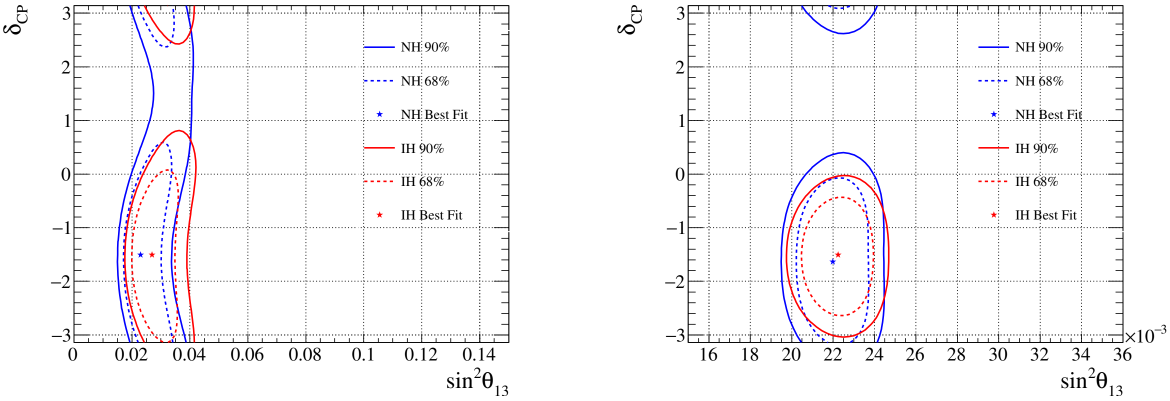

(a) T2K only (b) T2K + reactor

Figure 6.7: Asimov sensitivity 2D confidence level contours in δ_{CP} vs. $\sin^2\theta_{13}$ for normal and inverted hierarchy using Set A

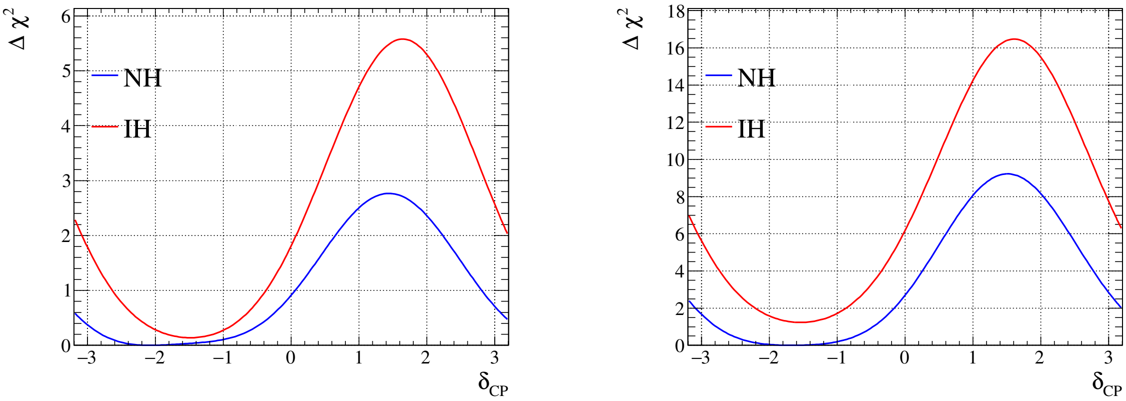

(a) T2K only (b) T2K + reactor

Figure 6.8: Asimov sensitivity 1D $\Delta\chi^2$ in δ_{CP} for normal and inverted hierarchy using Set A

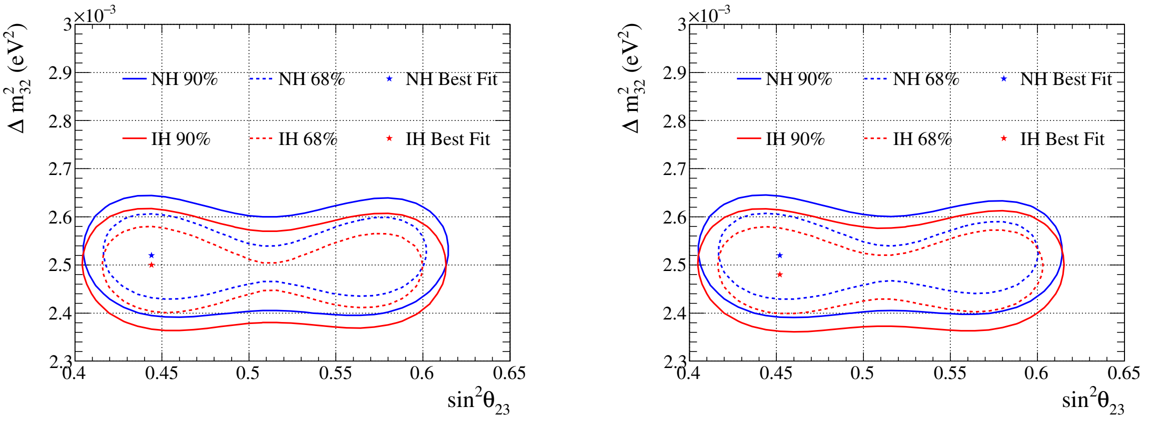

(a) T2K only (b) T2K + reactor

Figure 6.9: Asimov sensitivity 2D confidence level contours in $|\Delta m^2_{32}|$ vs.$\sin^2\theta_{23}$ for normal and inverted hierarchy using Set B

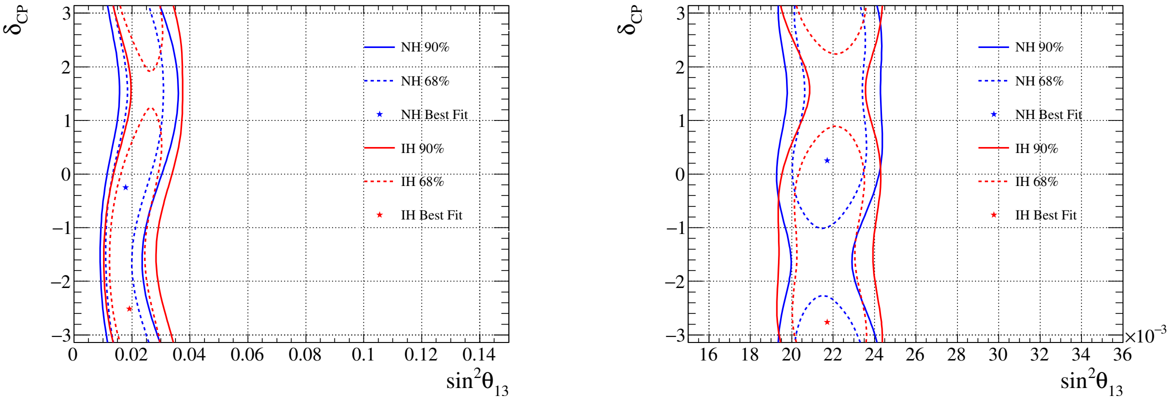

(a) T2K only (b) T2K + reactor

Figure 6.10: Asimov sensitivity 2D confidence level contours in δ_{CP} vs. $\sin^2\theta_{13}$ for normal and inverted hierarchy using Set B

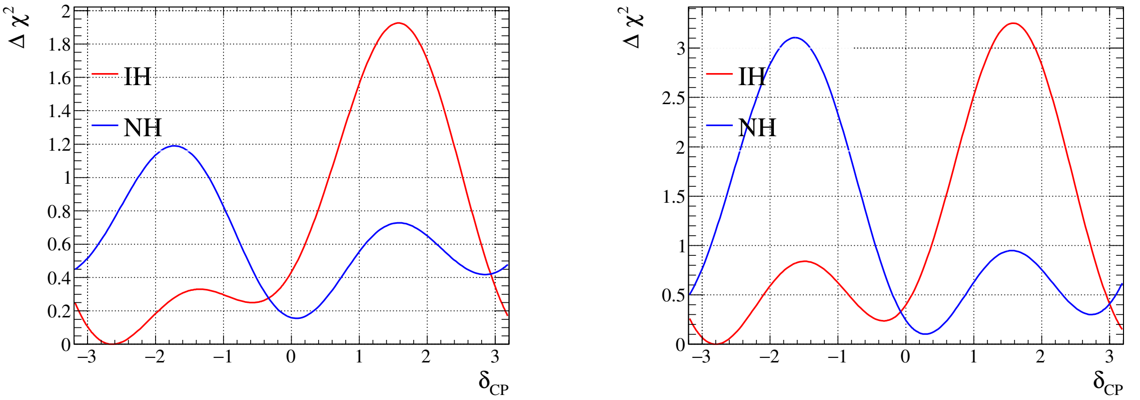

(a) T2K only (b) T2K + reactor

Figure 6.11: Asimov sensitivity 1D $\Delta\chi^2$ in δ_{CP} for normal and inverted hierarchy using Set B

The results for Set B follow in Figures 6.9-6.11. Since the δ_{CP} value in this case is set to zero, the expected exclusion ranges for δ_{CP} are smaller compared to oscillation parameter set A. These are shown in Figure 6.11a and 6.11b. It is interesting to note that although Set B uses the normal hierarchy as the true configuration, the best fit prefers the inverted hierarchy. This occurs as a result of marginalising over all of the other parameters. At some values of δ_{CP} the inverted hierarchy χ^2 is lower averaging over values of the latent parameters. The difference in the χ^2 between the best fit points for normal and inverted hierarchy in these instances is very small and thus while a preference for the wrong hierarchy exists, it is very weak indeed and no statement about real data could be made in such circumstances.

6.5.1 Sensitivity studies using Credible Intervals

This section presents the results of sensitivity studies for δ_{CP} using one-dimensional credible intervals. The same marginal likelihoods were used as for the confidence level sensitivity in the previous section. The credible intervals are constructed by treating the marginal likelihood as proportional to the posterior probability. Sensitivities using oscillation parameter Set A can be found in Figures 6.12 to 6.14 and using Set B in Figures 6.15 to 6.17.

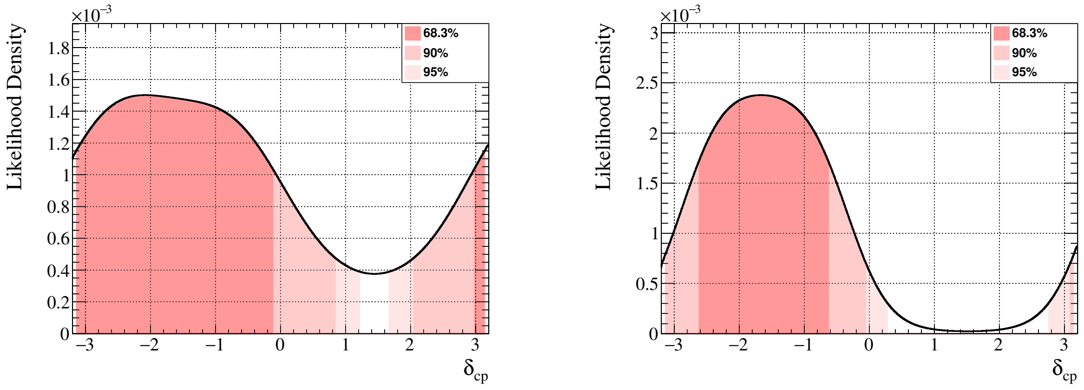

(a) T2K only

(b) T2K + reactor

Figure 6.12: 68.3%, 90% and 95% 1D Credible intervals in δ_{CP} for the normal hierarchy fit, oscillation parameter Set A

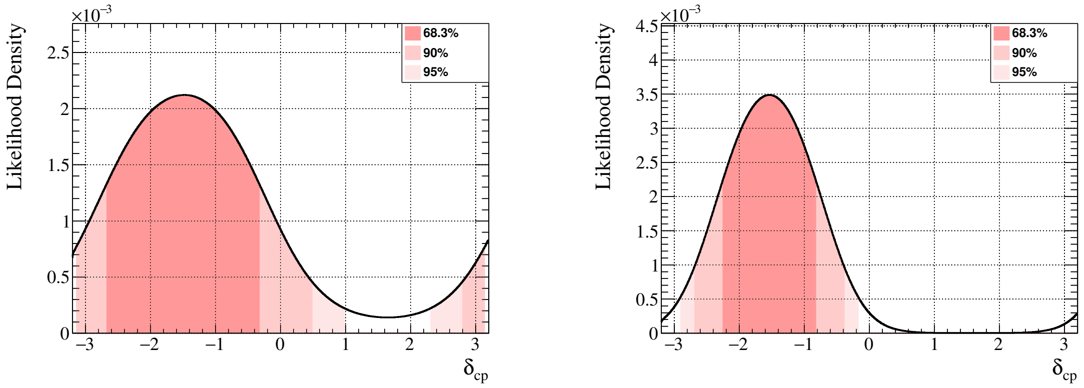

(a) T2K only

(b) T2K + reactor

Figure 6.13: 68.3%, 90% and 95% 1D Credible intervals in δ_{CP} for the inverted hierarchy fit, oscillation parameter Set A

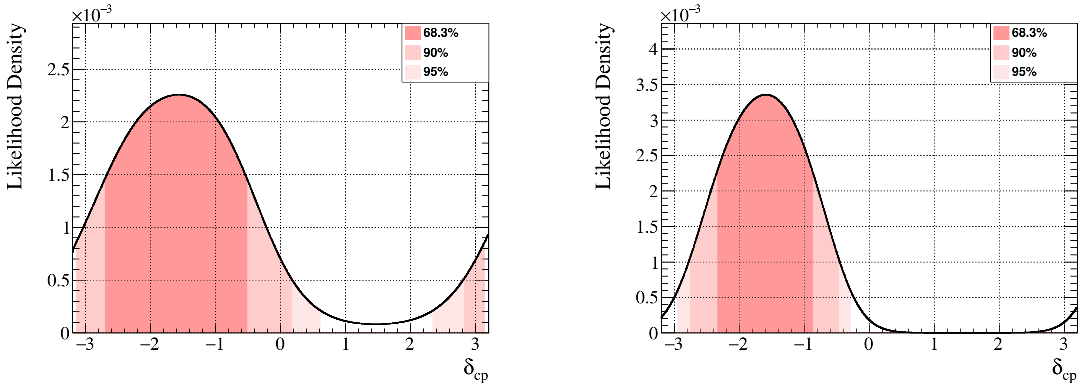

(a) T2K only

(b) T2K + reactor

Figure 6.14: 68.3%, 90% and 95% 1D Credible intervals in δ_{CP} for both hierarchies, oscillation parameter Set A

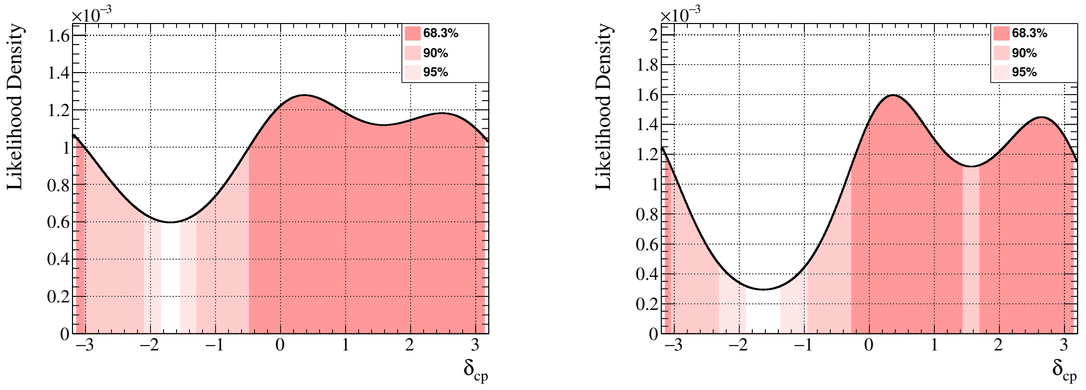

(a) T2K only

(b) T2K + reactor

Figure 6.15: 68.3%, 90% and 95% 1D Credible intervals in δ_{CP} for the normal hierarchy fit, oscillation parameter Set B

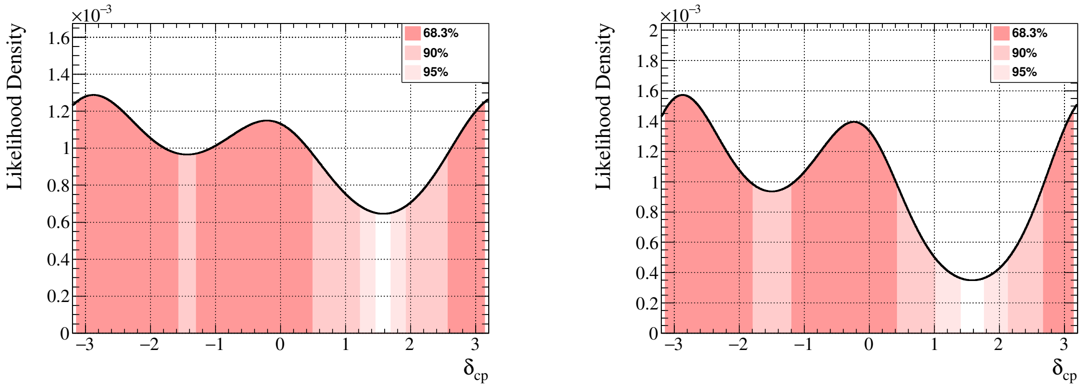

(a) T2K only

(b) T2K + reactor

Figure 6.16: 68.3%, 90% and 95% 1D Credible intervals in δ_{CP} for the inverted hierarchy fit, oscillation parameter Set B

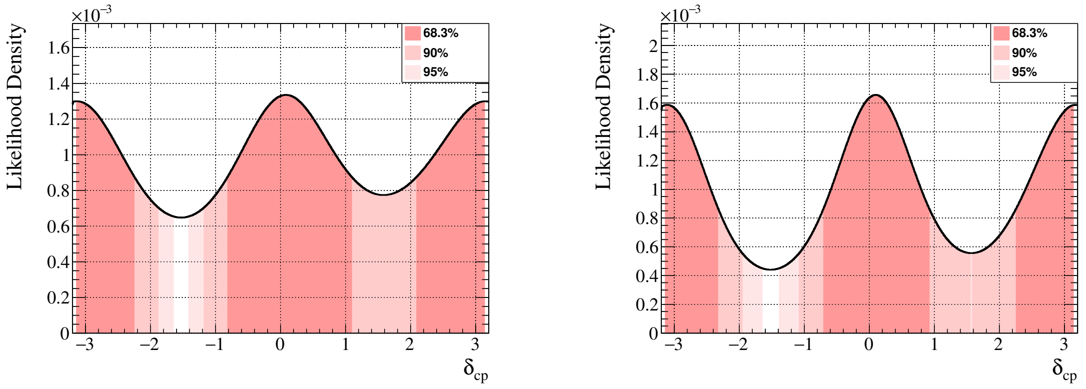

(a) T2K only

(b) T2K + reactor

Figure 6.17: 68.3%, 90% and 95% 1D Credible intervals in δ_{CP} for both hierarchies, oscillation parameter Set B

6.5.2 Comparison of hypotheses on mass hierarchy and $\sin^2\theta_{23}$ octant

We also look at the posterior probability of different hypotheses. Here we consider the mass hierarchy and the octant of θ_{23}. We define the posterior probability of an hypothesis H_i as:

$$P(H_i|N^{obs.},\boldsymbol{x}) = \frac{\mathcal{L}_{marg}(N^{obs.},\boldsymbol{x},H_i)P(H_i)}{\sum\limits_j \mathcal{L}_{marg}(N^{obs.},\boldsymbol{x},H_j)P(H_j)} \tag{6.18}$$

Where:

- the hypothesis H_j runs through the 4 combinations which can be made with the two mass hierarchies and the two octants for θ_{23}.
- the likelihood of the observed measurement $(N^{obs.},\boldsymbol{x})$ in the hypothesis H_i is given by the marginal likelihood for this hypothesis. The range over which $\sin^2(\theta_{23})$ is integrated is adjusted depending on the octant corresponding to H_i.
- the prior probabilities for each hypothesis are taken equal, $P(H_j) = 0.25$ for all j.

The posterior probabilities for the various combinations of mass hierarchies and octants for Asimov A and B are summarised in tables 6.22 and 6.23. Reactor constrain is imposed to give better ability to constrain models.

Table 6.22: Posterior probabilities for different hypotheses assuming Asimov A oscillation parameters.

	$\sin^2 2\theta_{23} < 0.5$	$\sin^2 2\theta_{23} > 0.5$	Line total
Inverted hierarchy	0.07	0.21	0.28
Normal hierarchy	0.22	0.50	0.72
Column total	0.29	0.71	1

Table 6.23: Posterior probabilities for different hypotheses assuming Asimov B oscillation parameters.

	$\sin^2 2\theta_{23} < 0.5$	$\sin^2 2\theta_{23} > 0.5$	Line total
Inverted hierarchy	0.23	0.29	0.52
Normal hierarchy	0.24	0.25	0.49
Column total	0.47	0.54	1

6.6 Data fit results

In this section are the results obtained when fitting the four one-ring CCQE-like samples and a one-ring CC1π-like sample observed at Super-Kamiokande over the 2009-2017 T2K data sets. This dataset is made of 74 1Re and 240 1Rμ candidate events in FHC mode, 7 1Re and 68 1Rμ in RHC mode, and 15 1R ν_e CC1π candidate events which passed all the selection cuts [133]. The five samples are reproduced in the variables used for the analysis in Figure 6.18. This is important when considering the fit results compared to the sensitivities in the previous section. We will first present the results obtained when using a frequentist approach, where we build confidence intervals for the parameters, and then additional results obtained when following a Bayesian approach. For the mass splittings, we will be giving the results for $|\Delta m^2_{32}|$ in the normal hierarchy, and $|\Delta m^2_{31}|$ in the inverted hierarchy.

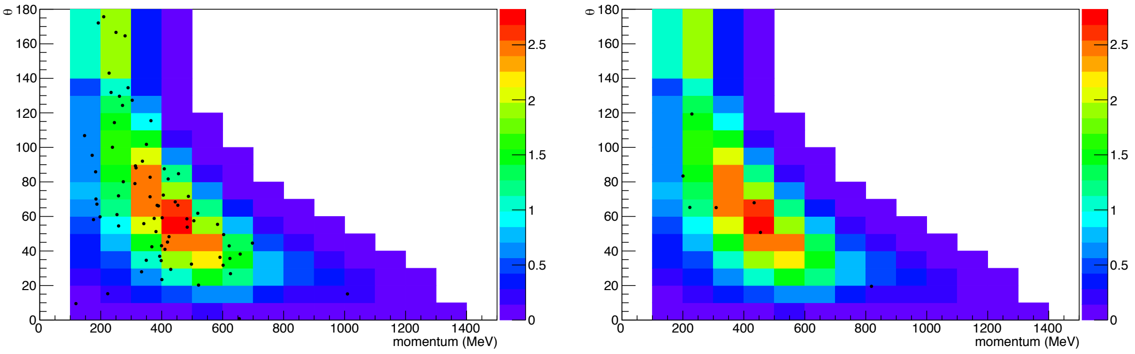

(a) FHC 1Re (b) RHC 1Re

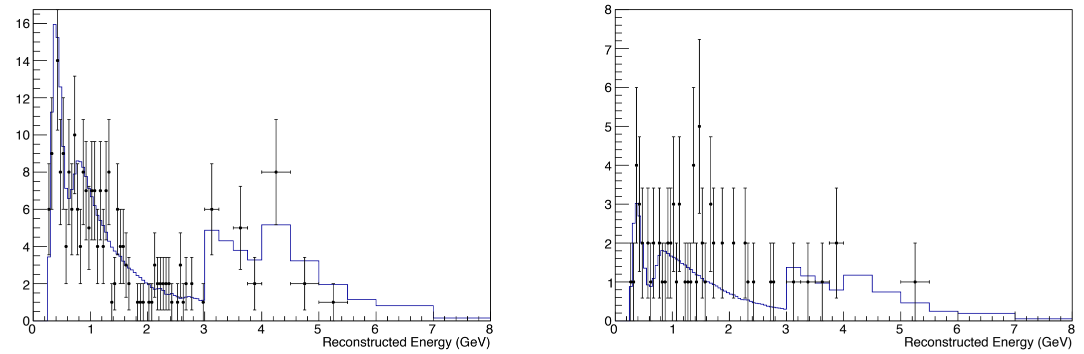

(c) FHC 1Rμ (d) RHC 1Rμ

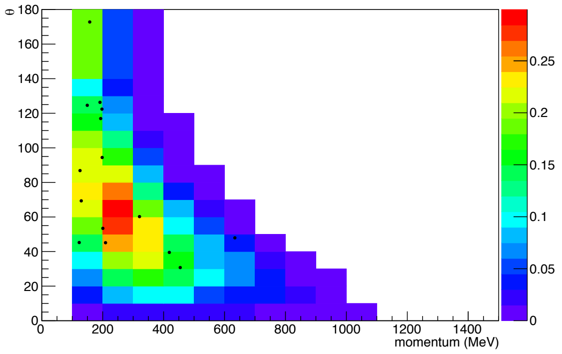

(e) FHC 1R ν_e CC1π^+

Figure 6.18: Events of the Run 1-8 data set for all five samples considered, overlay with spectra produced using best fit points from Section 6.6.1 assuming NH.

6.6.1 Global Best-fit Results

Results for T2K only data

We will start by fitting the T2K data without external constraints for the four oscillation parameters allowed to vary. Performing a simple minimisation over the systematic and oscillation parameters yields a best fit point in the 4D oscillation space. Best fit values for the individual parameters are given in table 6.24 for the normal hierarchy case, and in table 6.25 for the inverted hierarchy case.

Table 6.24: Results of the fit of the T2K run 1-8 data in the normal hierarchy

Parameter	Best fit
$\sin^2(2\theta_{13})$	0.105
δ_{CP}	-2.02
$\lvert\Delta m^2_{32}\rvert(\mathrm{eV}^2/\mathrm{c}^4)$	2.46×10^{-3}
$\sin^2(\theta_{23})$	0.518

Table 6.25: Results of the fit of the T2K run 1-8 data in the inverted hierarchy

Parameter	Best fit
$\sin^2(2\theta_{13})$	0.120
δ_{CP}	-1.22
$\lvert\Delta m^2_{31}\rvert(\mathrm{eV}^2/\mathrm{c}^4)$	2.44×10^{-3}
$\sin^2(\theta_{23})$	0.520

Results with reactor constraint for $\sin^2(2\theta_{13})$

In this section are the results obtained when fitting the T2K data while constraining the variations of $\sin^2(2\theta_{13})$ in the fit using the results of the reactor experiments. We will take for this the value coming from the PDG 2016 summary table:

$$\sin^2(2\theta_{13}) = 0.0857 \pm 0.0046$$

and so a Gaussian constraint is applied with mean 0.0857 and σ 0.0046 for $\sin^2(2\theta_{13})$. The best fit values obtained for the different parameters in both mass hierarchies are shown in tables 6.26 and 6.27.

Table 6.26: Results of the fit of the T2K run 1-8 data in the normal hierarchy

Parameter	Best fit
$\sin^2(2\theta_{13})$	0.087
δ_{CP}	-1.77
$\lvert\Delta m^2_{32}\rvert(\mathrm{eV}^2/\mathrm{c}^4)$	2.46×10^{-3}
$\sin^2(\theta_{23})$	0.528

Table 6.27: Results of the fit of the T2K run 1-8 data in the inverted hierarchy

Parameter	Best fit
$\sin^2(2\theta_{13})$	0.088
δ_{CP}	-1.44
$\lvert\Delta m^2_{31}\rvert(\mathrm{eV}^2/\mathrm{c}^4)$	2.44×10^{-3}
$\sin^2(\theta_{23})$	0.533

6.6.2 Frequentist results using marginalisation

In this section can be found the confidence level contours for the data fit. They are built using the fixed $\Delta\chi^2$ method on the distribution of the 1D/2D marginal likelihood for the parameter(s) considered (marginalised over the nuisance parameters, and all the other oscillation parameters). Figure 6.19 shows the contours in $\sin^2\theta_{23}$ vs. Δm^2_{32} space. For both T2K only and T2K plus reactor the best fit point lies in the higher octant with T2K only best fit point lies closer to maximal oscillation. Figure 6.20 shows the contours in δ_{CP} vs. $\sin^2\theta_{13}$ space. Here the contours for normal and inverted hierarchy are constructed relative to a common χ^2 minimum. Figure 6.21 shows the $\Delta\chi^2$ distribution as a function of δ_{CP} . Even assuming normal hierarchy without reactor constrain, $\delta_{CP} = 0$ is still excluded at 2σ CL. These results are presented with local contours for each hierarchy hypothesis, expect for 1D $\Delta\chi^2$ distribution for δ_{CP} , where global minimum is used. The preference in hierarchy will be evaluated using the posterior probabilities in the Bayesian approach shown in the next section.

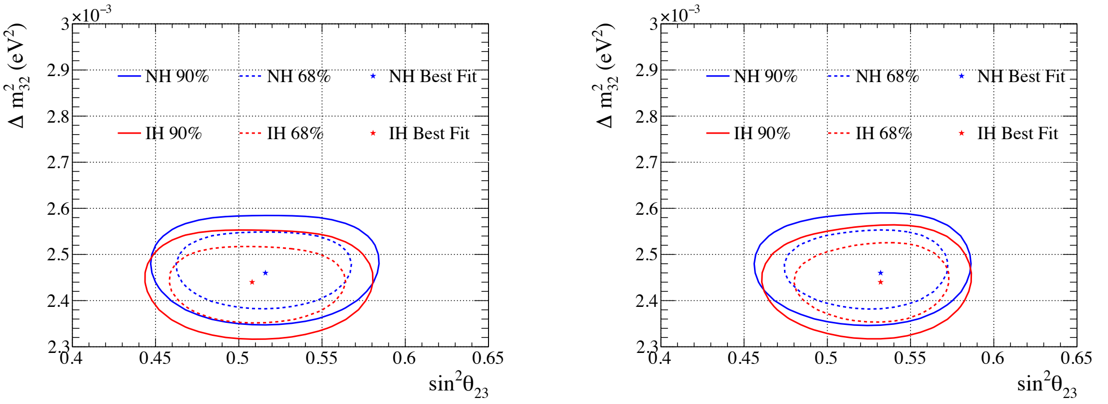

(a) T2K only

(b) T2K + reactor

Figure 6.19: 2D confidence level contours in $|\Delta m^2_{32}|$ vs. $\sin^2\theta_{23}$ for normal and inverted hierarchy. These results are presented with local contours for each hierarchy hypothesis.

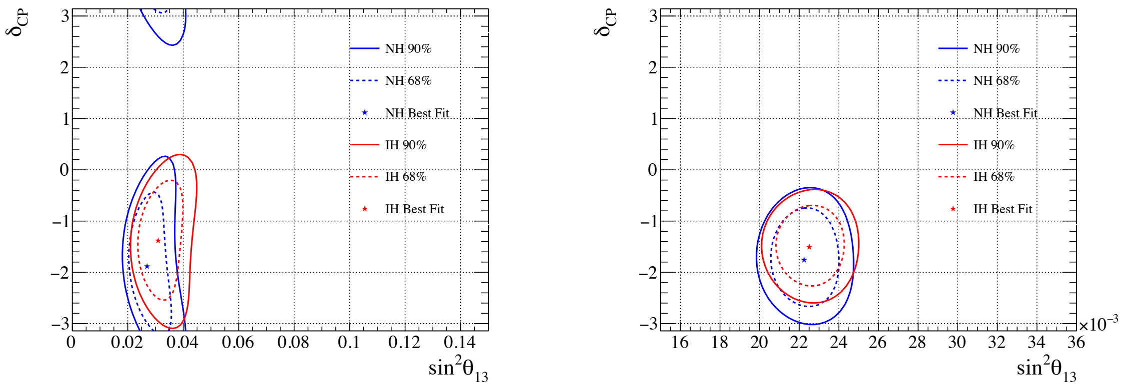

(a) T2K only

(b) T2K + reactor

Figure 6.20: 2D confidence level contours in δ_{CP} vs. $\sin^2\theta_{13}$ for normal and inverted hierarchy. These results are presented with local contours for each hierarchy hypothesis.

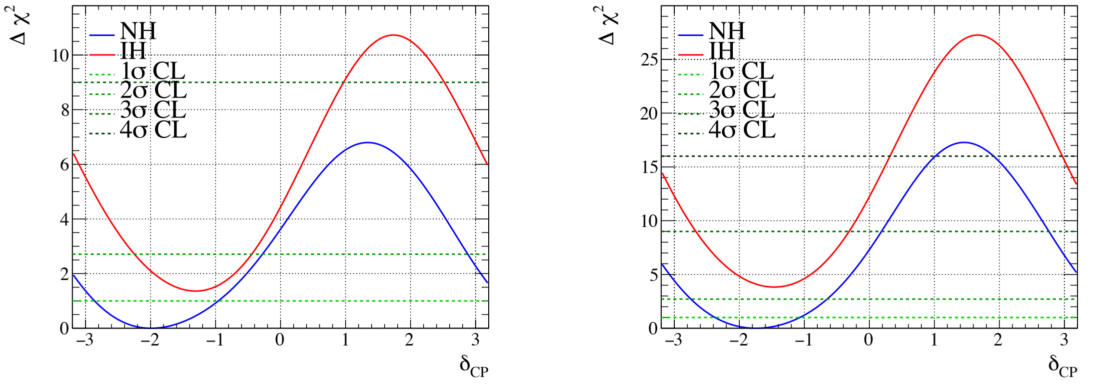

(a) T2K only

(b) T2K + reactor

Figure 6.21: 1D $\Delta\chi^2$ plots in δ_{CP} for normal and inverted hierarchy. Global minimum is used for 1D results. Confidence level intervals have been built using the fixed $\Delta\chi^2$ method.

6.6.3 Bayesian results using marginalisation

Here, instead of the $\Delta\chi^2$ distribution, we can look at the posterior probability for this parameter, and build credible intervals from it. An additional difference is that we can also marginalise over the mass hierarchy, taken as a discrete variable with two values to which we can assign prior probabilities P(NH) and P(IH). The normal hierarchy scenario corresponds to P(NH)=1 and P(IH)=0, the inverted hierarchy one to P(NH)=0 and P(IH)=1. When marginalising over the mass hierarchy we will assume that both hierarchies were equally likely before the fit and take P(NH)=P(IH)=0.5. The posterior probability for δ_{CP} is then given in each case by:

$$P(\delta_{CP}) = \alpha \times [\mathcal{L}_{marg}(\delta_{CP}|NH)P(NH) + \mathcal{L}_{marg}(\delta_{CP}|IH)P(IH)] \tag{6.19}$$

where α is a constant so that the probability over the whole range $[-\pi;\pi]$ is equal to 1.

In the section below can be found 1D Bayesian credible intervals in δ_{CP} for normal hierarchy, inverted hierarchy and both together. Equivalent intervals in $\sin^2 2\theta_{13}$, $\sin^2\theta_{23}$ and Δm^2_{32} can be found in section B. Below the plots/analysis are tables summarising the extent of the credible intervals for all four parameters. Within each table the second column contains the most probable value (MPV), the peak of the posterior likelihood, and the third and fourth columns contain the distance from the MPV to the lower and upper edges of the 68.3% credible interval. These intervals form a clear and concise way to represent the fit results and have therefore been chosen as the primary result from this thesis. From Figure 6.24 using the reactor prior on $\sin^2 2\theta_{13}$, δ_{CP} =0 is excluded at the 95% level. From figures B.3 we can see that the reactor constraint clearly dominates the posterior in $\sin^2\theta_{13}$, but also has a clear effect on $\sin^2\theta_{23}$ shown in figures B.6, causing it to favour the higher octant.

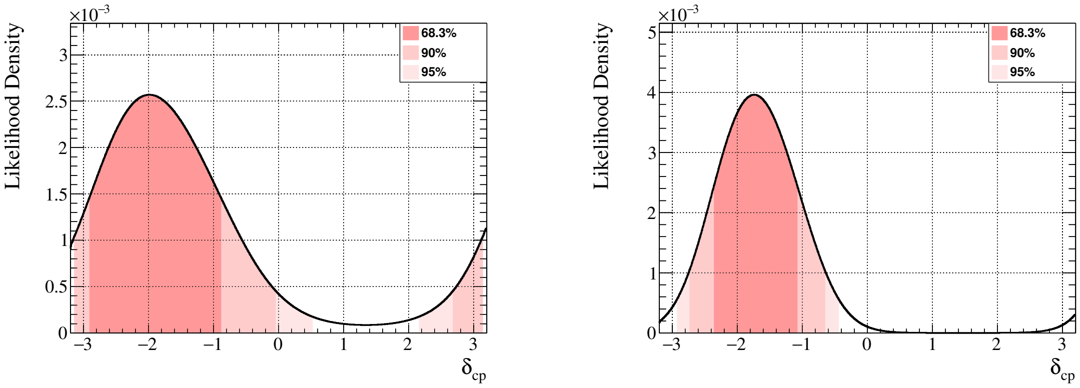

(a) T2K only (b) T2K + reactor

Figure 6.22: 1D Credible intervals in δ_{CP} for the normal hierarchy fit

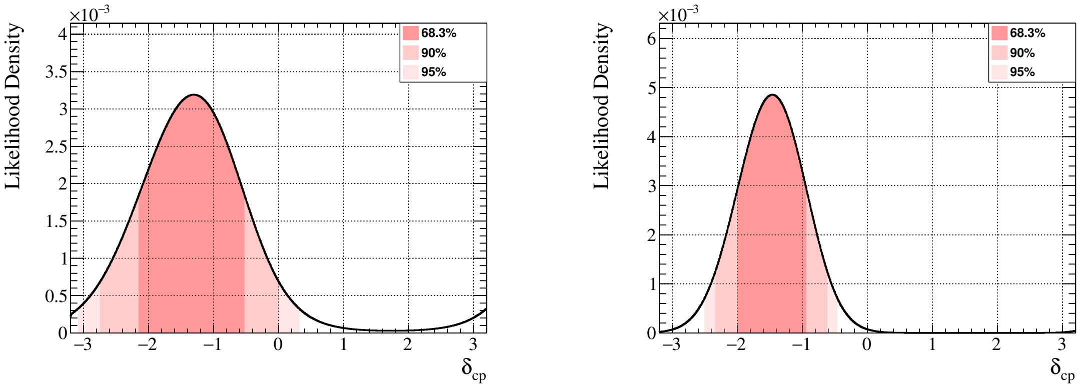

(a) T2K only (b) T2K + reactor

Figure 6.23: 1D Credible intervals in δ_{CP} for the inverted hierarchy fit

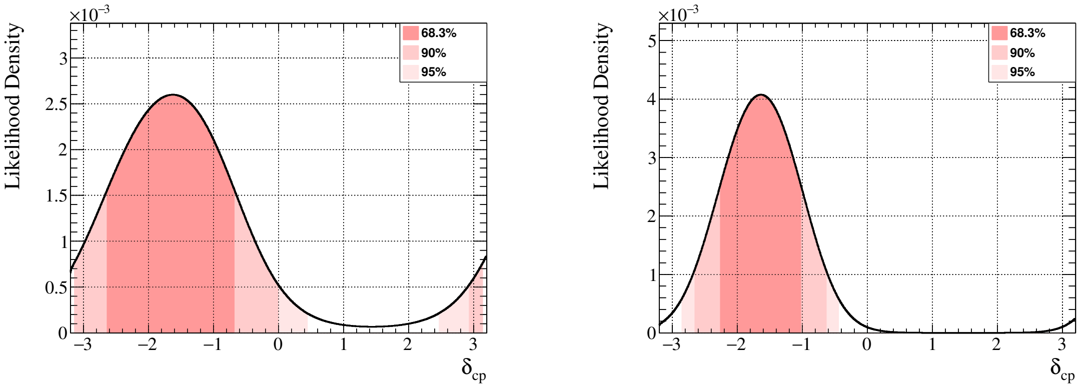

(a) T2K only (b) T2K + reactor

Figure 6.24: 1D Credible intervals in δ_{CP} for both hierarchies

Table 6.28: Credible intervals for $\sin^2 2\theta_{13}$ using T2K only and with the reactor constraint

	Hierarchy	Most Probable Value	Lower Range	Upper Range
T2K only	Normal	0.1099	0.0185	0.0218
	Inverted	0.1242	0.0203	0.0236
	Both	0.1147	0.0197	0.0247
T2K + reactor	Normal	0.0875	0.0045	0.0043
	Inverted	0.0882	0.0043	0.0055
	Both	0.0876	0.0044	0.0045

Table 6.29: Credible intervals for $\sin^2\theta_{13}$ using T2K only and with the reactor constraint

	Hierarchy	Most Probable Value	Lower Range	Upper Range
T2K only	Normal	0.0283	0.0049	0.0058
	Inverted	0.0321	0.0054	0.0064
	Both	0.0296	0.0052	0.0066
T2K + reactor	Normal	0.0224	0.0012	0.0011
	Inverted	0.0226	0.0011	0.0012
	Both	0.0224	0.0012	0.0012

Table 6.30: Credible intervals for $\sin^2\theta_{23}$ using T2K only and with the reactor constraint

	Hierarchy	Most Probable Value	Lower Range	Upper Range
T2K only	Normal	0.512	0.031	0.036
	Inverted	0.509	0.031	0.037
	Both	0.511	0.032	0.036
T2K + reactor	Normal	0.529	0.035	0.029
	Inverted	0.527	0.028	0.033
	Both	0.530	0.034	0.028

Table 6.31: Credible intervals for Δm^2_{32} (Δm^2_{31}) using T2K only and with the reactor constraint

	Hierarchy	Most Probable Value	Lower Range	Upper Range
T2K only	Normal	2.471	0.057	0.057
	Inverted	2.439	0.056	0.056
	Both	2.458	0.059	0.058
T2K + reactor	Normal	2.469	0.055	0.058
	Inverted	2.440	0.056	0.056
	Both	2.462	0.057	0.059

Table 6.32: Credible intervals for δ_{CP} using T2K only and with the reactor constraint

	Hierarchy	Most Probable Value	Lower Range	Upper Range
T2K only	Normal	-1.98	0.0.92	1.09
	Inverted	-1.31	0.84	0.78
	Both	-1.72	0.92	1.04
T2K + reactor	Normal	-1.73	0.63	0.65
	Inverted	-1.47	0.52	0.52
	Both	-1.64	0.62	0.62

Comparison of hypotheses on mass hierarchy and $\sin^2\theta_{23}$ octant

The posterior probabilities for the various combinations of mass hierarchies and octants are summarised in tables 6.33 and 6.34. The Bayes factor which is the ratio of the posterior likelihood is used to interpret the results. We can see that when using the results of the reactor experiment as a prior for $\sin^2(2\theta_{13})$, the T2K data favours the normal hierarchy with a Bayes factor of 7.47, stronger than previously reported in the last analysis, but still considered a weak preference according to [134]. The preference for the normal hierarchy from this analysis is somewhat stronger than that found by the MaCh3 group [124]. There is also a preference to the higher octant with a Bayes factor of 3.24.

Table 6.33: Posterior probabilities for different hypotheses from T2K run 1-8 only

	$\sin^2 2\theta_{23} < 0.5$	$\sin^2 2\theta_{23} > 0.5$	Line total
Inverted hierarchy	0.107	0.187	0.294
Normal hierarchy	0.254	0.452	0.706
Column total	0.361	0.639	1

Table 6.34: Posterior probabilities for different hypotheses from T2K run 1-8 data and the results of the reactor experiments.

	$\sin^2 2\theta_{23} < 0.5$	$\sin^2 2\theta_{23} > 0.5$	Line total
Inverted hierarchy	0.022	0.096	0.118
Normal hierarchy	0.214	0.668	0.882
Column total	0.236	0.764	1

6.6.4 Significance and Coverage Studies using Feldman-Cousins Method

Since the parameter δ_{CP} is periodic and the likelihood is clearly non-Gaussian (as shown in Figure 6.21), limits base on a Gaussian approximation are unlikely to have correct coverage. Therefore, we produced the critical $\Delta\chi^2$ values for δ_{CP} using the Feldman-Cousins approach [130]. In order to perform the study, 10,000 toy MC experiments are generated with fixed value of δ_{CP} and randomly thrown values for the other oscillation parameters according to the considerations of the data fit and the reactor experiment. In the last analysis the toy experiments take the posterior likelihood distributions (separately for normal and inverted hierarchies) in $\sin^2\theta_{23}$ - Δm^2_{32} space based on the data fit results. T2K has decided to use instead the posterior likelihood distributions from Asimov disappearance fits, which use best fits points from Run 1-8 data fits for $\sin^2\theta_{23}$ and Δm^2_{32} , and a Gaussian distribution of $\sin^2 2\theta_{13}$ based on the reactor experiment ($\sin^2 2\theta_{13} = 0.0857 \pm 0.0046$). The distributions of oscillation parameters used to generate the toys are shown in Figure 6.25.

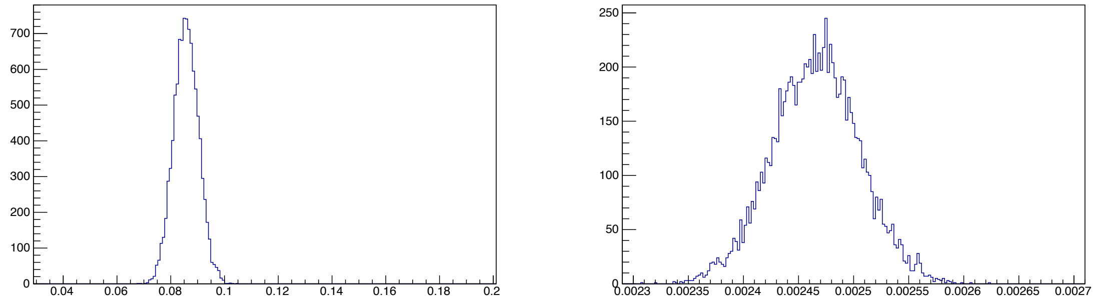

(a) $\sin^2 2\theta_{13}$ (b) Δm^2_{32}

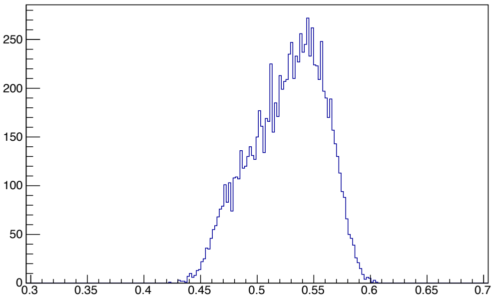

(c) $\sin^2\theta_{23}$

Figure 6.25: 1D distributions of oscillation parameters for generating toy experiments used for F&C studies from Asimov NH fit.

The $\Delta\chi^2$ values are calculated based on the difference between the χ^2 values calculated using the true values of δ_{CP} and mass hierarchy of interest and the best fit values:

$$\Delta\chi^2(\delta_{CP}, MH) = \chi^2(\delta^{true}_{CP}, MH^{true}) - \chi^2(\delta^{bf}_{CP}, MH^{bf}) \tag{6.20}$$

with MH is mass hierarchy, δ^{true}_{CP} and MH^{true} are the true values of δ_{CP} and mass hierarchy, and δ^{bf}_{CP} and MH^{bf} are the best-fit values. The critical $\Delta\chi^2$ value for each δ_{CP} step is decided by evaluating at which $\Delta\chi^2$ value the distribution contains X% of the toy experiment results.

The X% is decided based on the Gaussian approximation. in this study, we consider the critical $\Delta\chi^2$ values for 1σ, 90% confidence level, and 2σ significances for 9 δ_{CP} steps between $-\pi$ and $+\pi$ in an increment of $\pi/4$.

Figure 6.26 shows the distributions of the critical $\Delta\chi^2$ values obtained with the Feldman-Cousins method for each true δ_{CP} step for both normal and inverted hierarchy.

The obtained critical value distributions are used to evaluate the 2σ confidence level of the δ_{CP} with correct coverage. Using the Feldman-Cousins method, it gives the δ_{CP} values of [-2.894,-0.561] and [-1.504,-1.265] at 2σ confidence level for normal hierarchy hypotheses inverted hierarchy hypotheses respectively as shown in Figure 6.27.

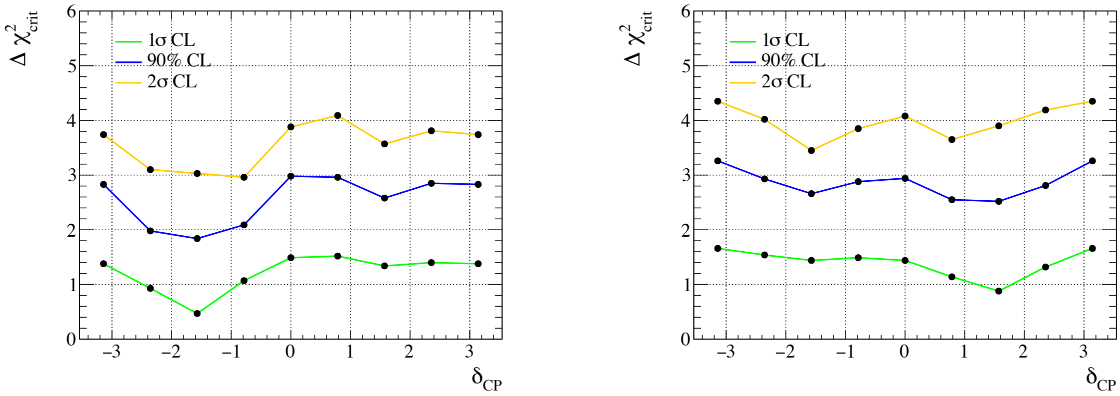

(a) NH

(b) IH

Figure 6.26: Distributions of the critical $\Delta\chi^2$ values obtained with the Feldman-Cousins methods as a function of true δ_{CP} value for normal hierarchy (left) and inverted hierarchy (right). Each step provides the critical value calculated with the statistical uncertainty considering the binomial fluctuation with linear interpolation between points. Green, blue, and yellow lines represent the critical values obtained by considering the 1σ, 90%, and 2σ confidence level, respectively.

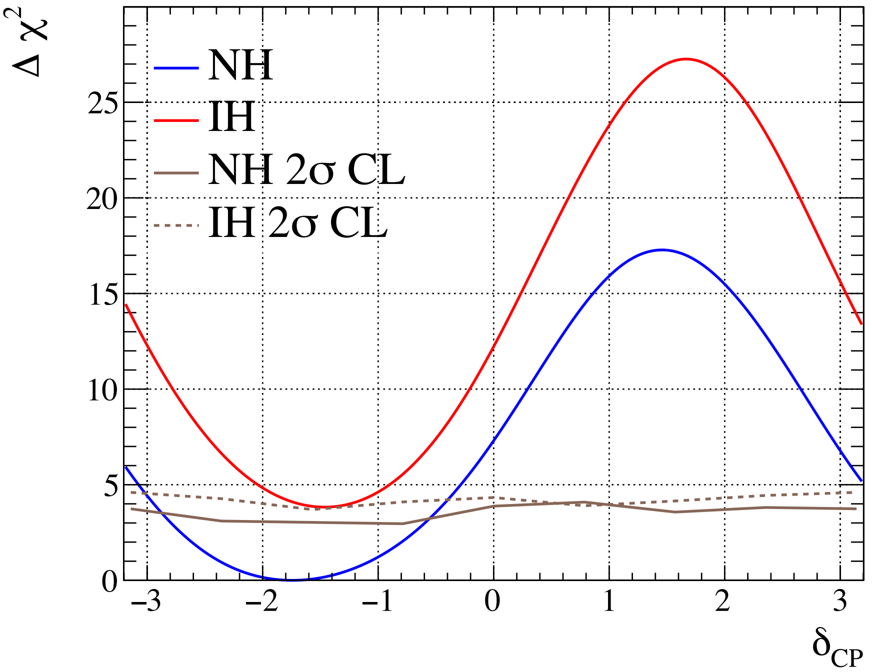

Figure 6.27: 1D $\Delta\chi^2$ distribution as a function of δ_{CP} of the data fit with reactor constraint. The critical $\Delta\chi^2$ values obtained with the Feldman-Cousins method are used to evaluate the 2σ confidence level with the proper coverage.

Chapter 7

Conclusions and Outlook

Five SK samples (FHC/RHC 1Rμ, FHC/RHC 1Re and FHC 1R ν_e CC1π^+) from 2009-2017 T2K data sets have been analysed together in a fit to four oscillation parameters of the PMNS matrix. Since the 2016 results were released, statistics almost doubled by data accumulation increase and selection efficiency increase. With a beam exposure of 1.47×10^{21} POT in neutrino mode and 0.76×10^{21} POT in antineutrino mode, 88 ν_e candidates and 7 $\overline{\nu}_e$ candidates were observed while expected number is 67.5 and 9 for $\delta_{CP} = 0$ in case of normal hierarchy. While we see a large upward fluctuation in the CC1π rate with 15 events observed and maximum prediction of 6.92 events, the p-value for upward or downward fluctuation in one sample is found to be 2.5%, and in at least 1 of 5 samples is 11.9%. Therefore what we observed could well be just a statistical fluctuation and would need more data to confirm.

The results of the joint oscillation fit are summarised in Table 7.1, where the uncertainties quoted represent the 1D 68% credible interval limits. The results using Feldman-Cousins method gives the δ_{CP} values of [-2.894,-0.561] and [-1.504,-1.265] with 2σ confidence level for normal hierarchy hypotheses inverted hierarchy hypotheses respectively. We see a first indication of CP conservation in neutrino sector excluded at 2σ level.

The T2K data weakly favours the normal hierarchy and the upper octant, a preference which becomes stronger with the addition of a reactor constraint on $\sin^2 2\theta_{13}$.

Table 7.1: Best fit and 68% credible interval uncertainties from the T2K- only and T2K+reactor data fits.

	$\|\Delta m^2_{32}\|(\times 10^{-3}\text{eV}^2)$	$\sin^2\theta_{23}$	$\sin^2\theta_{13}$	δ_{CP}
T2K-only	$2.458^{+0.058}_{-0.059}$	$0.511^{+0.036}_{-0.032}$	$0.0296^{+0.0066}_{-0.0052}$	$-1.72^{+1.04}_{-0.92}$
with reactor	$2.462^{+0.059}_{-0.057}$	$0.530^{+0.028}_{-0.034}$	0.0224 ± 0.0012	-1.64 ± 0.62

Several aspects for this analysis can be improved in the future for the reductions of background and systematic uncertainties. One of the dominant uncertainties in the analysis is from final state and secondary interactions at ND280. These uncertainties are currently included as cross-section systematic parameters at ND280, but included in the detector response systematic uncertainty at SK, and such treatment neglects correlations between the two detectors. Currently there are some studies to pion data at ND280 that could potentially help to reduce the uncertainty in the SK prediction due to these effects. This data can be added to the BANFF fit and the reduced FSI/SI uncertainties can be propagated to SK. Also, since the current event selection at ND280 accepts forwards-going tracks only, there are plans for improving the selection which will accept backwards-going and high-angle muon tracks, therefore providing a model-independent method to extrapolate expected spectra at SK.

With T2K continuing to collect more data, the understanding of systematic uncertainties are becoming more important. There has been ongoing effort of studying new ND280 detector configuration, with which we could get results on CP violation with better reliability. Initial studies with the new ND280 configuration using simulations shows systematic uncertainties can be significantly reduced. Together with the beamline upgrades and phase II data-taking, T2K could observe CP violation with sensitivity greater than 3σ with proposed 20×10^{21} POT. With analysis upgrades and future data accumulation, T2K will continue to make a strong contribution to the measurement of CP, and by combining atmospheric neutrino data and other long-baseline neutrino experiment measurements, accurate measurements of the 3-flavour neutrino oscillation parameters can be made. This also allows the 3-flavour oscillation model to be tested.

The next generation water Cherenkov detector called Hyper-Kamiokande (HK) [135] has been proposed which is planned to start operation in 2026. With an order of magnitude larger fiducial mass and higher performance photodetectors, it will provide much larger statistics for neutrino oscillation studies. Figure 7.1 shows the expected significance to exclude sin$\delta = 0$ (the CP conserved case) after 10 years of running. CP violation in the lepton sector can be observed with more than 3(5)σ significance for 78(62)% of the possible values of δ_{CP} . With T2K phase II and Hyper-Kamiokande experiment planned to run in the next decade, neutrino physics will continue to be one of the most exciting places to search for BSM physics.

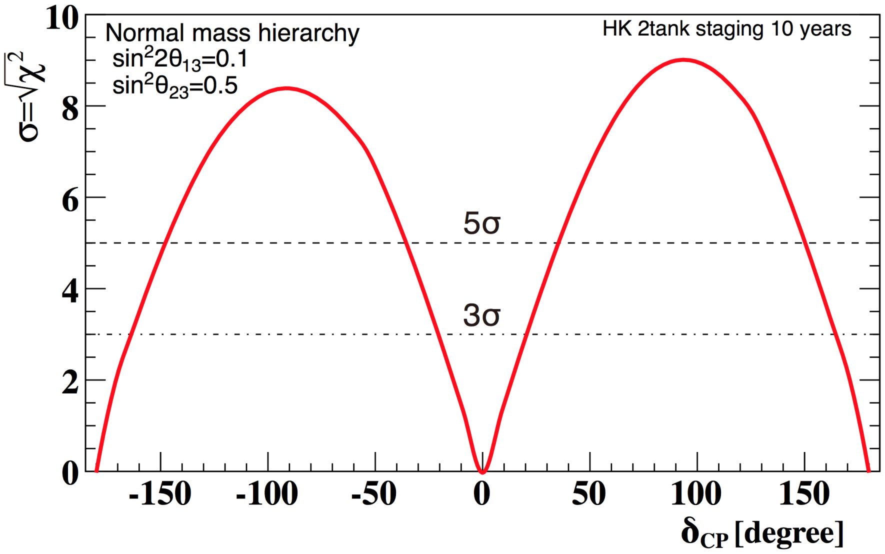

Figure 7.1: Expected significance to exclude sin$\delta = 0$ assuming normal hierarchy after 10 years of running HK. The sensitivity is estimated based on a framework developed in current T2K experiment with updated systematic uncertainty estimation.

Bibliography

[1] F. Capozzi, E. Lisi, A. Marrone et al., "Neutrino masses and mixings: Status of known and unknown 3ν parameters", *Nucl. Phys.* **B908** (2016) 218–234, `doi:10.1016/j.nuclphysb.2016.02.016`, `arXiv:1601.07777`.

[2] A. de Gouvea, "TASI lectures on neutrino physics", in *Physics in D ¿= 4. Proceedings, Theoretical Advanced Study Institute in elementary particle physics, TASI 2004, Boulder, USA, June 6-July 2, 2004*, pp. 197–258. 2004. `arXiv:hep-ph/0411274`.

[3] NOvA Collaboration, "First measurement of muon-neutrino disappearance in NOvA", *Phys. Rev.* **D93** (2016), no. 5, 051104, `doi:10.1103/PhysRevD.93.051104`, `arXiv:1601.05037`.

[4] MINOS Collaboration Collaboration, "Measurement of Neutrino and Antineutrino Oscillations Using Beam and Atmospheric Data in MINOS", *Phys. Rev. Lett.* **110** (Jun, 2013) 251801, `doi:10.1103/PhysRevLett.110.251801`.

[5] "Proceedings, 34th International Cosmic Ray Conference (ICRC 2015)", volume ICRC2015. (2015).

[6] M. G. Aartsen et al., "Neutrino oscillation studies with IceCube-DeepCore", *Nucl. Phys.* **B908** (2016) 161–177, `doi:10.1016/j.nuclphysb.2016.03.028`.

[7] T2K Collaboration, "Combined Analysis of Neutrino and Antineutrino Oscillations at T2K", *Phys. Rev. Lett.* **118** (2017), no. 15, 151801, `doi:10.1103/PhysRevLett.118.151801`, `arXiv:1701.00432`.

[8] NOvA Collaboration, "First measurement of electron neutrino appearance in NOvA", *Phys. Rev. Lett.* **116** (2016), no. 15, 151806, `doi:10.1103/PhysRevLett.116.151806`, `arXiv:1601.05022`.

[9] LSND Collaboration Collaboration, "Evidence for neutrino oscillations from the observation of $\overline{\nu}_e$ appearance in a $\overline{\nu}_\mu$ beam", *Phys. Rev. D* **64** (Nov, 2001) 112007, `doi:10.1103/PhysRevD.64.112007`.

[10] Particle Data Group Collaboration, "Review of Particle Physics", *Chin. Phys.* **C40** (2016), no. 10, 100001, `doi:10.1088/1674-1137/40/10/100001`.

[11] T. collaboration, "Expression of Interest for an Extended Run at T2K to 20×10^{21} POT". `http://www.t2k.org/docs/technotes/276`, 2017. [T2K collaboration].

[12] T2K Collaboration, "The T2K Experiment", *Nucl. Instrum. Meth.* **A659** (2011) 106–135, `doi:10.1016/j.nima.2011.06.067`, `arXiv:1106.1238`.

[13] M. F. *et al.*, "Flux Tuning and Uncertainty Updates for the 13a Flux". `http://www.t2k.org/docs/technotes/217`, 2015.

[14] "T2K neutrino flux prediction", *Phys. Rev. D* **87** (Jan, 2013) 012001, `doi:10.1103/PhysRevD.87.012001`.

[15] K. Abe, N. Abgrall, Y. Ajima et al., "Measurements of the T2K neutrino beam properties using the INGRID on-axis near detector", *Nuclear Instruments and Methods in Physics Research A* **694** (December, 2012) 211–223, `doi:10.1016/j.nima.2012.03.023`, `arXiv:1111.3119`.

[16] P.-A. A. et. al., "The T2K fine-grained detectors", *Nuclear Instruments and Methods in Physics Research Section A: Accelerators, Spectrometers, Detectors and Associated Equipment* **696** (2012) 1 – 31, `doi:https://doi.org/10.1016/j.nima.2012.08.020`.

[17] T2K Collaboration, Y. Itow et al., "The JHF-Kamioka neutrino project", in *Neutrino oscillations and their origin. Proceedings, 3rd International Workshop, NOON 2001,*

Kashiwa, Tokyo, Japan, December 508, 2001, pp. 239–248. 2001. `arXiv:hep-ex/0106019`.

[18] `http://www.ps.uci.edu/~tomba/sk/tscan/compare_mu_e/`. [Online; accessed 18-Feb-2017].

[19] J. A. Formaggio and G. P. Zeller, “From eV to EeV: Neutrino cross sections across energy scales”, *Rev. Mod. Phys.* **84** (Sep, 2012) 1307–1341, `doi:10.1103/RevModPhys.84.1307`.

[20] P. de Perio, “NEUT pion FSI”, *AIP Conf. Proc.* **1405** (2011) 223–228, `doi:10.1063/1.3661590`, `arXiv:1405.3973`.

[21] J. Chadwick, “The intensity distribution in the magnetic spectrum of beta particles from radium (B + C)”, *Verh. Phys. Gesell.* **16** (1914) 383–391.

[22] W. Pauli, “Dear radioactive ladies and gentlemen”, *Phys. Today* **31N9** (1978) 27.

[23] F. Reines and C. L. Cowan, “Detection of the Free Neutrino”, *Phys. Rev.* **92** (Nov, 1953) 830–831, `doi:10.1103/PhysRev.92.830`.

[24] G. Danby, J.-M. Gaillard, K. Goulianos et al., “Observation of High-Energy Neutrino Reactions and the Existence of Two Kinds of Neutrinos”, *Phys. Rev. Lett.* **9** (Jul, 1962) 36–44, `doi:10.1103/PhysRevLett.9.36`.

[25] DONUT Collaboration, “Observation of tau neutrino interactions”, *Phys. Lett.* **B504** (2001) 218–224, `doi:10.1016/S0370-2693(01)00307-0`, `arXiv:hep-ex/0012035`.

[26] Standard Model, “Standard Model — Wikipedia, The Free Encyclopedia”, 2017. [Online; accessed 25-September-2017].

[27] C. S. Wu, E. Ambler, R. W. Hayward et al., “Experimental Test of Parity Conservation in Beta Decay”, *Phys. Rev.* **105** (Feb, 1957) 1413–1415, `doi:10.1103/PhysRev.105.1413`.

[28] M. Goldhaber, L. Grodzins, and A. W. Sunyar, "Helicity of Neutrinos", *Phys. Rev.* **109** (Feb, 1958) 1015–1017, `doi:10.1103/PhysRev.109.1015`.

[29] T. D. Lee and C.-N. Yang, "Parity Nonconservation and a Two Component Theory of the Neutrino", *Phys. Rev.* **105** (1957) 1671–1675, `doi:10.1103/PhysRev.105.1671`. [,245(1957)].

[30] L. D. Landau, "On the conservation laws for weak interactions", *Nucl. Phys.* **3** (1957) 127–131, `doi:10.1016/0029-5582(57)90061-5`.

[31] A. Salam, "On parity conservation and neutrino mass", *Nuovo Cim.* **5** (1957) 299–301, `doi:10.1007/BF02812841`.

[32] S. Weinberg, "A Model of Leptons", *Phys. Rev. Lett.* **19** (1967) 1264–1266, `doi:10.1103/PhysRevLett.19.1264`.

[33] A. Salam, "Weak and Electromagnetic Interactions", *Conf. Proc.* **C680519** (1968) 367–377.

[34] B. Pontecorvo, "Mesonium and anti-mesonium", *Sov. Phys. JETP* **6** (1957) 429. [Zh. Eksp. Teor. Fiz.33,549(1957)].

[35] R. Davis, D. S. Harmer, and K. C. Hoffman, "Search for Neutrinos from the Sun", *Phys. Rev. Lett.* **20** (May, 1968) 1205–1209, `doi:10.1103/PhysRevLett.20.1205`.

[36] SNO Collaboration Collaboration, "Direct Evidence for Neutrino Flavor Transformation from Neutral-Current Interactions in the Sudbury Neutrino Observatory", *Phys. Rev. Lett.* **89** (Jun, 2002) 011301, `doi:10.1103/PhysRevLett.89.011301`.

[37] Kamiokande-II Collaboration, "Observation of a small atmospheric muon-neutrino / electron-neutrino ratio in Kamiokande", *Phys. Lett.* **B280** (1992) 146–152, `doi:10.1016/0370-2693(92)90788-6`.

[38] Super-Kamiokande Collaboration, "Evidence for oscillation of atmospheric neutrinos", *Phys. Rev. Lett.* **81** (1998) 1562–1567, `doi:10.1103/PhysRevLett.81.1562`, `arXiv:hep-ex/9807003`.

[39] Z. Maki, M. Nakagawa, and S. Sakata, “Remarks on the unified model of elementary particles”, *Prog.Theor.Phys.* **28** (1962) 870–880, `doi:10.1143/PTP.28.870`.

[40] N. Cabibbo, “Unitary Symmetry and Leptonic Decays”, *Phys. Rev. Lett.* **10** (Jun, 1963) 531–533, `doi:10.1103/PhysRevLett.10.531`.

[41] E. K. Akhmedov and A. Y. Smirnov, “Paradoxes of neutrino oscillations”, *Physics of Atomic Nuclei* **72** (Aug, 2009) 1363–1381, `doi:10.1134/S1063778809080122`.

[42] Daya Bay Collaboration, “Observation of electron-antineutrino disappearance at Daya Bay”, *Phys. Rev. Lett.* **108** (2012) 171803, `doi:10.1103/PhysRevLett.108.171803`, `arXiv:1203.1669`.

[43] T2K Collaboration, “Observation of Electron Neutrino Appearance in a Muon Neutrino Beam”, *Phys. Rev. Lett.* **112** (2014) 061802, `doi:10.1103/PhysRevLett.112.061802`, `arXiv:1311.4750`.

[44] S. P. Mikheev and A. Yu. Smirnov, “Resonance Amplification of Oscillations in Matter and Spectroscopy of Solar Neutrinos”, *Sov. J. Nucl. Phys.* **42** (1985) 913–917. [Yad. Fiz.42,1441(1985)].

[45] L. Wolfenstein, “Neutrino Oscillations in Matter”, *Phys. Rev.* **D17** (1978) 2369–2374, `doi:10.1103/PhysRevD.17.2369`.

[46] GALLEX Collaboration, “GALLEX solar neutrino observations: Results for GALLEX IV”, *Phys. Lett.* **B447** (1999) 127–133, `doi:10.1016/S0370-2693(98)01579-2`.

[47] SAGE Collaboration, “Measurement of the response of the Russian-American gallium experiment to neutrinos from a Cr-51 source”, *Phys. Rev.* **C59** (1999) 2246–2263, `doi:10.1103/PhysRevC.59.2246`, `arXiv:hep-ph/9803418`.

[48] Borexino Collaboration Collaboration, “Final results of Borexino Phase-I on low-energy solar neutrino spectroscopy”, *Phys. Rev. D* **89** (Jun, 2014) 112007, `doi:10.1103/PhysRevD.89.112007`.

[49] SNO Collaboration Collaboration, “Measurement of the ν_e and total ^{8}B solar neutrino fluxes with the Sudbury Neutrino Observatory phase-III data set”, *Phys. Rev. C* **87** (Jan, 2013) 015502, `doi:10.1103/PhysRevC.87.015502`.

[50] KamLAND Collaboration, “^{7}Be Solar Neutrino Measurement with KamLAND”, *Phys. Rev.* **C92** (2015), no. 5, 055808, `doi:10.1103/PhysRevC.92.055808`, `arXiv:1405.6190`.

[51] The MINOS Collaboration Collaboration, “Measurements of atmospheric neutrinos and antineutrinos in the MINOS far detector”, *Phys. Rev. D* **86** (Sep, 2012) 052007, `doi:10.1103/PhysRevD.86.052007`.

[52] MACRO Collaboration, “Measurement of the atmospheric neutrino induced upgoing muon flux using MACRO”, *Phys. Lett.* **B434** (1998) 451–457, `doi:10.1016/S0370-2693(98)00885-5`, `arXiv:hep-ex/9807005`.

[53] Soudan-2 Collaboration, “The Soudan-2 detector: The Design and construction of the tracking calorimeter modules”, *Nucl. Instrum. Meth.* **A376** (1996) 36–48, `doi:10.1016/0168-9002(96)00271-9`.

[54] J. A. B. Coelho, W. A. Mann, and S. S. Bashar, “Nonmaximal θ_{23} mixing at NOvA from neutrino decoherence”, *Phys. Rev. Lett.* **118** (2017), no. 22, 221801, `doi:10.1103/PhysRevLett.118.221801`, `arXiv:1702.04738`.

[55] T. Lasserre, G. Mention, M. Cribier et al., “Comment on Phys. Rev. Lett. 108, 191802 (2012): ’Observation of Reactor Electron Antineutrino Disappearance in the RENO Experiment’”, `arXiv:1205.5626`.

[56] Double Chooz Collaboration, “Reactor electron antineutrino disappearance in the Double Chooz experiment”, *Phys. Rev.* **D86** (2012) 052008, `doi:10.1103/PhysRevD.86.052008`, `arXiv:1207.6632`.

[57] MiniBooNE Collaboration, “Event Excess in the MiniBooNE Search for $\bar{\nu}_\mu \to \bar{\nu}_e$ Oscillations”, *Phys. Rev. Lett.* **105** (2010) 181801, `doi:10.1103/PhysRevLett.105.181801`, `arXiv:1007.1150`.

[58] KARMEN Collaboration Collaboration, “Upper limits for neutrino oscillations $\overline{\nu}_\mu \to \overline{\nu}_e$ from muon decay at rest”, *Phys. Rev. D* **65** (Jun, 2002) 112001, `doi:10.1103/PhysRevD.65.112001`.

[59] NOMAD Collaboration, “Search for nu(mu) —¿ nu(e) oscillations in the NOMAD experiment”, *Phys. Lett.* **B570** (2003) 19–31, `doi:10.1016/j.physletb.2003.07.029`, `arXiv:hep-ex/0306037`.

[60] T. A. Mueller, D. Lhuillier, M. Fallot et al., “Improved predictions of reactor antineutrino spectra”, *Phys. Rev. C* **83** (May, 2011) 054615, `doi:10.1103/PhysRevC.83.054615`.

[61] Daya Bay Collaboration Collaboration, “Search for a Light Sterile Neutrino at Daya Bay”, *Phys. Rev. Lett.* **113** (Oct, 2014) 141802, `doi:10.1103/PhysRevLett.113.141802`.

[62] K. Eitel, “Direct Neutrino Mass Experiments”, *Nuclear Physics B - Proceedings Supplements* **143** (2005), no. Supplement C, 197 – 204, `doi:https://doi.org/10.1016/j.nuclphysbps.2005.01.105`. NEUTRINO 2004.

[63] Planck Collaboration, “Planck 2015 results. XIII. Cosmological parameters”, *Astron. Astrophys.* **594** (2016) A13, `doi:10.1051/0004-6361/201525830`, `arXiv:1502.01589`.

[64] J. Suhonen and O. Civitarese, “Weak-interaction and nuclear-structure aspects of nuclear double beta decay”, *Physics Reports* **300** (1998), no. 3, 123 – 214, `doi:http://dx.doi.org/10.1016/S0370-1573(97)00087-2`.

[65] SNO+ Collaboration, “Current Status and Future Prospects of the SNO+ Experiment”, *Adv. High Energy Phys.* **2016** (2016) 6194250, `doi:10.1155/2016/6194250`, `arXiv:1508.05759`.

[66] KamLAND-Zen Collaboration, “Search for Majorana Neutrinos near the Inverted Mass Hierarchy Region with KamLAND-Zen”, *Phys. Rev. Lett.* **117** (2016), no. 8, 082503,

doi:10.1103/PhysRevLett.117.109903,10.1103/PhysRevLett.117.082503, arXiv:1605.02889. [Addendum: Phys. Rev. Lett.117,no.10,109903(2016)].

[67] GERDA Collaboration, G. Benato, "Search of Neutrinoless Double Beta Decay with the GERDA Experiment", in *Proceedings, 12th Conference on the Intersections of Particle and Nuclear Physics (CIPANP 2015): Vail, Colorado, USA, May 19-24, 2015.* 2015. arXiv:1509.07792.

[68] *MAJORANA* Collaboration, "The *MAJORANA DEMONSTRATOR*: A Search for Neutrinoless Double-beta Decay of ^{76}Ge", *J. Phys. Conf. Ser.* **606** (2015), no. 1, 012004, doi:10.1088/1742-6596/606/1/012004, arXiv:1501.03089.

[69] LEGEND Collaboration, "The Large Enriched Germanium Experiment for Neutrinoless Double Beta Decay (LEGEND)", *AIP Conf. Proc.* **1894** (2017), no. 1, 020027, doi:10.1063/1.5007652, arXiv:1709.01980.

[70] M. Agostini et al., "Background free search for neutrinoless double beta decay with GERDA Phase II", doi:10.1038/nature21717, arXiv:1703.00570. [Nature544,47(2017)].

[71] A. D. Sakharov, "Violation of CP Invariance, c Asymmetry, and Baryon Asymmetry of the Universe", *Pisma Zh. Eksp. Teor. Fiz.* **5** (1967) 32–35, doi:10.1070/PU1991v034n05ABEH002497. [Usp. Fiz. Nauk161,61(1991)].

[72] Y. Nir, "Introduction to leptogenesis", in *6th Rencontres du Vietnam: Challenges in Particle Astrophysics Hanoi, Vietnam, August 6-12, 2006.* 2007. arXiv:hep-ph/0702199.

[73] S. Pascoli, S. T. Petcov, and A. Riotto, "Leptogenesis and Low Energy CP Violation in Neutrino Physics", *Nucl. Phys.* **B774** (2007) 1–52, doi:10.1016/j.nuclphysb.2007.02.019, arXiv:hep-ph/0611338.

[74] M. Fukugita and T. Yanagida, "Baryogenesis Without Grand Unification", *Phys. Lett.* **B174** (1986) 45–47, doi:10.1016/0370-2693(86)91126-3.

[75] DUNE Collaboration, J. Martn-Albo, “Sensitivity of DUNE to long-baseline neutrino oscillation physics”, in *2017 European Physical Society Conference on High Energy Physics (EPS-HEP 2017) Venice, Italy, July 5-12, 2017*. 2017. `arXiv:1710.08964`.

[76] S. van der Meer, “A directive device for charged particles and its use in an enhanced neutrino beam”. CERN Yellow Reports: Monographs. CERN, Geneva, 1961.

[77] CERN, “”. CERN, Geneva, (1965).

[78] D. Beavis, A. Carroll, and I. Chiang, “Long baseline neutrino oscillation experiment at the AGS”, technical report, (April, 1995).

[79] T2K UK Collaboration, “The Electromagnetic Calorimeter for the T2K Near Detector ND280”, *JINST* **8** (2013) P10019, `doi:10.1088/1748-0221/8/10/P10019`, `arXiv:1308.3445`.

[80] Super-Kamiokande Collaboration, “The Super-Kamiokande detector”, *Nucl. Instrum. Meth.* **A501** (2003) 418–462, `doi:10.1016/S0168-9002(03)00425-X`.

[81] NA61/SHINE Collaboration, “Measurement of Production Properties of Positively Charged Kaons in Proton-Carbon Interactions at 31 GeV/c”, *Phys. Rev.* **C85** (2012) 035210, `doi:10.1103/PhysRevC.85.035210`, `arXiv:1112.0150`.

[82] A. Ferrari, P. R. Sala, A. Fasso et al., “FLUKA: A multi-particle transport code (Program version 2005)”,.

[83] R. Brun, F. Bruyant, M. Maire et al., “GEANT3”,.

[84] C. Zeitnitz and T. A. Gabriel, “The GEANT - CALOR interface and benchmark calculations of ZEUS test calorimeters”, *Nucl. Instrum. Meth.* **A349** (1994) 106–111, `doi:10.1016/0168-9002(94)90613-0`.

[85] Y. Hayato, “A neutrino interaction simulation program library NEUT”, *Acta Phys. Polon.* **B40** (2009) 2477–2489.

[86] GEANT4 Collaboration, "GEANT4: A Simulation toolkit", *Nucl. Instrum. Meth.* **A506** (2003) 250–303, `doi:10.1016/S0168-9002(03)01368-8`.

[87] C. Andreopoulos, C. Barry, S. Dytman et al., "The GENIE Neutrino Monte Carlo Generator: Physics and User Manual", `arXiv:1510.05494`.

[88] T. Golan, C. Juszczak, and J. T. Sobczyk, "Final State Interactions Effects in Neutrino-Nucleus Interactions", *Phys. Rev.* **C86** (2012) 015505, `doi:10.1103/PhysRevC.86.015505`, `arXiv:1202.4197`.

[89] C. H. Llewellyn Smith, "Neutrino Reactions at Accelerator Energies", *Phys. Rept.* **3** (1972) 261–379, `doi:10.1016/0370-1573(72)90010-5`.

[90] O. Benhar and A. Fabrocini, "Two-nucleon spectral function in infinite nuclear matter", *Phys. Rev. C* **62** (Aug, 2000) 034304, `doi:10.1103/PhysRevC.62.034304`.

[91] R. Smith and E. Moniz, "Neutrino reactions on nuclear targets", *Nuclear Physics B* **43** (1972), no. Supplement C, 605 – 622, `doi:https://doi.org/10.1016/0550-3213(72)90040-5`.

[92] J. Nieves, I. R. Simo, and M. J. V. Vacas, "Inclusive charged-current neutrino-nucleus reactions", *Phys. Rev. C* **83** (Apr, 2011) 045501, `doi:10.1103/PhysRevC.83.045501`.

[93] C. Wilkinson et al., "Testing charged current quasi-elastic and multinucleon interaction models in the NEUT neutrino interaction generator with published datasets from the MiniBooNE and MINERA experiments", *Phys. Rev.* **D93** (2016), no. 7, 072010, `doi:10.1103/PhysRevD.93.072010`, `arXiv:1601.05592`.

[94] D. Rein and L. M. Sehgal, "Neutrino Excitation of Baryon Resonances and Single Pion Production", *Annals Phys.* **133** (1981) 79–153, `doi:10.1016/0003-4916(81)90242-6`.

[95] K. M. Graczyk and J. T. Sobczyk, "Form factors in the quark resonance model", *Phys. Rev. D* **77** (Mar, 2008) 053001, `doi:10.1103/PhysRevD.77.053001`.

[96] C. Wilkinson, P. Rodrigues, S. Cartwright et al., “Reanalysis of bubble chamber measurements of muon-neutrino induced single pion production”, *Phys. Rev.* **D90** (2014), no. 11, 112017, `doi:10.1103/PhysRevD.90.112017`, `arXiv:1411.4482`.

[97] D. Rein and L. M. Sehgal, “Coherent pi0 Production in Neutrino Reactions”, *Nucl. Phys.* **B223** (1983) 29–44, `doi:10.1016/0550-3213(83)90090-1`.

[98] M. Glck, E. Reya, and A. Vogt, “Dynamical parton distributions revisited”, *Eur. Phys. J.* **C5** (1998) 461–470, `doi:10.1007/s100529800978,10.1007/s100520050289`, `arXiv:hep-ph/9806404`.

[99] A. Bodek and U. K. Yang, “Modeling neutrino and electron scattering inelastic cross-sections in the few GeV region with effective LO PDFs TV Leading Order”, in *2nd International Workshop on Neutrino-Nucleus Interactions in the Few GeV Region (NuInt 02) Irvine, California, December 12-15, 2002.* 2003. `arXiv:hep-ex/0308007`.

[100] R. D. Woods and D. S. Saxon, “Diffuse Surface Optical Model for Nucleon-Nuclei Scattering”, *Phys. Rev.* **95** (1954) 577–578, `doi:10.1103/PhysRev.95.577`.

[101] C. D. Jager, H. D. Vries, and C. D. Vries, “Nuclear charge- and magnetization-density-distribution parameters from elastic electron scattering”, *Atomic Data and Nuclear Data Tables* **14** (1974), no. 5, 479 – 508, `doi:http://dx.doi.org/10.1016/S0092-640X(74)80002-1`. Nuclear Charge and Moment Distributions.

[102] E. Oset, L. L. Salcedo, and D. Strottman, “A Theoretical Approach to Pion Nuclear Reactions in the Resonance Region”, *Phys. Lett.* **165B** (1985) 13–18, `doi:10.1016/0370-2693(85)90681-1`.

[103] H. W. Bertini, “Nonelastic Interactions of Nucleons and π Mesons with Complex Nuclei at Energies Below 3 GeV”, *Phys. Rev. C* **6** (Aug, 1972) 631–659, `doi:10.1103/PhysRevC.6.631`.

[104] R. Carlson, “Proton-Nucleus Total Reaction Cross Sections and Total Cross Sections Up to 1 GeV”, *Atomic Data and Nuclear Data Tables* **63** (1996), no. 1, 93 – 116, `doi:http://dx.doi.org/10.1006/adnd.1996.0010`.

[105] B. D. Wilkins and G. Igo, “10-MeV Proton Reaction Cross Sections for Several Elements”, *Phys. Rev.* **129** (Mar, 1963) 2198–2206, `doi:10.1103/PhysRev.129.2198`.

[106] J. F. Dicello and G. Igo, “Proton Total Reaction Cross Sections in the 10-20-MeV Range: Calcium-40 and Carbon-12”, *Phys. Rev. C* **2** (Aug, 1970) 488–499, `doi:10.1103/PhysRevC.2.488`.

[107] M. Q. Makino, C. N. Waddell, and R. M. Eisberg, “Proton total reaction cross sections of carbon from 16 to 28 MeV”, *Nuclear Physics* **68** (1965), no. 2, 378 – 386, `doi:http://dx.doi.org/10.1016/0029-5582(65)90654-1`.

[108] I. Šlaus, D. J. Margaziotis, R. F. Carlson et al., “Structure in the energy dependence of the proton total reaction cross section for C and Si in the energy region 20-40 MeV”, *Phys. Rev. C* **12** (Sep, 1975) 1093–1095, `doi:10.1103/PhysRevC.12.1093`.

[109] W. F. McGill, R. F. Carlson, T. H. Short et al., “Measurements of the proton total reaction cross section for light nuclei between 20 and 48 MeV”, *Phys. Rev. C* **10** (Dec, 1974) 2237–2246, `doi:10.1103/PhysRevC.10.2237`.

[110] P. U. Renberg, D. F. Measday, M. Pepin et al., “Reaction cross-sections for protons in the energy range 220-570 mev”, *Nucl. Phys.* **A183** (1972) 81–104, `doi:10.1016/0375-9474(72)90932-3`.

[111] G. P. Millburn, W. Birnbaum, W. E. Crandall et al., “Nuclear Radii from Inelastic Cross-Section Measurements”, *Phys. Rev.* **95** (Sep, 1954) 1268–1278, `doi:10.1103/PhysRev.95.1268`.

[112] R. Goloskie and K. Strauch, “Measurement of proton inelastic cross sections between 77 MeV and 133 MeV”, *Nuclear Physics* **29** (1962) 474 – 485, `doi:http://dx.doi.org/10.1016/0029-5582(62)90197-9`.

[113] F. F. Chen, C. P. Leavitt, and A. M. Shapiro, “Attenuation Cross Sections for 860-Mev Protons”, *Phys. Rev.* **99** (Aug, 1955) 857–871, `doi:10.1103/PhysRev.99.857`.

[114] “Inelastic p cross section on C”. `http://geant4.web.cern.ch/geant4/results/validation_plots/cross_sections/hadronic/inelastic/test1/inelastic.shtml`. [Online; accessed 20-July-2017].

[115] V. S. Barashenkov, A. S. Il’inov, N. M. Sobolevski et al., “Interaction of particles and nuclei of high and ultrahigh energy with nuclei”, *Soviet Physics Uspekhi* **16** (1973), no. 1, 31.

[116] P. B. *et al.*, “ν_μ CC Event Selections in the ND280 Tracker Using Run 2+3+4 Data”. `http://www.t2k.org/docs/technotes/212`, 2015.

[117] V. B. *et al.*, “CC $\overline{\nu}_\mu$ Event Selection in the ND280 Tracker Using Run 5c Anti-Neutrino Beam Data”. `http://www.t2k.org/docs/technotes/224`, 2015.

[118] V. B. *et al.*, “ND280 Tracker Analysis of ν_μ Contamination In AntiNu Beam in Run5c Data”. `http://www.t2k.org/docs/technotes/227`, 2015.

[119] V. B. *et al.*, “CC $\overline{\nu}_\mu$ Event Selection in the ND280 Tracker Using Run 5c and Run 6 Anti-Neutrino Beam Data”. `http://www.t2k.org/docs/technotes/246`, 2015.

[120] V. B. *et al.*, “CC ν_μ Background Event Selection in the ND280 Tracker Using Run 5c+Run 6 Anti-Neutrino Beam Data”. `http://www.t2k.org/docs/technotes/248`, 2015.

[121] K. M. M. S. M. Hartz, A. Kaboth and C. Wret, “ND280 Analysis (BANFF) for 2017 Oscillation Analyses”. `http://www.t2k.org/docs/technotes/324`, 2017.

[122] S. Tobayama, “An Analysis of the Oscillation of Atmospheric Neutrinos”. PhD thesis, THE UNIVERSITY OF BRITISH COLUMBIA, 2016.

[123] VaLOR group, “VALOR Run 1-8 Joint Analysis”. `http://www.t2k.org/docs/technotes/327`, 2017.

[124] MaCh3 group, "MaCh3 Run 1-8 Joint Analysis". `http://www.t2k.org/docs/technotes/320`, 2017.

[125] E. t. Wang, "Photon emission in neutral current interactions at the T2K experiment", *Phys. Rev. D* **92** (Sep, 2015) 053005, `doi:10.1103/PhysRevD.92.053005`.

[126] C. Berger and L. M. Sehgal, "Partially conserved axial vector current and coherent pion production by low energy neutrinos", *Phys. Rev. D* **79** (Mar, 2009) 053003, `doi:10.1103/PhysRevD.79.053003`.

[127] R. Wendell. http://www.phy.duke.edu/ raw22/public/Prob3++/.

[128] W. H. Press, S. A. Teukolsky, W. T. Vetterling et al., "Numerical Recipes 3rd Edition: The Art of Scientific Computing". Cambridge University Press, New York, NY, USA, 3 edition, 2007.

[129] C. B. *et al.*, "Markov Chain Monte Carlo framework for electron neutrino appearance analysis using electron angle and momentum information". `http://www.t2k.org/docs/technotes/137`, 2013.

[130] G. Feldman and R. Cousins, "A Unified Approach to the Classical Statistical Analysis of Small Signals". Phys.Rev.D57:3873-3889, 1998.

[131] M. Day and K. S. McFarland, "Differences in Quasi-Elastic Cross-Sections of Muon and Electron Neutrinos", *Phys. Rev.* **D86** (2012) 053003, `doi:10.1103/PhysRevD.86.053003`, `arXiv:1206.6745`.

[132] G. Cowan, K. Cranmer, E. Gross et al., "Asymptotic formulae for likelihood-based tests of new physics", *Eur. Phys. J.* **C71** (2011) 1554, `doi:10.1140/epjc/s10052-011-1554-0,10.1140/epjc/s10052-013-2501-z`, `arXiv:1007.1727`. [Erratum: Eur. Phys. J.C73,2501(2013)].

[133] R. A. *et al.*, "Super-Kamiokande Events and Data Quality Studies for T2K Runs 1-8". `http://www.t2k.org/docs/technotes/317`, 2017.

[134] H. Jeffreys, "Theory of Probability". Oxford, Oxford, England, third edition, 1961.

[135] Hyper-Kamiokande Proto Collaboration, M. Yokoyama, “The Hyper-Kamiokande Experiment”, in *Proceedings, Prospects in Neutrino Physics (NuPhys2016): London, UK, December 12-14, 2016*. 2017. `arXiv:1705.00306`.

Appendix A

Validations with other oscillation analysis groups

The behaviour of the fitting framework was checked by comparing the total number of events in each sample, the effect of each systematic error and the sensitivity contours between the three oscillation analysis groups (P-theta, VaLOR [123] and MaCh3 [124]).

A.1 Reference event rates using oscillation parameter Set B

Expected event rates with with Run 1-8 POT are shown in Tables A.1-A.5. These numbers assumes the oscillation parameters Set B listed in Table 6.1.

Table A.1: Event rate table for 1Rμ, SKMC 14a with tuned RUN1-8 FHC flux 13av2 and with BANFF/NIWG postfit reweight, 1.47×10^{21} POT.

Event Type	$\nu_\mu \rightarrow \nu_\mu$	$\nu_e \rightarrow \nu_e$	$\bar{\nu}_\mu \rightarrow \bar{\nu}_\mu$	$\bar{\nu}_e \rightarrow \bar{\nu}_e$	$\nu_\mu \rightarrow \nu_e$	$\bar{\nu}_\mu \rightarrow \bar{\nu}_e$	Total
CCQE	186.417	0.004	11.153	0.000	0.015	0.000	197.589
CCMEC	36.705	0.002	1.420	0.000	0.017	0.000	38.144
CC 1π	28.202	0.002	2.628	0.000	0.017	0.000	30.849
CC coh.	0.294	0.000	0.093	0.000	0.000	0.000	0.387
CC other	5.478	0.001	0.407	0.000	0.000	0.000	5.886
NC 1π	5.523	0.116	0.197	0.011	-	-	5.847
NC coh.	0.000	0.000	0.000	0.000	-	-	0.000
NC 1γ	0.000	0.000	0.000	0.000	-	-	0.000
NC other	2.056	0.074	0.131	0.009	-	-	2.270
Subtotal	264.675	0.199	16.028	0.021	0.049	0.000	
Total	280.971						

Table A.2: Event rate table for 1Re, SKMC 14a with tuned RUN1-8 FHC flux 13av2 and with BANFF/NIWG postfit reweight, 1.47×10^{21} POT.

Event Type	$\nu_\mu \rightarrow \nu_\mu$	$\nu_e \rightarrow \nu_e$	$\bar{\nu}_\mu \rightarrow \bar{\nu}_\mu$	$\bar{\nu}_e \rightarrow \bar{\nu}_e$	$\nu_\mu \rightarrow \nu_e$	$\bar{\nu}_\mu \rightarrow \bar{\nu}_e$	Total
CCQE	0.172	6.306	0.006	0.255	31.226	0.339	38.305
CCMEC	0.031	1.597	0.001	0.043	6.083	0.046	7.802
CC 1π	0.048	0.932	0.003	0.067	3.284	0.056	4.390
CC coh.	0.000	0.008	0.000	0.004	0.025	0.004	0.042
CC other	0.013	0.128	0.000	0.009	0.075	0.004	0.230
NC 1π	1.870	0.042	0.070	0.004	-	-	1.987
NC coh.	0.528	0.007	0.048	0.003	-	-	0.586
NC 1γ	0.942	0.017	0.050	0.002	-	-	1.011
NC other	0.318	0.017	0.021	0.001	-	-	0.357
Subtotal	3.924	9.054	0.200	0.390	40.694	0.448	
Total	54.709						

Table A.3: Event rate table for 1Rμ, SKMC 14a with tuned RUN5c-7b RHC flux 13av2 and with BANFF/NIWG postfit reweight, 0.76×10^{21} POT.

Event Type	$\nu_\mu \to \nu_\mu$	$\nu_e \to \nu_e$	$\bar{\nu_\mu} \to \bar{\nu_\mu}$	$\bar{\nu_e} \to \bar{\nu_e}$	$\nu_\mu \to \nu_e$	$\bar{\nu_\mu} \to \bar{\nu_e}$	Total
CCQE	15.541	0.001	31.141	0.001	0.001	0.002	46.686
CCMEC	4.510	0.000	2.928	0.000	0.000	0.000	7.439
CC 1π	3.976	0.000	4.600	0.000	0.000	0.001	8.578
CC coh.	0.047	0.000	0.182	0.000	0.000	0.000	0.230
CC other	0.944	0.000	0.607	0.000	0.000	0.000	1.551
NC 1π	0.420	0.017	0.522	0.014	-	-	0.973
NC coh.	0.000	0.000	0.002	0.000	-	-	0.002
NC 1γ	0.000	0.000	0.000	0.000	-	-	0.000
NC other	0.316	0.016	0.201	0.008	-	-	0.541
Subtotal	25.753	0.035	40.183	0.023	0.001	0.003	
Total	65.999						

Table A.4: Event rate table for 1Re, SKMC 14a with tuned RUN5c-7b RHC flux 13av2 and with BANFF/NIWG postfit reweight, 0.76×10^{21} POT.

Event Type	$\nu_\mu \to \nu_\mu$	$\nu_e \to \nu_e$	$\bar{\nu_\mu} \to \bar{\nu_\mu}$	$\bar{\nu_e} \to \bar{\nu_e}$	$\nu_\mu \to \nu_e$	$\bar{\nu_\mu} \to \bar{\nu_e}$	Total
CCQE	0.013	0.509	0.025	0.848	0.725	3.396	5.517
CCMEC	0.003	0.144	0.002	0.113	0.175	0.391	0.828
CC 1π	0.008	0.101	0.007	0.144	0.113	0.396	0.770
CC coh.	0.000	0.001	0.000	0.011	0.001	0.037	0.050
CC other	0.004	0.021	0.001	0.012	0.009	0.008	0.055
NC 1π	0.163	0.007	0.196	0.005	-	-	0.372
NC coh.	0.048	0.002	0.203	0.003	-	-	0.256
NC 1γ	0.079	0.004	0.175	0.004	-	-	0.263
NC other	0.057	0.002	0.027	0.001	-	-	0.087
Subtotal	0.375	0.792	0.637	1.141	1.024	4.227	
Total	8.197						

Table A.5: Event rate table for 1R ν_e CC1π^+, SKMC 14a with tuned RUN1-8 FHC flux 13av2 and with BANFF/NIWG postfit reweight, 1.47×10^{21} POT.

Event Type	$\nu_\mu \to \nu_\mu$	$\nu_e \to \nu_e$	$\bar{\nu_\mu} \to \bar{\nu_\mu}$	$\bar{\nu_e} \to \bar{\nu_e}$	$\nu_\mu \to \nu_e$	$\bar{\nu_\mu} \to \bar{\nu_e}$	Total
CCQE	0.033	0.024	0.001	0.002	0.146	0.003	0.210
CCMEC	0.011	0.022	0.001	0.001	0.117	0.001	0.152
CC 1π	0.081	0.761	0.003	0.004	3.477	0.003	4.328
CC coh.	0.000	0.018	0.000	0.000	0.076	0.000	0.095
CC other	0.039	0.112	0.001	0.003	0.098	0.002	0.255
NC 1π	0.085	0.002	0.005	0.000	-	-	0.093
NC coh.	0.000	0.000	0.000	0.000	-	-	0.000
NC 1γ	0.028	0.000	0.001	0.000	-	-	0.029
NC other	0.206	0.008	0.013	0.001	-	-	0.228
Subtotal	0.485	0.948	0.024	0.011	3.914	0.009	
Total				5.3899			

A.2 Systematic Variation Comparisons

To ensure that each systematic parameters are implemented correctly in each of the fitting code, we compare E_{rec} spectra for each event sample by varying ± 1 and 3 sigma of each of the parameters one at a time (see Figure A.1 to A.3 for examples).

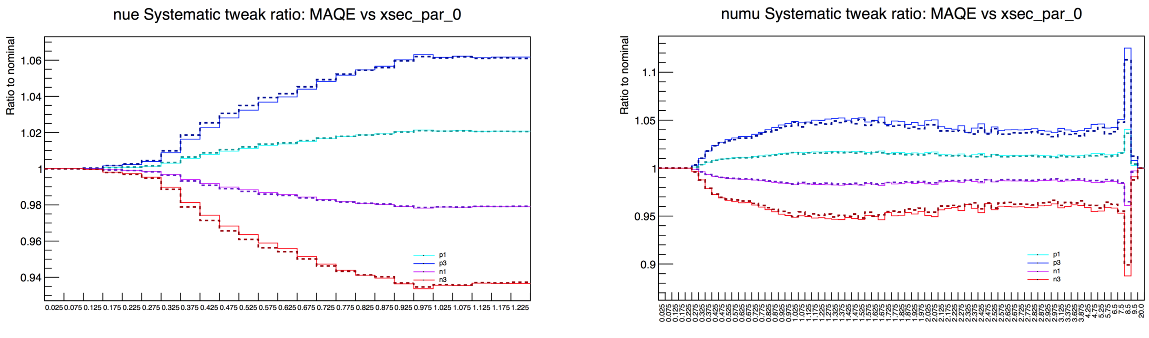

(a) 1Re

(b) 1Rμ

Figure A.1: Varying ± 1 and 3 sigma of M_A^{QE} have on E_{rec} spectra of 1Re and 1Rμ-like events. Dash line represents MaCh3 and solid line represents P-theta.

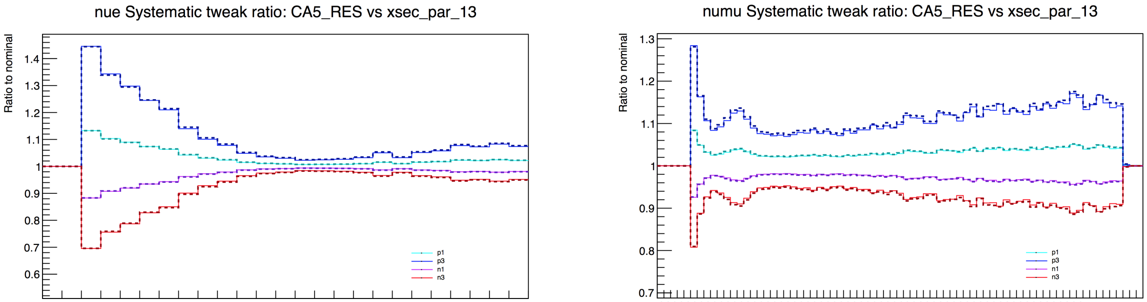

(a) 1Re (b) 1Rμ

Figure A.2: Varying ± 1 and 3 sigma of C_A^{RES} have on E_{rec} spectra of 1Re and 1Rμ-like events. Dash line represents MaCh3 and solid line represents P-theta.

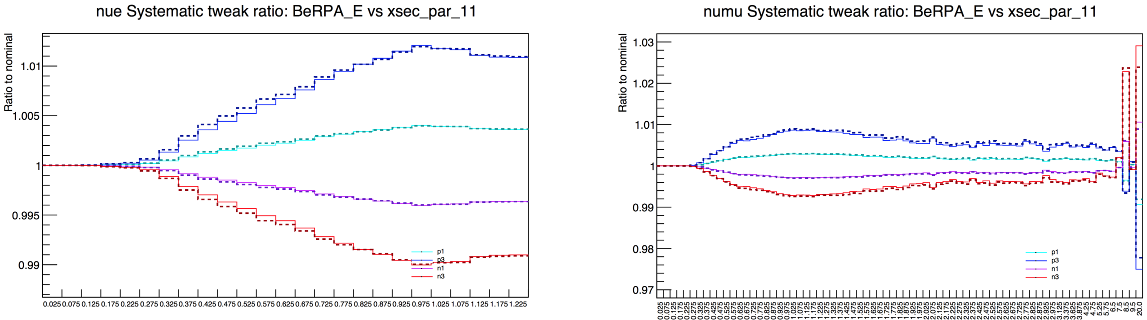

(a) 1Re (b) 1Rμ

Figure A.3: Varying ± 1 and 3 sigma of BeRPA E have on E_{rec} spectra of 1Re and 1Rμ-like events. Dash line represents MaCh3 and solid line represents P-theta.

A.3 Comparisons of data fit between different oscillation analysis groups

Data fit contours are compared among the other two independent analysis groups. Figures A.4 to A.6 show the comparisons of data fit contours with reactor constraint. The contours seem to agree well amongst the three analyses. The disagreements seen in the 1D δ_{CP} contours are due to the fact that confidence intervals in MaCh3 are constructed by obtaining an estimate of the likelihood involving the inverse of the posterior probability in each bin of the histogram (see [124] for details).

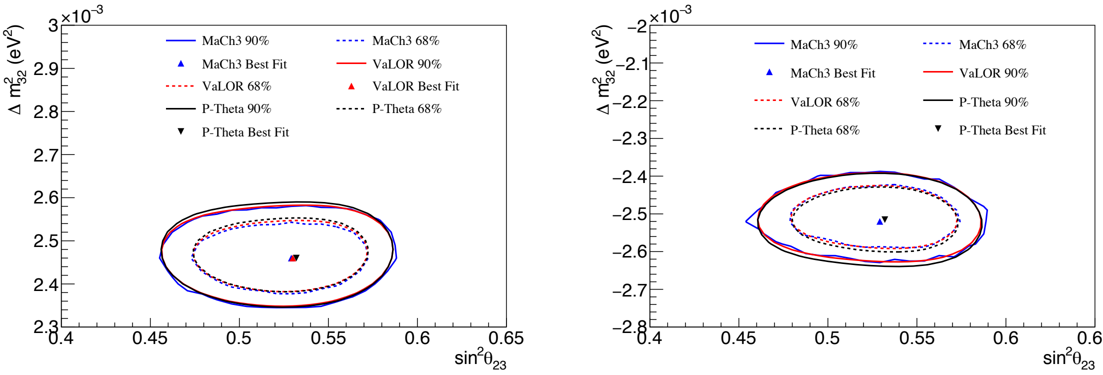

(a) NH

(b) IH

Figure A.4: Comparison of 2D confidence level contours in $|\Delta m^2_{32}|$ vs. $\sin^2\theta_{23}$ for normal and inverted hierarchy to VaLOR and MaCh3. These results are presented with local contours for each hierarchy hypothesis.

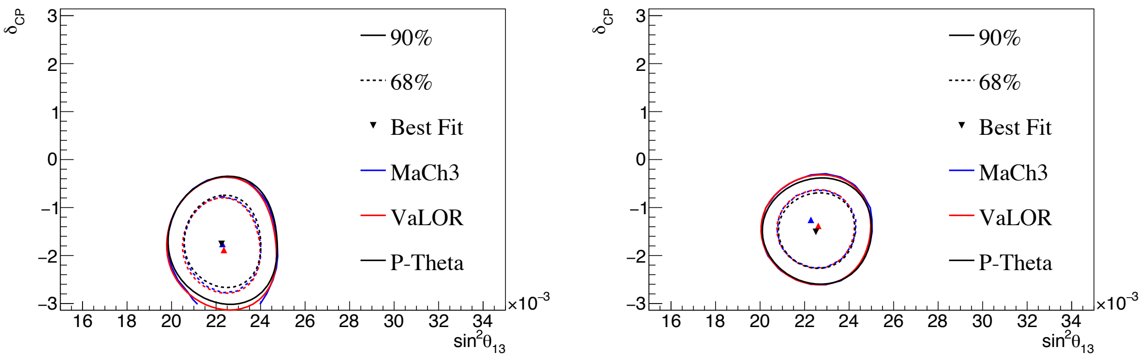

(a) NH

(b) IH

Figure A.5: Comparison of 2D confidence level contours in δ_{CP} vs. $\sin^2\theta_{13}$ for normal and inverted hierarchy to VaLOR and MaCh3. These results are presented with local contours for each hierarchy hypothesis.

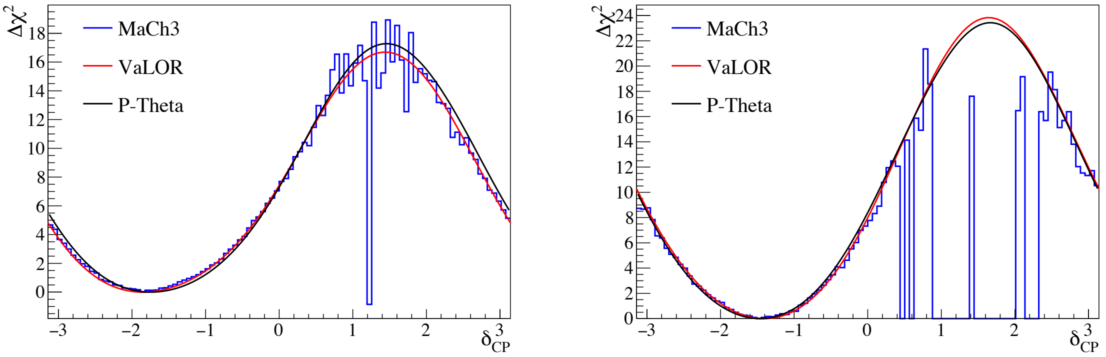

(a) NH

(b) IH

Figure A.6: Comparison of 1D $\Delta\chi^2$ of δ_{CP} to VaLOR and MaCh3.

A.4 Effect of the number of throws used for marginalisation

As stated in section 6.3.2 , we use 10k throws of the nuisance parameters to numerically integrate the likelihood over the nuisance parameters and construct the distribution of the marginal likelihood as a function of the parameters of interest. Previously, all fits were performed using 10k throws but it was found that this number of throws is insufficient to properly sample the tails of oscillation parameters (in particular $\sin^2 2\theta_{13}$ when performing 1D fits) given the significant increase in sensitivity compare to previous analyses. As a result, each separate 1D fits result in different distributions of marginal likelihood (and hence the contours). This is demonstrated in figure A.7.

To check whether the number of throws is sufficient, we perform several fits on Asimov data set A using different sets of throws and check for convergence. Figure A.8 shows the result of the 1D δ_{CP} fits using 40k and 80k throws respectively. It was found that 80k throws is sufficient enough to obtain a good stability of the fits.

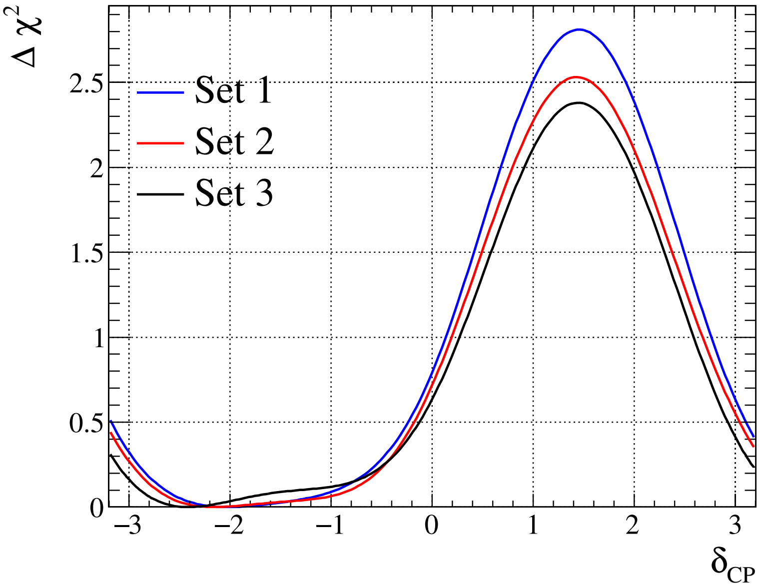

Figure A.7: Asimov A sensitivity of 1D δ_{CP} contours using different sets of 10k throws.

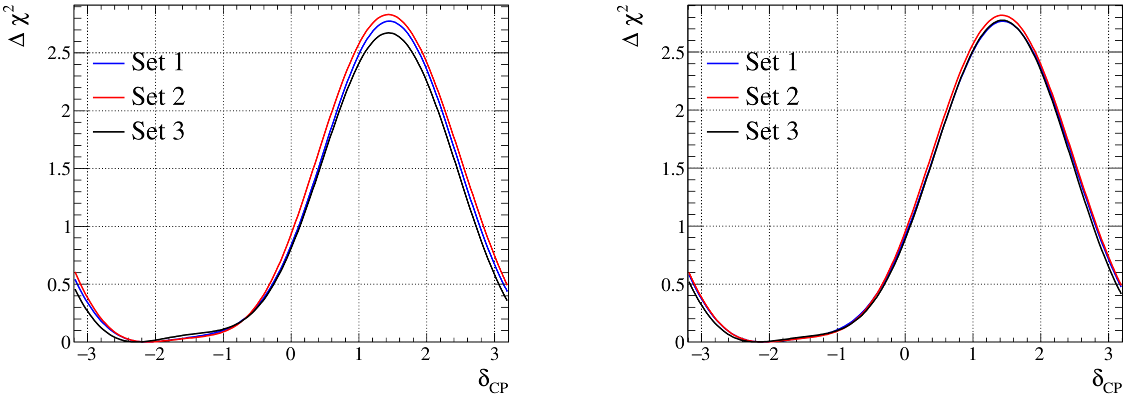

(a) 40k throws

(b) 80k throws

Figure A.8: Asimov A sensitivity of 1D δ_{CP} contours using different sets of throws.

A.5 Effect of the systematic parameters for each sample

Tables A.6-A.10 describe the effect of systematic uncertainties for each of the sample. These numbers assumes the oscillation parameters Set A listed in Table 6.1.

Table A.6: ν_e 1R

	Pre-BANFF			Post-BANFF		
Sample	mean	1σ	%	mean	1σ	%
SK Detector	64.77	2.00	3.1	74.78	2.25	3.0
SK FSI+SI+PN	64.43	1.83	2.8	74.47	2.16	2.9
SK Detector+FSI+SI+PN	63.78	2.63	4.1	73.78	3.13	4.2
ND280 const. flux & xsec	63.74	9.67	15.2	72.63	2.34	3.2
$\sigma(\nu_e)/\sigma(\nu_\mu)$, $\sigma(\overline{\nu}_e)/\sigma(\overline{\nu}_\mu)$	63.45	1.63	2.6	73.54	1.95	2.7
NC1γ	63.73	0.82	1.3	73.81	0.80	1.1
NC Other	64.43	0.11	0.2	73.52	0.11	0.1
Syst. Total	64.33	10.11	15.7	73.23	4.39	6.0

Table A.7: ν_μ 1R

	Pre-BANFF			Post-BANFF		
Sample	mean	1σ	%	mean	1σ	%
SK detector	241.95	5.63	2.3	268.57	5.10	1.9
SK FSI+SI+PN	241.05	6.82	2.8	267.69	5.90	2.2
SK Detector+FSI+SI+PN	242.89	8.84	3.6	268.93	7.75	2.9
ND280 const. flux & xsec	243.56	35.22	14.5	266.72	8.69	3.3
$\sigma(\nu_e)/\sigma(\nu_\mu)$, $\sigma(\overline{\nu}_e)/\sigma(\overline{\nu}_\mu)$	241.92	0.00	0.0	268.36	0.00	0.0
NC1γ	241.92	0.00	0.0	268.36	0.00	0.0
NC Other	241.92	0.68	0.3	268.37	0.68	0.3
Syst. Total	244.47	36.08	14.8	267.48	11.79	4.4

Table A.8: $\overline{\nu}_e$ 1R

	Pre-BANFF			Post-BANFF		
Sample	mean	1σ	%	mean	1σ	%
SK detector	7.48	0.33	4.4	8.07	0.34	4.2
SK FSI+SI+PN	7.39	0.20	2.8	7.99	0.20	2.5
SK Detector+FSI+SI+PN	7.44	0.36	4.8	7.99	0.38	4.8
ND280 const. flux & xsec	7.45	0.91	12.3	7.85	0.23	2.9
$\sigma(\nu_e)/\sigma(\nu_\mu)$, $\sigma(\overline{\nu}_e)/\sigma(\overline{\nu}_\mu)$	7.36	0.11	1.5	7.92	0.12	1.5
NC1γ	7.43	0.21	2.8	8.00	0.21	2.6
NC Other	7.36	0.03	0.3	7.92	0.03	0.3
Syst. Total	7.61	1.01	13.3	8.00	0.51	6.4

Table A.9: $\overline{\nu}_\mu$ 1R

	Pre-BANFF			Post-BANFF		
Sample	mean	1σ	%	mean	1σ	%
SK detector	58.19	1.07	1.8	63.21	0.99	1.6
SK FSI+SI+PN	58.03	1.38	2.4	63.04	1.27	2.0
SK Detector+FSI+SI+PN	60.02	1.75	2.9	64.36	1.60	2.5
ND280 const. flux & xsec	60.44	7.24	12.0	63.98	1.75	2.7
$\sigma(\nu_e)/\sigma(\nu_\mu)$, $\sigma(\overline{\nu}_e)/\sigma(\overline{\nu}_\mu)$	59.84	0.00	0.0	64.26	0.00	0.0
NC1γ	59.84	0.00	0.0	64.26	0.00	0.0
NC Other	59.84	0.16	0.3	64.26	0.16	0.3
Syst. Total	60.66	7.39	12.2	64.11	2.43	3.8

Table A.10: 1R ν_e CC1π^+

	Pre-BANFF			Post-BANFF		
Sample	mean	1σ	%	mean	1σ	%
SK detector	8.669	0.152	1.8	7.04	1.16	16.5
SK FSI+SI+PN	7.73	0.88	11.4	6.95	0.79	11.3
SK Detector+FSI+SI+PN	7.79	1.49	19.1	7.03	1.35	19.2
ND280 const. flux & xsec	7.68	0.90	11.7	6.90	0.28	4.0
$\sigma(\nu_e)/\sigma(\nu_\mu)$, $\sigma(\overline{\nu}_e)/\sigma(\overline{\nu}_\mu)$	7.70	0.20	2.6	6.92	0.18	2.6
NC1γ	7.71	0.02	0.3	6.93	0.02	0.3
NC Other	7.70	0.07	0.9	6.92	0.07	1.0
Syst. Total	7.68	1.64	21.3	6.99	1.37	19.6

Appendix B

One-dimensional Marginalised Likelihood

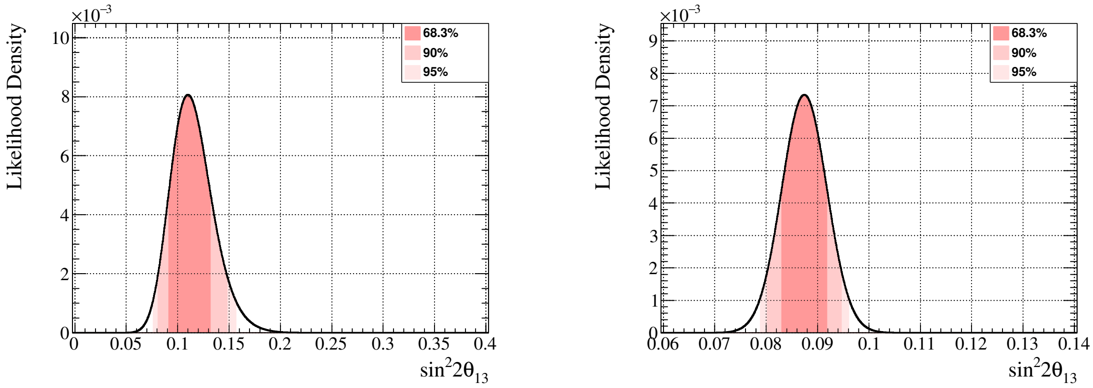

(a) T2K only

(b) T2K + reactor

Figure B.1: 1D Credible intervals in $\sin^2\theta_{13}$ for the normal hierarchy fit

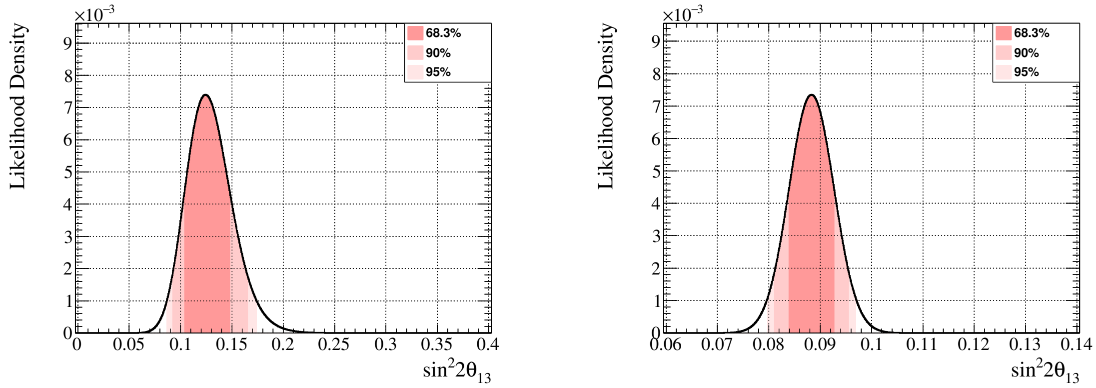

(a) T2K only

(b) T2K + reactor

Figure B.2: 1D Credible intervals in $\sin^2\theta_{13}$ for the inverted hierarchy fit

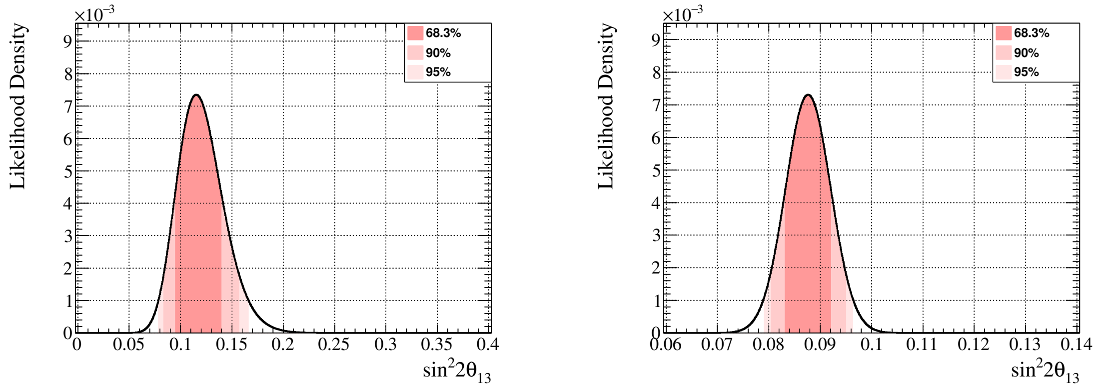

(a) T2K only

(b) T2K + reactor

Figure B.3: 1D Credible intervals in $\sin^2\theta_{13}$ for both hierarchies

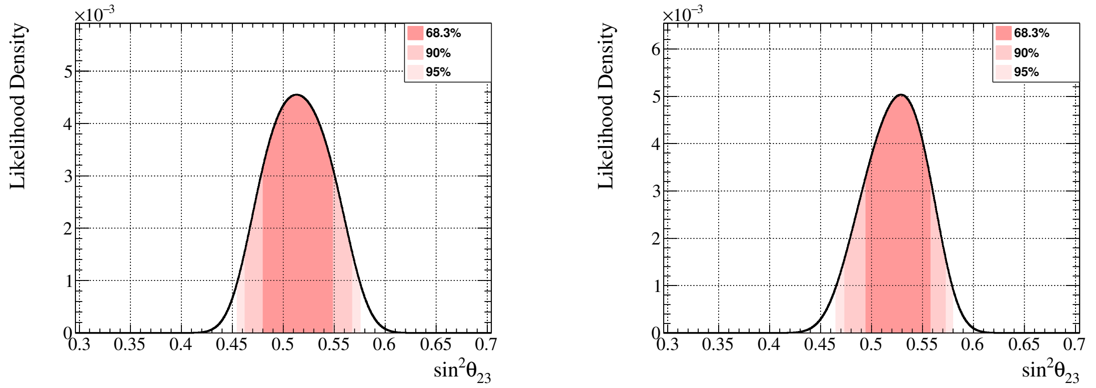

(a) T2K only

(b) T2K + reactor

Figure B.4: 1D Credible intervals in $\sin^2\theta_{23}$ for the normal hierarchy fit

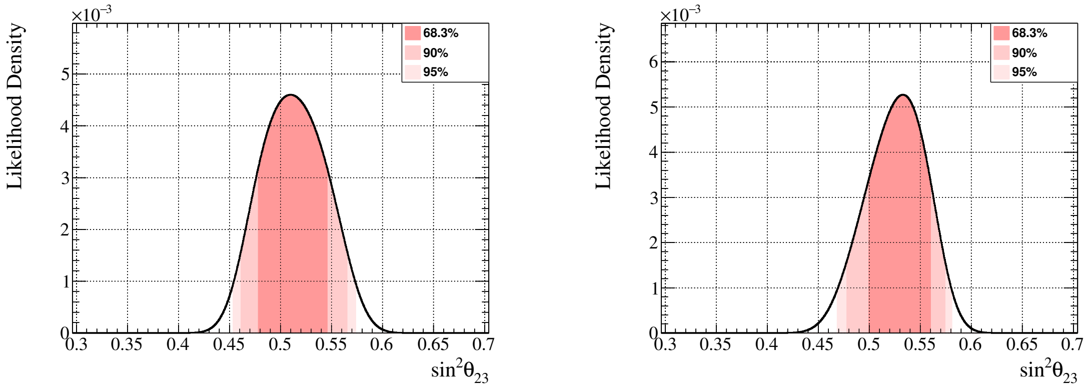

(a) T2K only (b) T2K + reactor

Figure B.5: 1D Credible intervals in $\sin^2\theta_{23}$ for the inverted hierarchy fit

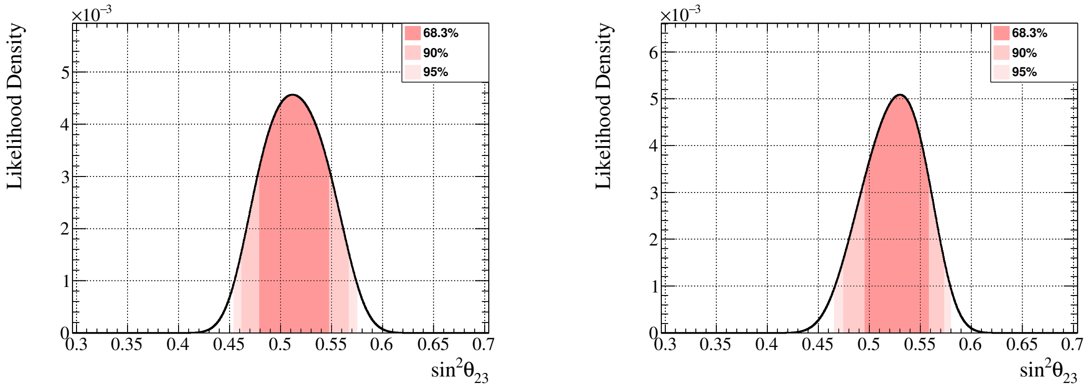

(a) T2K only (b) T2K + reactor

Figure B.6: 1D Credible intervals in $\sin^2\theta_{23}$ for both hierarchies

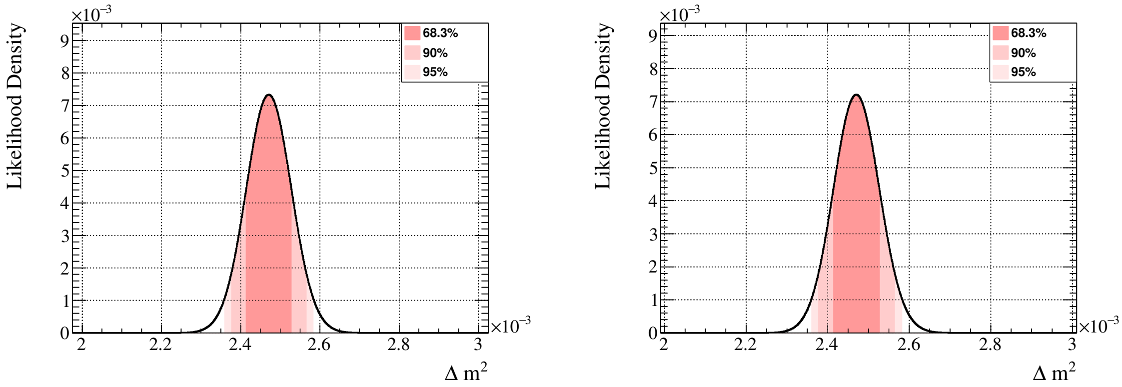

(a) T2K only (b) T2K + reactor

Figure B.7: 1D Credible intervals in Δm^2_{32} for the normal hierarchy fit

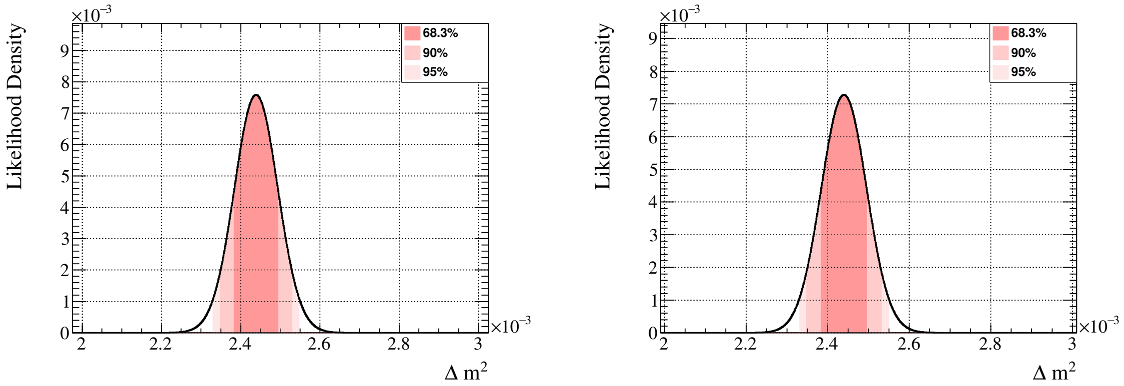

(a) T2K only

(b) T2K + reactor

Figure B.8: 1D Credible intervals in Δm^2_{31} for the inverted hierarchy fit

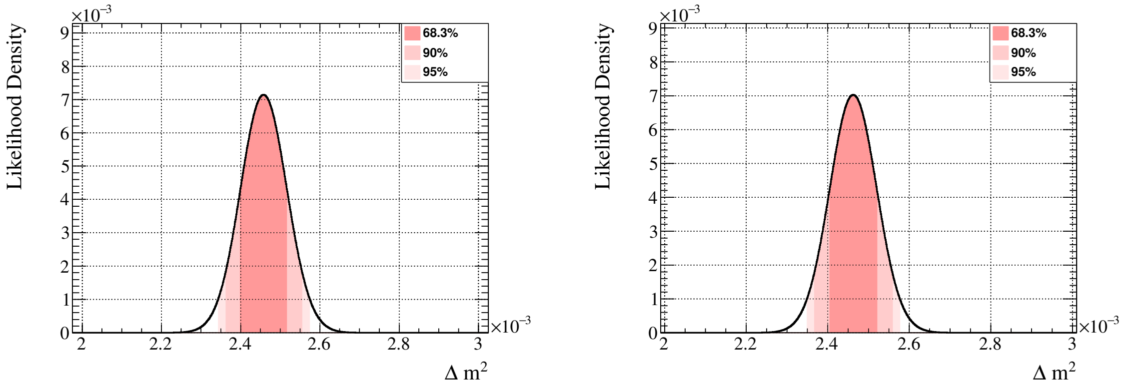

(a) T2K only

(b) T2K + reactor

Figure B.9: 1D Credible intervals in $|\Delta m^2|$ for both hierarchies

Appendix C

List of Acronyms

MC Monte Carlo Simulation 39

A method of generating simulated data by throwing random variables.

J-PARC Japan Proton Accelerator Research Complex 26

T2K the Tokai-to-Kamioka Experiment 2

FV fiducial volume 37

This has been re-defined since this analysis and is different for different SK samples considered.

POT protons on target 2

FHC Forward Horn Current 28

Equivalent to neutrino beam mode.

RHC Reverse Horn Current 28

Equivalent to antineutrino beam mode.

PID particle identification 35

NC Neutral-current 6

CC Charged-current 6

SF spectral function 43

PDD Pionless Delta decay 44

Process which consider absorption of baryon resonance.

FSI Final-state interactions 45

SI Secondary interactions 45

FS final state 48

RPA Random Phase Approximation 43

Takes into account the long range nucleon-nucleon correlation in a nucleus.

SPD Single π production 48

DPD Double π production 48

PMTs photomultiplier tubes 36

ID inner detector 36

OD outer detector 36

BANFF Beam And Nd280 Flux Fit 56

BeRPA Bernstein Random Phase Approximation 84

A parameterisation to the RPA function.

fiTQun Reconstruction algorithm.

NEUT A neutrino event generator which is primarily used in T2K.